

NASA Contractor Report 178353

COMBINED OPTIMIZATION OF IMAGE-GATHERING AND IMAGE-PROCESSING SYSTEMS FOR SCENE FEATURE DETECTION

**Nesim Halyo
Robert F. Arduini
Richard W. Samms**

**INFORMATION & CONTROL SYSTEMS, INCORPORATED
28 RESEARCH DRIVE
HAMPTON, VIRGINIA**

**CONTRACT NAS1-17133
AUGUST 1987**

**(NASA-CR-178353) COMBINED OPTIMIZATION OF
IMAGE-GATHERING AND IMAGE-PROCESSING SYSTEMS
FOR SCENE FEATURE DETECTION Final Report
(Information and Control Systems) 89 p
Avail: NTIS EC AC5/MF A01**

N87-27991

**Unclas
0097592**



**National Aeronautics and
Space Administration**

**Langley Research Center
Hampton, Virginia 23665**

FOREWORD

The work described in this report was performed by Information & Control Systems, Incorporated (ICS) under Contract Number NAS1-17133 for the National Aeronautics and Space Administration, Langley Research Center, Hampton, Virginia. Mr. Friedrich O. Huck was the NASA Technical Representative for this contract. Dr. Nesim Halyo directed the technical effort at ICS.

TABLE OF CONTENTS

FOREWORD.	1
LIST OF FIGURES	1v
CHAPTER I. COMBINED OPTIMIZATION OF IMAGE-GATHERING	
OPTICS AND IMAGE-PROCESSING ALGORITHM FOR	
EDGE DETECTION	1
1. INTRODUCTION	2
2. FORMULATION OF THE COMBINED OPTIMIZATION PROBLEM .	5
3. OPTIMIZATION OF CHARACTERISTIC IMAGE PROCESSORS. .	9
4. OPTIMAL IMAGE PROCESSOR FOR EDGE DETECTION	15
5. OPTIMIZATION OF THE IMAGE GATHERING OPTICS AND	
SENSITIVITY CONSIDERATIONS	20
6. CONCLUSIONS.	24
REFERENCES	26
CHAPTER II. EFFECTS OF ELECTRICAL FILTERING ON IMAGE-	
GATHERING AND IMAGE-PROCESSING SYSTEM	
OPTIMIZATION FOR EDGE DETECTION	45
1. INTRODUCTION	46
2. EFFECTIVE IMAGE-GATHERING SPATIAL RESPONSE	49
3. OPTIMAL IMAGE PROCESSOR.	56
4. OPTIMIZATION OF THE IMAGE GATHERING SYSTEM	61
5. CONCLUSIONS.	64
REFERENCES	66

PRECEDING PAGE BLANK NOT FILMED

PAGE 11 INTENTIONALLY BLANK

LIST OF FIGURES

CHAPTER I:

FIGURE 1.	BASIC BLOCK DIAGRAM FOR PROBLEM FORMULATION	28
FIGURE 2.	SMOOTHING OF SMALL DETAIL BY CONVOLVING SCENE RADIANCE $L(x)$ WITH A GAUSSIAN KERNEL, G_β , OF STANDARD DEVIATION β	29
FIGURE 3.	SENSOR (OTF) RESPONSES	30
FIGURE 4.	SCENE POWER SPECTRA FOR VARIOUS LEVELS OF DETAIL, μ_r	30
FIGURE 5.	EXAMPLE OF UNDERSAMPLING.	31
FIGURE 6.	OPTIMAL EDGE DETECTOR USING ∇^2	32
FIGURE 7.	OPTIMAL EDGE DETECTOR USING $\nabla^2 G_\beta, \beta = .2$	33
FIGURE 8.	OPTIMAL EDGE DETECTOR USING $\nabla^2 G_\beta, \beta = .4$	34
FIGURE 9.	OPTIMAL EDGE DETECTOR USING ∇^2 AND SQUARE APERTURE.	35
FIGURE 10.	OPTIMAL EDGE DETECTOR TRANSFER FUNCTION PERSPECTIVE PLOT FOR $\nabla^2 S/N = 32, \mu_r = 1, \rho_c = .38$. . .	36
FIGURE 11.	OPTIMAL EDGE DETECTOR TRANSFER FUNCTION PERSPECTIVE PLOT FOR $\nabla^2 S/N = 32, \mu_r = 1, \rho_c = .38$. . .	36
FIGURE 12.	OPTIMAL EDGE DETECTOR TRANSFER FUNCTION PERSPECTIVE PLOT FOR $\nabla^2 S/N = 32, \mu_r = 1$	37
FIGURE 13.	OPTIMAL EDGE DETECTOR POINT SPREAD FUNCTION. . . .	38
FIGURE 14.	1-D SIMULATIONS OF OPTIMAL EDGE DETECTORS FOR $\frac{d^2}{dx^2} G_\beta, \beta = .2$	39

LIST OF FIGURES (CONCLUDED)

FIGURE 15.	MEAN-SQUARED ERROR VERSUS OTF CUT-OFF FREQUENCY FOR $\nabla^2 G_\beta$ AND $\mu_r = 3$	40
FIGURE 16.	MEAN-SQUARED ERROR VERSUS OTF CUT-OFF FREQUENCY FOR $\nabla^2 G_\beta$ AND $\mu_r = 1$	41
FIGURE 17.	MEAN-SQUARED ERROR VERSUS OTF CUT-OFF FREQUENCY FOR SCENE RECONSTRUCTION $G_\beta * L$ AND $\mu_r = 3$	42
FIGURE 18.	SENSITIVITY TO UNCERTAINTIES IN ACTUAL SCENE DETAIL, μ_r . DESIGN BASED ON $\mu_r = 3$	43
FIGURE 19.	SENSITIVITY TO UNCERTAINTIES IN THE ACTUAL SIGNAL- TO-NOISE RATIO S/N; DESIGN BASED ON S/N OF 16.	44

CHAPTER II:

FIGURE 1.	BASIC SCANNER BLOCK DIAGRAM	68
FIGURE 2.	EFFECTIVE IMAGE-GATHERING PSF, $\tau(x,y)$	69
FIGURE 3.	EFFECTIVE IMAGE-GATHERING OTF, $\hat{\tau}(\nu,\omega)$	72
FIGURE 4.	IMAGE-GATHERING OPTICS.	75
FIGURE 5.	LOW-PASS ELECTRICAL FILTER.	77
FIGURE 6.	OPTIMAL EDGE DETECTOR OTF ($c,(x,y) = -\nabla^2 L(x,y), \mu_r = 3$)	78
FIGURE 7.	OPTIMAL EDGE DETECTOR PSF ($c,(x,y) = -\nabla^2 L(x,y), \mu_r = 3$)	81

CHAPTER I.

COMBINED OPTIMIZATION OF IMAGE-GATHERING OPTICS AND IMAGE-PROCESSING ALGORITHM FOR EDGE DETECTION

ABSTRACT

This paper investigates the relationships between the image-gathering and image-processing systems for minimum mean-squared error estimation of scene characteristics. A stochastic optimization problem is formulated where the objective is to determine a spatial characteristic of the scene rather than a feature of the already blurred, sampled and noisy image data. An analytical solution for the optimal characteristic image processor is developed. The Wiener filter for the sampled image case is obtained as a special case, where the desired characteristic is scene restoration. Optimal edge detection is investigated using $\nabla^2 G$ as the desired characteristic, where G is a two-dimensional Gaussian distribution function. It is shown that the optimal edge detector compensates for the blurring introduced by the image gathering optics, and notably, that it is not circularly symmetric. The lack of circular symmetry is largely due to the geometric effects of the sampling lattice used in image acquisition. The optimal image gathering OTF is also investigated and the results of a sensitivity analysis are shown.

1. INTRODUCTION

Much attention on edge detection has centered around the development of algorithms which process the sampled image data obtained by an image acquisition system [1] - [5]. Often these algorithms are finite difference approximations to linear isotropic differential operators, and are generally based on highly intuitive and heuristic arguments.

On the other hand, a frequency domain filter which maximizes the energy within a specified interval about an edge (modeled as a step function) given the constraints that the filter response vanish at zero frequency and outside a specified frequency band and be symmetric is developed in [6], [7]. The result of this approach, namely the $\nabla^2 G$ operator, where G represents a two-dimensional Gaussian distribution function, is also obtained in [2] which uses a heuristic argument to minimize a different objective function.

A statistical approach to image reconstruction and edge detection using Wiener filter concepts is found in [8] - [13]. In general, the underlying approach in these studies is to develop image processing algorithms in order to determine a spatial characteristic of the image, such as its edges. In [12] and [13], the effects of the image gathering point spread function (PSF) are included for the Wiener filter case ([9], [10]) where the desired spatial characteristic is scene restoration. The relationship between the mean-squared error and the pupil function of the aperture at various signal-to-noise ratios is investigated for a class of one-dimensional pupil functions in [13]. In all cases, the effects of the image gathering sampling lattice on the optimal processor and the relationships between the image gathering and processing systems has not received much attention. In most studies, the effects of the image gathering PSF used in acquiring the image are not explicitly modeled and included in the development of the processing algorithms.

In this paper, the objective is to determine a spatial characteristic or feature of the scene under observation, rather than a characteristic of the already blurred, sampled and

noisy image data. The image processing algorithm is designed to produce a spatial characteristic of the scene radiance observed from the samples of the image obtained by the acquisition system. In order to obtain the desired feature of the scene, the optimal image processor must compensate for the major effects of the image gathering system; namely, the blurring introduced by the image gathering optics, the aliasing effects due to the sampling lattice used, and the sensor noise effects, or more generally, image acquisition errors.

When the objective is formulated as a characteristic of the scene, rather than the image, both the image gathering system and the image processing algorithm have significant effects on the error in estimating the scene characteristic, as shown in Figure 1. Thus, both the image gathering and image processing systems must be optimized to obtain the total imaging system; i.e., the optimal image gathering and processing systems must be compatible with each other.

In Section 2, a combined stochastic optimization problem is formulated where the objective is to estimate a spatial characteristic of the scene. The optimization criterion considered is the spatially-averaged mean-squared error between the desired scene characteristic and the output of the image processing system. Characteristics which can be obtained from the scene using a linear operator are considered. This class of characteristics includes scene reconstruction, low-pass, band-pass or other filtering tasks, estimation of the gradient, $\nabla^2 G$, etc.

An analytical expression for the optimal characteristic image processor in terms of the image gathering system parameters is obtained in Section 3. This general expression explicitly shows the relationships between the optimal image gathering and processing systems for an arbitrary desired characteristic. The Wiener filter for the sampled image case is obtained as a special case of the optimal characteristic image processor, where the desired characteristic is selected to be least-mean-square scene reconstruction. The optimal characteristic image processor for the special case of a scene characteristic corresponding to the DOG (Difference-Of-Gaussian) operator is also used in [17] to investigate the rela-

tionships between the criteria of fidelity and information density. Some general properties of the optimal characteristic image processor are mentioned.

Section 4 investigates the optimal image processor for edge detection using scene characteristics corresponding to $\nabla^2 G$ operators. It is shown that the optimal edge processor tries to compensate for the blurring introduced by the image gathering optics by appropriately amplifying the spatial frequencies which have been attenuated in image acquisition. In particular, it is shown that the optimal edge detector is not circularly symmetric even when the desired characteristic has a circularly symmetric spectrum. This is shown to be due to the non-symmetric effects of the sampling lattice used in image acquisition.

The combined optimization of the image gathering optics and characteristic image processor, as well as the sensitivity of the processor is investigated in Section 5. General expressions for the spatially-averaged mean-squared error in estimating an arbitrary scene characteristic are presented. The optimization of the image gathering optics for edge detection is investigated both according to the mean-squared error criterion and according to the robustness or insensitivity of the image processor.

In this paper, the specific results have largely centered around edge detection and the $\nabla^2 G$ characteristics, as the edges of a scene are generally accepted to contain much of the important information in an image. However, the results of Sections 3 and 4 are general and applicable to the estimation of a large class of characteristics; so that the methodology of combined optimization of the image gathering and processing systems can be applied to the analysis and synthesis of a variety of imaging problems.

2. FORMULATION OF THE COMBINED OPTIMIZATION PROBLEM

Consider an image gathering system whose output is fed to an image processor to obtain the total imaging system output, as shown in Figure 1. The image gathering system is described by the Optical Transfer Function (OTF) of the optics, the sampling lattice and an additive noise process. Thus, the image gathering system transforms the scene into a sampled image which is blurred and corrupted by noise.

The sampled image data is then processed by an algorithm with the objective of obtaining some spatial characteristic or feature of the scene under observation. As the objective is to determine a feature of the object scene under observation, rather than a feature of the already blurred, sampled and noisy image, the image processor must appropriately compensate for the blurring introduced by the OTF and for the particular sampling lattice, while accounting for system noise. In this formulation, it is clear that both the parameters of the image gathering system and the image processing algorithm must be optimized in order to best achieve the objective of obtaining the desired scene characteristic.

For notational simplicity, x, ω and k will be used to represent column vectors with two components $(x_1, x_2)^T, (\omega_1, \omega_2)^T$, and $(k_1, k_2)^T$, respectively.¹ The product $k\omega$ of two column vectors will represent the vector $(k_1\omega_1, k_2\omega_2)^T$. The product of a row vector by a column vector (e.g., $\omega^T x = \omega_1 x_1 + \omega_2 x_2$) will represent the usual inner (or dot) product. In general, we will use x as the spatial location variable and ω as the spatial frequency variable.

As shown in Figure 1, let $L(x)$ represent the scene radiance, $\hat{\tau}(\omega)$ ² the OTF of the image gathering optics, corresponding to the Point Spread Function (PSF) $\tau(x)$. Let

¹The superscript "T" denotes the transpose of a vector or matrix.

²The superscript "^" denotes the two-dimensional Fourier Transform.

$x(k)$ be the sampling points $(x_1(k_1), x_2(k_2))$ defining the sampling lattice used, $m(k)$ the noisy and blurred image at the sampling points $x(k)$, and $n(k)$ the equivalent noise after sampling. We consider the particular scene radiance $L(x)$ viewed, and the particular noise sequence $n(k)$ encountered to be realizations of second order stationary random processes. In this way, the imaging system is designed for a class of scenes and noise patterns having the same Power Spectral Density (PSD or Wiener spectrum). The scene $L(x)$ and the noise $n(k)$ are assumed to be statistically independent processes. We will denote the power spectral densities of the scene radiance, $L(x)$, by $\hat{\phi}_L(\omega)$, while the PSD's of other random processes will have appropriate subscripts.

With the notation described, the basic equations defining the image gathering system can be formally expressed as

$$L(x) = \int_{R^2} e^{i2\pi\omega^T x} \hat{L}(\omega) d\omega, \quad x \in R^2 \quad (1)$$

$$s(x) = \int_{R^2} \tau(x - x') L(x') dx', \quad (2)$$

$$s(x) = \int_{R^2} e^{i2\pi\omega^T x} \hat{\tau}(\omega) \hat{L}(\omega) d\omega, \quad (3)$$

$$M(x) = s(x) + n(x), \quad (4a)$$

$$m(k) = M(x_k) = s(x(k)) + n(k), \quad -\infty < k_1, k_2 < \infty. \quad (4b)$$

For ease of notation, a single integral sign over R^2 (Euclidian 2-space) is used to denote a double integral. It should be noted that Fourier theory for second-order random processes requires the use of stochastic Riemann-Stieltjes integrals [18], [14]. However, to maintain the familiarity of deterministic Fourier transform relationships, (1), (2) and

(3) are formally expressed in the same manner as deterministic functions, but should be interpreted as stochastic integrals described in the Appendix of [14] for mathematical rigor.

As shown in (4b), the image $m(k)$ is a sequence of points obtained from sampling the continuous image $M(x)$ according to the selected sampling strategy. Thus, the image processor must operate on this image sequence in order to best estimate the desired scene characteristic, $c(x)$. In this paper, the sampling intervals are normalized to unity, unless stated otherwise. We will consider the class of image processors shown below.

$$r(x) = \sum_{k=-\infty}^{\infty} \tau_p(x - x(k)) m(k) , \quad x \in R^2 \quad (5)$$

Thus, the processed output is (in general) an infinite sum of the samples of the image weighted according to the image processor PSF, $\tau_p(x)$. The processing algorithm produces an output at any point x , not just at the sampling points $x(k)$. Note that when the output is restricted to the sampling points,¹ (5) becomes a discrete convolution corresponding to a spatially-invariant linear system. However, in the general case, this processor does not satisfy all the requirements for a spatially-invariant system. For the class of image processors selected, the processing algorithm is completely determined by the PSF $\tau_p(x)$ or equivalently by its Fourier transform, $\hat{\tau}_p(\omega)$.

The class of scene characteristics considered in this paper is the class that can be obtained from scene, $L(x)$, using a linear, spatially-invariant operator. Thus, if the desired scene characteristic is $c(x)$, then

$$c(x) = \int_{R^2} \tau_c(x - x') L(x') dx' \quad (6)$$

$$= \int_{R^2} e^{i2\pi\omega^T x} \hat{\tau}_c(\omega) \hat{L}(\omega) d\omega . \quad (7)$$

The Wiener spectrum of the desired characteristic can be found to be

³Other selections are also possible.

$$\hat{\phi}_c(\omega) = |\hat{\tau}_c(\omega)|^2 \hat{\phi}_L(\omega) , \quad \omega \in R^2 . \quad (8)$$

The class of scene characteristics considered is quite large, as any linear and spatially-invariant operator where the characteristic, $c(x)$, has a finite variance, can be optimized. The class includes operators such as the Gaussian class, the Difference of Gaussian (DOG) class, $\nabla^2 G$, ∇ , high-pass, low-pass and band-pass filters, etc.

The criterion of optimization used in this paper is the spatially-averaged mean-squared error. While other criteria often produce useful results [14], [15], the mean-squared error (or derivatives such as fidelity) provides a simple, easy to understand criterion which produces analytical and insightful solutions. The criterion of optimization can be expressed as

$$J = \lim_{|A| \rightarrow \infty} \frac{1}{|A|} \int_A E |c(x) - r(x)|^2 dx , \quad (9)$$

where E denotes the statistical expectation operator and $|A|$ the area of the surface A .

The combined optimization problem can now be posed as the problem of determining the image gathering system OTF, $\hat{\tau}(\omega)$, and the characteristic image processing algorithm determined by $\tau_p(x)$ or $\hat{\tau}_p(\omega)$ which minimize the spatially-averaged mean-squared error, J , between the desired scene characteristic, $c(x)$, and the imaging system output, $r(x)$, subject to constraints on $\hat{\tau}(\omega)$ and $\hat{\tau}_p(\omega)$.

3. OPTIMIZATION OF CHARACTERISTIC IMAGE PROCESSORS

We will approach the combined optimization problem in two steps. The first step is to optimize the characteristic image processor, $\hat{r}_p(\omega)$, as if the OTF $\hat{r}(\omega)$ were a known, fixed function. This results in the optimal characteristic image processor as a function of the image gathering optical transfer function, $\hat{r}(\omega)$. Then, with this optimal characteristic image processor, the criterion J can be minimized to obtain the optimal OTF, $\hat{r}(\omega)$, within a class or realizable optics, which constitutes the second step.

In this section, the first step will be solved analytically. This important result provides the relationships between the optimal characteristic image processor and the image gathering system. The results provide insight by pointing out the parameters which are more important than others.

When the parameters of the image gathering system are fixed, the optimal processor, $\hat{r}_p(\omega)$, operating on the image data is the processor whose output, $r(x)$, is the least mean-square estimate of the scene characteristic, $c(x)$. It is well-known that, for second-order random processes, the optimal output, $r(x)$, is the projection of the scene characteristic, $c(x)$, onto the Hilbert Space generated by the image data $\{m(k), -\infty < k < \infty\}$, (e.g., see [19]). Thus, applying the Projection Theorem to the first step of our optimization problem, it can be shown that a linear characteristic image processor minimizes the mean-squared error $E|c(x) - r(x)|^2$ if, and only if,

$$E(r(x) m(k)) = E(c(x) m(k)), \quad \forall k. \quad (10)$$

Furthermore, such $r(x)$ exists and is unique with probability 1.

Now to determine the characteristic image processor satisfying (10), first note that from (2) and (3),

$$m(k) = M(x(k)) = \int_{R^2} e^{i2\pi\omega^T x(k)} \hat{r}(\omega) \hat{L}(\omega) d\omega + n(k) . \quad (11)$$

Combining (11) and (7),

$$E(c(x) m(k)) = \int_{R^2} e^{i2\pi\omega^T (x-x(k))} \hat{r}_c(\omega) \hat{r}^*(\omega) \hat{\phi}_L(\omega) d\omega \quad (12)$$

where we have used the facts that $m(k)$ is real and that the scene radiance, $L(x)$, and the noise, $n(k)$, are uncorrelated.

To obtain the left hand side of (1), first note that

$$m(k) = M(x(k)) = \int_{R^2} e^{i2\pi\omega^T x(k)} \hat{M}(\omega) d\omega \quad (13)$$

$$\begin{aligned} &= \int_{R^2} e^{i2\pi(\omega^T + j\omega_o^T)x(k)} \hat{M}(\omega) d\omega \\ &= \int_{R^2} e^{i2\pi\omega^T x(k)} \hat{M}(\omega - j\omega_o) d\omega \end{aligned} \quad (14)$$

where ω_o is the Nyquist frequency vector and j is an arbitrary integer. Taking the Fourier transform of (5)

$$\hat{r}(\omega) = \hat{r}_p(\omega) \hat{m}(\omega) \quad , \quad \omega \in R^2 \quad (15)$$

where $\hat{m}(\omega)$ is the discrete Fourier transform of the sampled image data, i.e.,

$$\hat{m}(\omega) = \sum_{k=-\infty}^{\infty} m(k) e^{-i2\pi\omega^T x(k)} \quad , \quad x(k) = kX . \quad (16)$$

On the other hand, using Theorem 3, in the Appendix of [14],

$$r(x) = \int_{R^2} e^{i2\pi\omega^T x} \hat{r}_p(\omega) \hat{r}(\omega) d\omega \quad (17)$$

$$= \sum_{j=-\infty}^{\infty} \int_{R^2} e^{i2\pi\omega^T x} \hat{r}_p(\omega) \hat{M}(\omega - j\omega_o) d\omega . \quad (18)$$

Combining (14) and (18), we obtain the LHS of (10).

$$E(r(x) m(k)) = \sum_{j=-\infty}^{\infty} \int_{R^2} e^{i2\pi\omega^T(x-z(k))} \hat{\tau}_p(\omega) \hat{\phi}_M(\omega - j\omega_o) d\omega \quad (19)$$

$$= \int_{R^2} e^{i2\pi\omega^T(x-z(k))} \hat{\tau}_p(\omega) \hat{\phi}_m(\omega) d\omega \quad (20)$$

Substituting (20) and (12) into (10), we obtain the expression for the optimal characteristic image processor

$$\hat{\tau}_p(\omega) = \hat{\tau}_c(\omega) \frac{\hat{\tau}^*(\omega) \hat{\phi}_L(\omega)}{\hat{\phi}_m(\omega)}, \quad \omega \in R^2 \quad (21)$$

where $\hat{\phi}_m(\omega)$ is given by (e.g., [12], [13])

$$\begin{aligned} \hat{\phi}_m(\omega) &= \sum_{k=-\infty}^{\infty} |\hat{\tau}(\omega - k\omega_o)|^2 \hat{\phi}_L(\omega - k\omega_o) + \hat{\phi}_n(\omega) \\ &= \hat{\phi}_a(\omega) + \hat{\phi}_n(\omega). \end{aligned} \quad (22)$$

Thus, an analytic expression for the optimal characteristic image processor transfer function in terms of the parameters of the image gathering system has been obtained. The optimal characteristic image processor PSF, $\tau_p(x)$, used in (5) is obtained simply as the inverse Fourier transform of the optimal transfer function, $\hat{\tau}_p(\omega)$, given in (21).

The expression obtained, (21), can be viewed as a compatibility measure between the characteristic image processor and the image gathering system, as this expression explicitly points out the relationships between the two system parameters which produce the smallest mean-squared error in the estimation of a scene characteristic. Whether or not the image gathering system is the "best" system to determine a particular scene characteristic, the relationship shown in (21) holds as the least-mean-squared error characteristic image processor for that case. While this relationship will be investigated for particular

classes of scenes, optical transfer functions, etc., some important general properties of the optimal characteristic image processor are worthy of note.

The optimal characteristic image processor is a linear function of the desired scene characteristic. As an example of the additive property, note that the optimal image processor for the characteristic $\nabla^2(\cdot) = \frac{\partial^2}{\partial x_1^2}(\cdot) + \frac{\partial^2}{\partial x_2^2}(\cdot)$ ($\hat{r}_c(\omega) = -(\omega_1^2 + \omega_2^2) = -\rho^2$), is the sum of the optimal image processors for the characteristics $\frac{\partial^2}{\partial x_1^2}(\cdot)$ ($\hat{r}_{c1}(\omega) = -\omega_1^2$) and $\frac{\partial^2}{\partial x_2^2}(\cdot)$ ($\hat{r}_{c2}(\omega) = -\omega_2^2$). This linearity property carries further into linear operators. Suppose that $c_o(x)$ is the scene characteristic corresponding to the characteristic transfer function $\hat{r}_{c_o}(\omega)$, and that we would like to estimate a new characteristic, $c(x)$, defined by the convolution

$$c(x) = a(x) * c_o(x) = [a(x) * \tau_{c_o}(x)] * L(x) \quad (23)$$

$$\hat{c}(\omega) = \hat{a}(\omega) \hat{c}_o(\omega) = [\hat{a}(\omega) \hat{r}_{c_o}(\omega)] \hat{L}(\omega) . \quad (24)$$

Then, the optimal characteristic image processor for $c(x)$ is given by

$$\hat{r}_p(\omega) = \hat{a}(\omega) \hat{r}_{p_o}(\omega) , \quad (24a)$$

$$\tau_p(x) = a(x) * \tau_{p_o}(x) , \quad (24b)$$

$$r(x) = a(x) * r_o(x) , \quad (24c)$$

where $\tau_{p_o}(x)$ and $r_o(x)$ are the optimal image processor and its output for the characteristic, $c_o(x)$.

⁴The symbol "*" denotes the two-dimensional convolution integral when applied as a binary operator.

An important special case of the optimal characteristic image processor is the Wiener filter [8], [9], [10], for sampled images. The Wiener filter corresponds to the case where the desired characteristic is simply the scene radiance; i.e.,

$$c(x) = L(x) \quad , \quad \hat{r}_c(\omega) = 1. \quad (25)$$

Substituting (25) into the general expression (21), results in the least-mean-squared error estimator of L , or the Wiener filter for sampled images.

$$\hat{r}_{pW}(\omega) = \frac{\tau^*(\omega) \hat{\phi}_L(\omega)}{\hat{\phi}_m(\omega)} \quad , \quad \omega \in R^2 \quad (26)$$

The Wiener and edge filters developed here were used in [17] to investigate the relationships between the criteria of information density and fidelity for scene reconstruction from sampled images.

It should also be noted that the optimal characteristic image processor given in (21) has a commutative property. In cases where it is desirable to perform some processing locally, this produces a flexibility in implementation and analysis. For this purpose, write $\hat{r}_p(\omega)$ in (21) as the product

$$\hat{r}_p(\omega) = \hat{a}(\omega) \hat{b}(\omega) = \hat{b}(\omega) \hat{a}(\omega) \quad , \quad (27a)$$

$$\tau_p(x) = a(x) * b(x) = b(x) * a(x) \quad . \quad (27b)$$

Then the optimal $r(x)$ can be implemented in either of the following ways, provided the terms in brackets are finite.⁵

⁵This commuting property cannot be extended past the sampling process which does not commute in the usual manner.

$$r(x) = a(x) * \left\{ \sum_{k=-\infty}^{\infty} b(x - x(k)) m(k) \right\} \quad (28a)$$

$$= b(x) * \left\{ \sum_{k=-\infty}^{\infty} a(x - x(k)) m(k) \right\} \quad (28b)$$

$$= \sum_{k=-\infty}^{\infty} \tau_p(x - x(k)) m(k) \quad (28c)$$

$$\hat{r}(\omega) = \hat{a}(\omega) \hat{b}(\omega) \hat{m}(\omega) = \hat{\tau}_p(\omega) \hat{m}(\omega) \quad (29)$$

Finally, it should be noted that the output $r(x)$ is the optimal estimate of the scene characteristic, $c(x)$, for every point x , i.e., $E|r(x) - c(x)|^2$ is minimized for every $x \in R^2$. Therefore, the optimal characteristic image processor, defined by (21) and (5), can be used to reconstruct $c(x)$ as a continuous function, or to optimally estimate $c(x)$ over a finer grid than the sampling lattice (or the same lattice) as the image data. Applications of the optimal image processor in this fashion include optimal interpolation between sampling points, or obtaining estimates over a finer grid which can be fed to a digital high-resolution display device for reconstruction. If the basis reconstruction function of the display device is known (e.g., Gaussian, cubic interpolation, etc.), a preprocessor may sometimes be desirable.

4. OPTIMAL IMAGE PROCESSOR FOR EDGE DETECTION

The optimal characteristic image processor given by (21) can be used to estimate any scene characteristic that can be expressed in the form of (6) or (7); i.e., any characteristic that can be obtained from the scene with a linear operator. An important characteristic of a scene is the location of its edges, or sudden, sharp changes of intensity in the scene radiance, $L(x)$. To investigate the implications of the optimal characteristic image processor to the task of edge detection, we will restrict attention to specific classes of scene and noise power spectral density image gathering system OTF's, and characteristics which contain edge information.

For this purpose, we will use the $\nabla^2 G_\beta$ operator, as the zero-crossings of this operator are known to contain information on edges [3], [7]; ∇^2 denotes the Laplacian operator and G_β denotes a Gaussian exponential with a standard deviation of β , viewed as a PSF. In this context, the standard deviation, β , of the Gaussian PSF determines the level of detail desired. Figure 2 shows a one-dimensional convolution of a scene containing a variety of edges with a Gaussian at various values of the standard deviation. As can be observed, the sharp edges are smoothed, and edges which occur close to each other (i.e., the high level of detail) are blurred increasingly, as β increases. Small detail smoothed in this manner becomes distinguishable from the image gathering system noise, and aliasing error. Variation of β allows us to specify the level of detail desired in estimating the location of edges. For example, if we want to accurately determine the finest detail, β can be set to a small value. On the other hand, if the smallest level detail is not necessary or desirable for a given application, β can be set to a higher value. Thus, the characteristic transfer function used is of the form⁶

⁶Note that the $\tau_c(\omega)$ expression used corresponds to $-\nabla^2 G_\beta$.

$$\hat{r}_c(\omega) = \rho^2 e^{-\beta^2 \rho^2/2} \quad , \quad \rho^2 = \omega_1^2 + \omega_2^2 \quad (30a)$$

$$c(x) = -\nabla^2 \{G_\beta(x) * L(x)\} . \quad (30b)$$

It should be noted that a subpixel accuracy is inherent in our formulation. Whether we are interested in small or large detail, the accuracy with which edges are located is an important property of an edge detector. As the system output shown in (5) can be computed for as fine a grid as desired, the zero-crossings of the optimal estimate of $\nabla^2 G_\beta$ can be determined to an arbitrary accuracy within the pixel in which they occur. Figure 14 shows one-dimensional simulations of the optimal edge detector estimating the characteristic $c(x) = -\nabla^2 G_\beta * L(x)$, for a Gaussian smoothing factor $\beta = .2$. As the zero-crossings of the output, $r(x)$, with appropriate thresholding provide estimates of the edge locations, it may be noted from Figure 14 that the error in locating the edges of $L(x)$ is significantly less than a pixel. Also note that due to the Gaussian smoothing, "small edges" are not detected, which is the intent in introducing the smoothing.

The class of image gathering system OTF's, $\hat{r}(\omega)$, which will be considered here have the form

$$\hat{r}(\omega) = e^{-\rho^2/\rho_0^2} \quad , \quad \rho^2 = \omega_1^2 + \omega_2^2 . \quad (31)$$

Figure 3 shows a cross-section of these circularly symmetric OTF's. This class of OTF's, while not exhaustive of all realizable transfer functions, is representative of the basic character of many apertures, and electro-optical device transfer functions. This form belongs to the more inclusive class of OTF's described in [20]. The case of a square aperture OTF is also considered for completeness.

It is important to note that for purposes of comparison and optimization, the OTF's are normalized so as to have equal "effective" aperture areas. Thus, for each OTF consid-

ered, the volume under the PSF of the image gathering system is kept constant.

The class of scene radiances considered here will be modeled as a homogeneous and isotropic random field; in particular, we use a wide-sense stationary second-order random process with power spectral density $\hat{\phi}_L(\omega)$ and covariance function $\phi_L(x)$ as shown below.

$$\hat{\phi}_L(\omega) = \frac{2\pi \mu_r^2 \sigma_L^2}{[1 + 4\pi^2 \mu_r^2 (\omega_1^2 + \omega_2^2)]^{3/2}} , \quad (32)$$

$$\phi_L(x) = E(L(x') L(x' + x)) = \sigma_L^2 e^{-r/\mu_r} , \quad r^2 = x_1^2 + x_2^2 . \quad (33)$$

Figure 4 shows cross-sections of the scene spectra $\hat{\phi}_L(\omega)$ in (32) for various values of μ_r .

The PSD in (32) corresponds to a random set of two-dimensional pulses whose width obeys an exponential probability law with average or mean width of μ_r , and whose magnitude obeys a Gaussian or Normal probability law with zero mean and variance σ_L^2 [21], [22]. This interpretation provides a physical significance to the scene statistics which is highly appropriate for edge detection investigations. Furthermore, the parameter μ_r attains a meaning directly applicable to the problem of optimal edge detection. Since μ_r is the average distance between two edges, it is a meaningful description of the amount of detail in the scene. For example, a μ_r value of 1 would imply that, on average, the scene contains an edge at every sampling interval (normalized to unity); so that the distance between some edges would be smaller and others larger than the sampling interval.

Suppose that, as shown in Figure 5, the scene contains four edges between two sampling points. From the samples of this scene shown in Figure 5, it is not possible to determine the location and magnitude of all four edges in the scene no matter what method of edge detection is used. This would be a situation occurring regularly throughout the scene for the case of $\mu_r = 1/4$. Thus, for edge detection purposes, the sampling interval selected would be very large, and must be reduced considerably if we are to reliably find the edges in the scene. Hence, we will consider optimal designs for the more realistic sampling rates according to the level of detail corresponding to μ_r values greater than 1.

Figures 6, 7, 8 and 9 show cross-sections of the optimal characteristic image processor (21) for edge detection using the characteristic $\nabla^2 G_\beta * L$ for various levels of desired detail, β , for various levels of detail present in the scene, μ_r , and for various image gathering OTF cut-off frequencies, ρ_c , as well as the case of a square aperture, all using a square sampling lattice. The optimal edge detector displays certain broad characteristics in all the cases shown despite the extent of variations in the parameters.

In all cases, the optimal edge detector vanishes at zero frequency, peaks near but before the Nyquist frequency (at .5), and attenuates at high frequencies. The optimal transfer functions tend to peak in the vicinity of .4 for a Nyquist frequency of .5 for almost all cases. However, the magnitude of the peaks varies considerably, largely according to the image gathering optics used in acquiring the image, but also with other variables. Thus, the optimal edge detector attempts to reduce the blurring introduced during image acquisition by amplifying the attenuated frequencies till close to the Nyquist frequency, where the aliasing and noise levels start to dominate.

Figures 10 and 11 show the two-dimensional perspectives of the optimal edge detector for the case of square and hexagonal sampling. Figure 12 shows the perspective plot for a square aperture with a square sampling lattice. It is clear that the optimal characteristic image processor for edge detection is not circularly symmetric even when the scene statistics, the image gathering optics and desired characteristic all have circular symmetry. The optimal edge detector is seen to be highly dependent on the sampling lattice used in the image gathering process. Thus, the optimal edge detector attempts to account for all three major effects introduced in an image acquisition: blurring, noise and sampling.

Figure 13 shows the PSF, $\tau_p(x)$, corresponding to the optimal edge detector using square sampling. This PSF is used as shown in (5) to implement the optimal characteristic image processor. The square shape of the optimal PSF is evident in the plots. This PSF can be used to estimate the desired characteristic as a continuous function, or at a much finer grid than the image to achieve subpixel accuracy as shown in the one-dimensional

simulations in Figure 14. It should be noted that the square shape of optimal edge detector, is a rather natural consequence of the sampling lattice effects in compensating for the cross-correlation of the signal at the sampling points. Also note from Figure 13c that the basic shape of the optimal PSF varies relatively little as the sensor cut-off frequency moves displaying some insensitivity to ρ_c .

5. OPTIMIZATION OF THE IMAGE GATHERING OPTICS AND SENSITIVITY CONSIDERATIONS

As discussed in Section 3, the combined optimization problem is divided into two steps: the optimization of the characteristic image processor and the optimization of the image gathering Optical Transfer Function (OTF). Having solved the former analytically as a function of the OTF, we use this expression (21) to evaluate the spatially-averaged mean-squared error, J , and minimize it over the class of OTF's selected.

We first obtain a general expression for the mean-squared error where the image processor $\hat{r}_p(\omega)$ is not necessarily the optimal processor. After some manipulation of (18), (3) and (4a), it can be shown that

$$r(x) = \int_{R^2} e^{i2\pi\omega^T x} \left[\sum_{j=-\infty}^{\infty} e^{i2\pi j\omega_o^T x} \hat{r}_p(\omega + j\omega_o) \right] [\hat{r}(\omega) \hat{L}(\omega) + \hat{N}(\omega)] d\omega \quad (34)$$

where $\hat{N}(\omega)$ is the continuous Fourier transform of the noise $n(x)$. From this expression, it becomes clear that the system output, $r(x)$, is not usually a wide-sense stationary process over R^2 . However, its statistics are periodic, so that when spatially averaged, the variations vanish. Also note that the sampled sequences $\{r(x(k) + \Delta)\}$ are stationary, due to the periodic nature of $r(x)$.

Substituting (34) and (7) into (9), and after considerable manipulation, the general expression for the spatially-averaged mean-squared error can be shown to be

$$J = \int_{R^2} \{ |\hat{r}_c(\omega)|^2 \hat{\phi}_L(\omega) - 2 \operatorname{Re} [\hat{r}_c^*(\omega) \hat{r}(\omega) \hat{r}_p(\omega)] \hat{\phi}_L(\omega) + |\hat{r}_p(\omega)|^2 \hat{\phi}_m(\omega) \} d\omega \quad (35)$$

where $\hat{r}_p(\omega)$ is an arbitrary image processor rather than the optimal one, and $\hat{\phi}_m(\omega)$ is the PSD of the sampled image which includes aliasing, as given in (22). Therefore, this

expression can be used to evaluate the mean-squared error in estimating a characteristic, $c(x)$, using an OTF, $\hat{\tau}(\omega)$, and an arbitrary image processor, $\hat{\tau}_p(\omega)$.

When the optimal characteristic image processor in (21) is used, the mean-squared error becomes

$$J = \int_{R^2} \frac{1}{1 + \frac{|\tau(\omega)|^2 \hat{\phi}_L(\omega)}{\hat{\phi}_a(\omega) + \hat{\phi}_n(\omega)}} |\hat{\tau}_c(\omega)|^2 \hat{\phi}_L(\omega) d\omega \quad (36a)$$

$$= \int_{R^2} \frac{1}{1 + \frac{S}{N}(\omega)} \hat{\phi}_c(\omega) d\omega = \int_{R^2} 2^{h(\omega)} \hat{\phi}_c(\omega) d\omega \quad (36b)$$

$$= \sigma_c^2 - \int_{R^2} |\hat{\tau}(\omega) \hat{\tau}_c(\omega)|^2 \frac{\hat{\phi}_L(\omega)}{\hat{\phi}_m(\omega)} d\omega, \quad (36c)$$

where $\hat{\phi}_a(\omega)$ is the PSD of the aliasing error and $\hat{\phi}_m(\omega)$ the PSD of the discrete noise, and σ_c^2 is the variance of the desired characteristic, $c(x)$; i.e.,

$$\sigma_c^2 = E |c(x)|^2 = \int_{R^2} |\hat{\tau}_c(\omega)|^2 \hat{\phi}_L(\omega) d\omega. \quad (37)$$

These expressions show the relationships between the mean-squared error and the signal-to-noise ratio, S/N , and the information density, $h(\omega)$.

It should be noted from both (36) and (35), that when the image gathering OTF, $\hat{\tau}(\omega)$, vanishes or is small over a frequency band, it is essentially not possible to recover the desired characteristic over that band. Thus, if the desired characteristic has high-frequency content, an image gathering OTF which acquires the high-frequency content even at the expense of some aliasing will result in a lower mean-squared error. Of course, to the extent possible, it is desirable to select a sampling interval so that most of the characteristic to be estimated is contained within the Nyquist band.

Figures 15, 16 and 17 show the spatially-averaged mean-squared error when using the optimal characteristic image processor for the characteristics $\nabla^2 G_\beta * L$ and simply L for various levels of noise; i.e., for optimal edge detection and for optimal restoration of the

image. As can be seen from the plots, the OTF shape which minimizes the mean-squared error depends on the frequency content of the desired scene characteristic. As the desired characteristic is smoothed by the Gaussian operator G_β , which shifts the frequency content lower, a shift to lower cut-off frequency can be noticed. However, the basic shape of the curves in most cases is such that a cut-off frequency in the interval from .5 to .7 produces little variation from the optimal. Further note that for low signal-to-noise ratios, the trend is to open the OTF band-width. In the case of edge detection, where the high-frequency or fine detail is to be estimated, the tendency is to prefer a higher cut-off frequency, ρ_c , for the image gathering OTF. While in the case of image restoration, where the desired characteristic has relatively low-frequency content, the mean-squared error is optimized at a lower cut-off frequency.

An important characteristic of any design is its robustness; i.e., its lack of sensitivity to variations in parameters about the scene. In particular, the optimal characteristic image processor depends on our expectation of the scene, namely, μ_r and $\hat{\phi}_n$. Now suppose that we design the image processor based on values $\mu_{rp}, \hat{\phi}_{np}$, but the actual scene corresponds to different values say μ_r and $\hat{\phi}_n$. It is important to know how much loss from the optimal design for the actual case ($\mu_r, \hat{\phi}_n$) we suffer by incorrectly designing for μ_{rp} and $\hat{\phi}_{np}$. Figures 18 and 19 show the loss from the optimal when the design is based on $\mu_{rp} = 3$, and a signal-to-noise ratio of 16. Figure 18 shows the change, or loss, of the mean-squared error for edge detectors for different values of mean spatial details in the actually observed scene, i.e., μ_r . It is seen that, when the actual scene detail is 3 times larger or smaller than expected, an OTF design with a cut-off frequency, ρ_c , higher than .6 produces minimal loss of performance. Note that, at these levels of mismatch, the sensitivity is low for all cut-off frequencies shown. Also note that, if the actual detail is larger than expected, the loss of accuracy is low. When the actual level of detail is much smaller than expected by the design (recall that the sampling interval is set to a value of 1), the edge detection sensitivity is accordingly higher, with some preference for ρ_c 's in the vicinity of .6.

Figure 19 shows the change, or loss, in mean-squared error when the signal-to-noise ratio is mismatched. When the actual signal-to-noise is lower than expected (i.e., higher than expected noise level), the curves are relatively flat over the range where the mean-squared error itself is small (see Figures 15 and 16). When the actual signal-to-noise ratio is larger than expected (i.e., lower than expected noise level), OTF cut-off frequencies higher than .6 appear to be preferable. Thus, designing for a noise level that is high and using OTF cut-off frequencies higher than .6 produce favorable noise robustness.

Interestingly, this sensitivity analysis tends to favor cut-off frequencies unless the expectations about the scene are grossly misjudged as represented by the curve for $\mu_r = 1/3$. The noise sensitivity curves indicate that, for higher ρ_c , designing for high noise can be advantageous.

Finally, the general expressions (35), (36) for the spatially-averaged mean-squared error in estimating a scene characteristic obtained in this section provide a general method of evaluating the combined image gathering and image processing systems, as well as providing insight into the basic tendencies and trade-offs involved in designing complex imaging systems.

6. CONCLUSIONS

This paper formulates a combined optimization problem where the optical transfer function (OTF) of the image gathering system, the noise level, the sampling lattice as well as the image processing algorithm are all design parameters to be selected according to the optimization criterion chosen to be the spatially-averaged mean-squared error. In this formulation, the objective is to determine a spatial characteristic of the scene radiance rather than a characteristic of the already blurred, noisy and sampled image.

With this formulation of the objective, the relationships between the image gathering system parameters and the image processing algorithm are clearly defined. To estimate a characteristic of the scene, the image processor must account for, or try to eliminate, any distortion that has been introduced in the image acquisition process.

The optimization of the image processor for a given image gathering system to estimate a scene characteristic is achieved analytically, which is the main result of the paper. An analytical expression for the optimal characteristic image processor in terms of the image gathering optical transfer function, the signal-to-noise ratio, and the sampling lattice effects is presented. This expression shows the relationships between the optimal characteristic image processor and the parameters of the image gathering system explicitly. The results are valid for characteristics which can be obtained from the scene by linear transformations. The Wiener filter for the case of sampled images is presented as a special case of the optimal characteristic image processor developed.

The optimal processor for edge detection is investigated by selecting scene characteristics from the form $\nabla^2 G$. The main results obtained show that the optimal edge detector 1) is not circularly symmetric but is highly dependent on the sampling lattice, as it attempts to account for its effects, 2) tends to peak near the Nyquist frequency, and vanish at zero and high frequencies, 3) attempts to reduce the blurring, aliasing and noise

effects introduced during image acquisition and 4) appears most insensitive to expected scene variations for ρ_c values between .7 and .9, corresponding to a 3 dB cut-off near the Nyquist frequency. One-dimensional simulations of the optimal edge detector demonstrate subpixel accuracy in determining the location of scene edges.

Expressions for the spatially-averaged mean-squared error between the desired scene characteristic and its estimate are obtained in terms of the scene power spectral density, the image gathering optical transfer function, the characteristic image processor and the desired scene characteristic. These expressions provide some insight into the behavior of the error for various designs. The results indicate that the optimal image gathering OTF depends on the frequency content of the scene characteristic desired. The basic tendency displayed is to increase the bandwidth of the image gathering system when the desired scene characteristic has high-frequency content.

Finally, the formulation presented provides an objective method of analyzing a complex imaging system where the objective is to determine a scene characteristic.

REFERENCES

1. Marr, D., *Vision*, W. H. Freeman and Company, San Francisco, 1982.
2. Marr, D. and E. C. Hildreth, "Theory of Edge Detection," *Proc. R. Soc. London Ser. B* 207, 187-217, 1980.
3. Hildreth, E. C., "The Detection of Intensity Changes by Computer and Biological Vision Systems," *Computer Vision, Graphics and Image Processing*, Vol. 22, pp. 1-27, 1983.
4. Rosenfeld, A. and A. C. Kak, *Digital Picture Processing*, Academic Press, New York, 1982.
5. Prewitt, M. S., "Object Enhancement and Extraction," in Lipkin, B. S. and Rosenfeld, A., *Picture Processing and Psychopictorics*, Academic Press, New York, 1970.
6. Shanmugam, K. S., Dickey, F. M. and J. A. Green, "An Optimal Frequency Domain Filter for Edge Detection in Digital Pictures," *IEEE Trans. on Pattern Analysis and Machine Intelligence*, Vol. PAMI-1, No. 1, pp. 37-49, 1979.
7. Lunscher, W. H. H. J., "Edge Detection," *IEEE Trans. on Pattern Analysis and Machine Intelligence*, Vol. PAMI-5, No. 6, pp. 678-680, 1983.
8. Horner, J. L., "Optical Spatial Filtering with the Least-Mean-Square Error Filter," *J. Opt. Soc. Am.*, Vol. 59, pp. 553-558, 1969.
9. Helmstrom, C. W., "Image Restoration by the Method of Least Squares," *J. Opt. Soc. Am.*, Vol. 57, pp. 297-303, 1967.
10. Slepian, D., "Linear Least-Squares Filtering of Distorted Images," *J. Opt. Soc. Am.*, Vol. 57, pp. 918-922, 1967.
11. Modestino, J. W. and R. W. Fries, "Edge Detection in Noisy Images Using Recursive Digital Filtering," *Computer Graphics and Image Processing*, Vol. 6, pp. 409-433, 1977.

12. Rushforth, C. K. and R. W. Harris, "Restoration, Resolution, and Noise," *J. Opt. Soc. Am.*, Vol. 58, No. 4, pp. 539-545, 1968.
13. Cathey, W. T., Frieden, B. R., Rhodes, W. T. and C. K. Rushforth, "Image Gathering and Processing for Enhanced Resolution," *J. Opt. Soc. Am. A*, Vol. 1, No. 3, pp. 241-250, 1984.
14. Halyo, N. and S. T. Stallman, "A Parametric Study of Aliasing Error for a Narrow Field of View Scanning Radiometer," NASA CR 3294, 1980.
15. Huck, F. O., Halyo, N. and S. K. Park, "Information Efficiency of Line-Scan Imaging Mechanisms," *Applied Optics*, Vol. 20, No. 11, pp. 1990-2007, 1981.
16. Huck, F. O., Park, S. K., Halyo, N. and S. T. Stallman, "Aliased Noise in Radiometric Measurements," NASA TP 1639, 1980.
17. Huck, F. O., Fales, C. L., Halyo, N., Samms, R. W. and K. Stacy, "Image Gathering and Processing: Information and Fidelity," *J. Opt. Soc. Am. A*, Vol. 2, No. 10, pp. 1644-1666, 1985.
18. Loève, M., *Probability Theory*, D. Van Nostrand Co., Inc., 1963.
19. Parzen, E., *Time Series Analysis Papers*, pp. 306-309, Holden-Day, San Francisco, 1967.
20. Johnson, C. B., "A Method for Characterizing Electro-Optical Device Modulation Transfer Functions," *Photographic Science and Engineering*, Vol. 14, No. 6, pp. 413-415, 1970.
21. Itakura, Y., et al., "Statistical Properties of the Background Noise for the Atmospheric Windows in the Intermediate Infrared Region," *Infrared Physics*, 14, Pergamon Press, 1974.
22. Takagi, T. and S. Tutumi, "Statistical Properties of Radiance Spatial Distribution of Sky and Forrest Backgrounds," *J. Elec. and Com. in Japan*, 51-C, 1968.

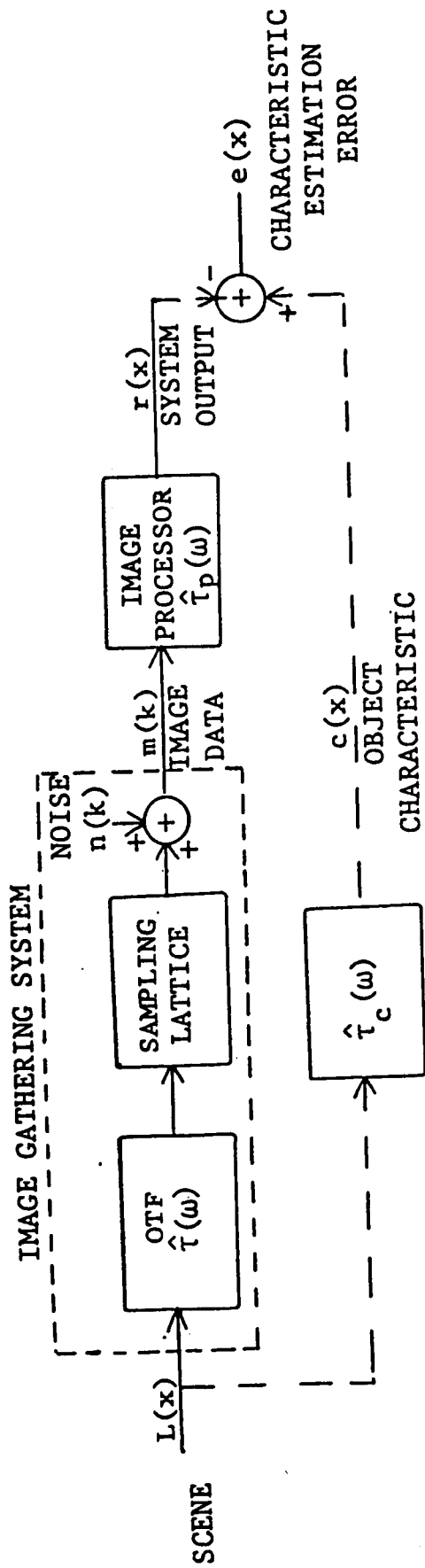
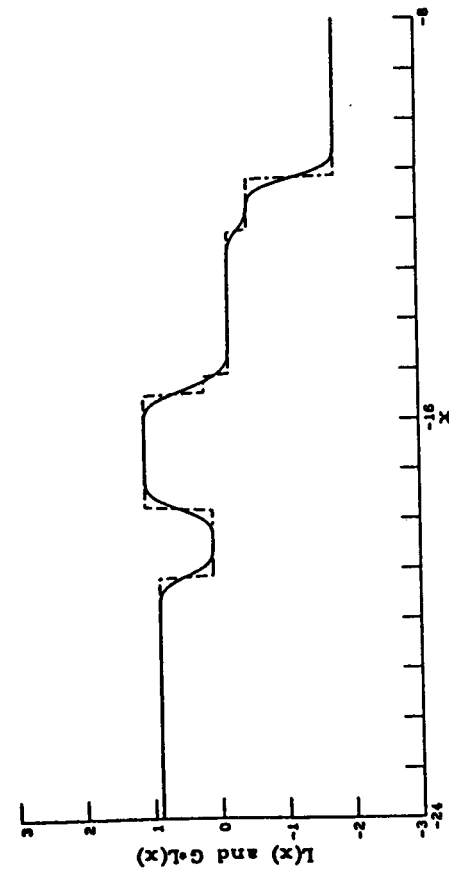
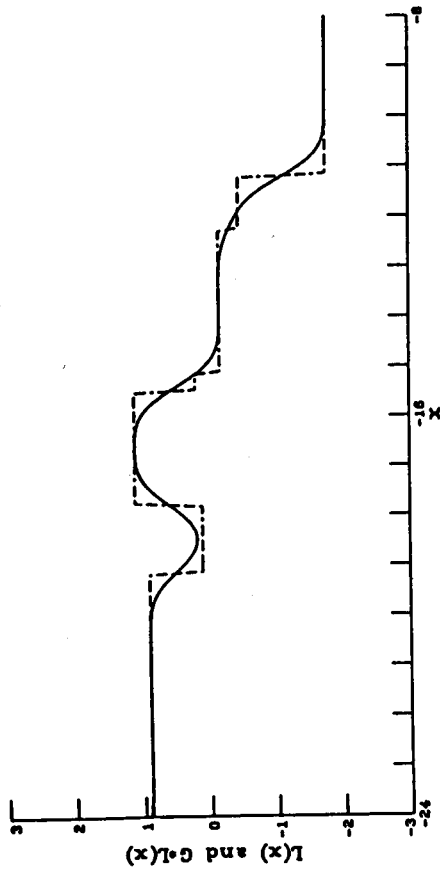


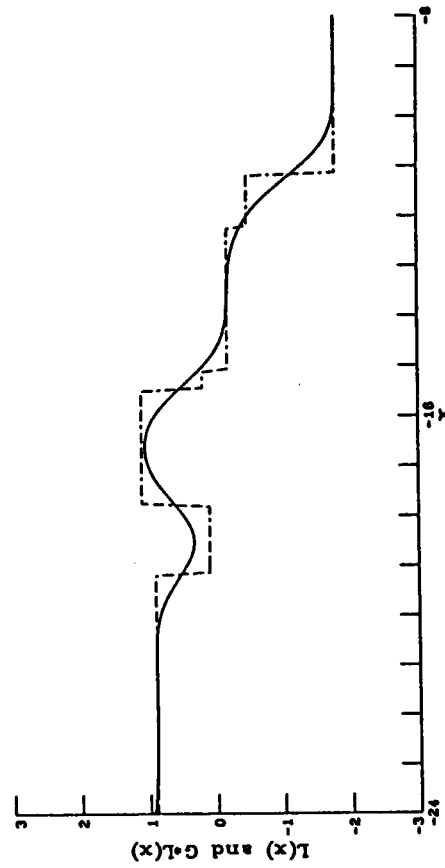
FIGURE 1. Basic block diagram for problem formulation.



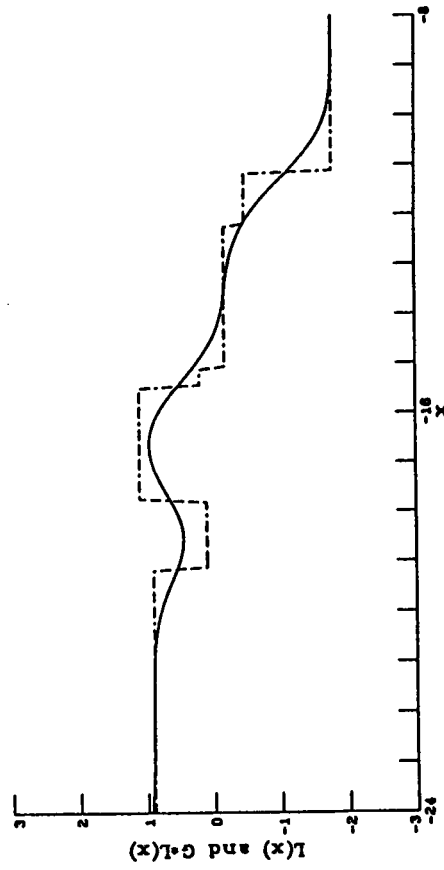
(a) $\beta = .2$



(b) $\beta = .4$



(c) $\beta = .6$



(d) $\beta = .8$

FIGURE 2. Smoothing of small detail by convolving scene radiance $L(x)$ with a Gaussian kernel, G_β , of standard deviation β .

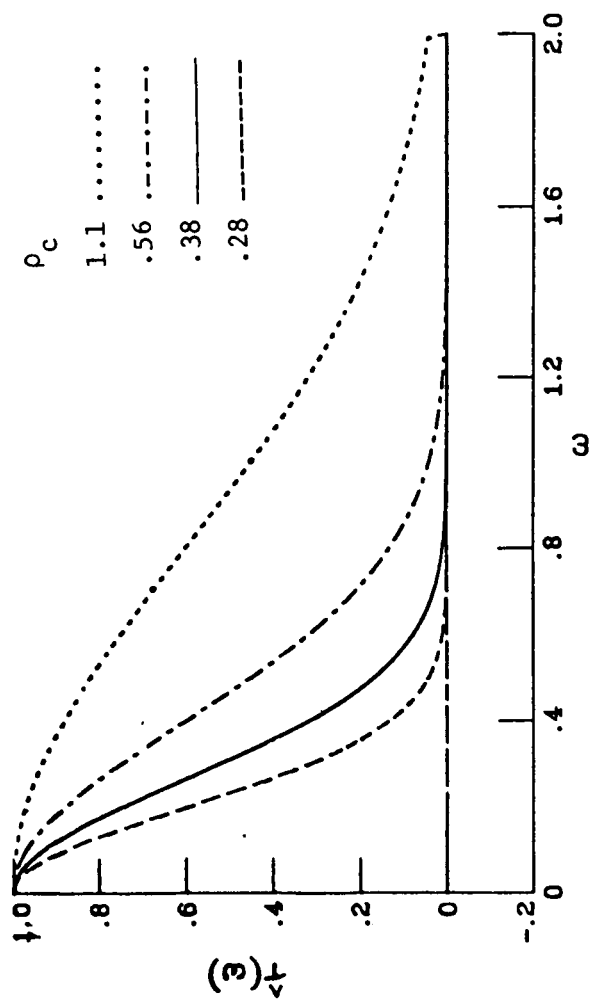
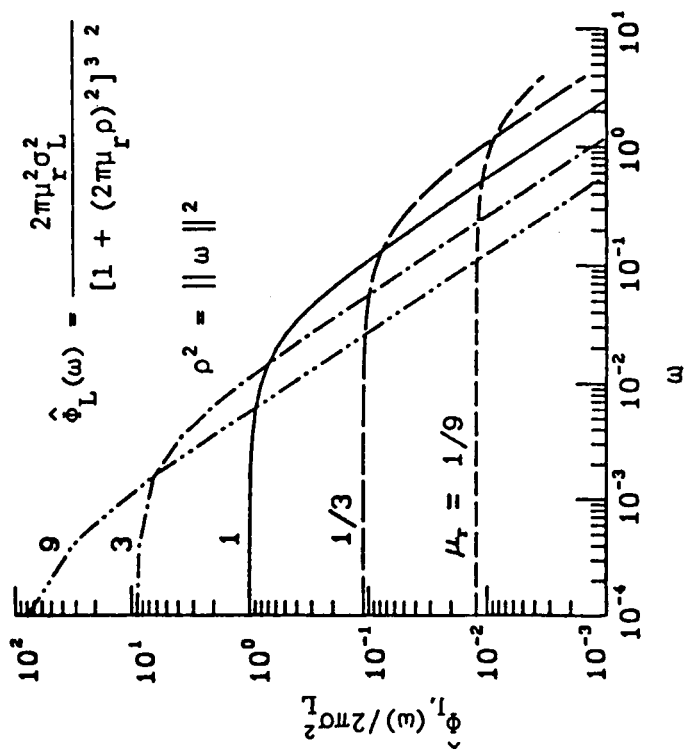


FIGURE 3. Sensor (OTF) responses

FIGURE 4. Scene power spectra for various levels of detail, μ_r

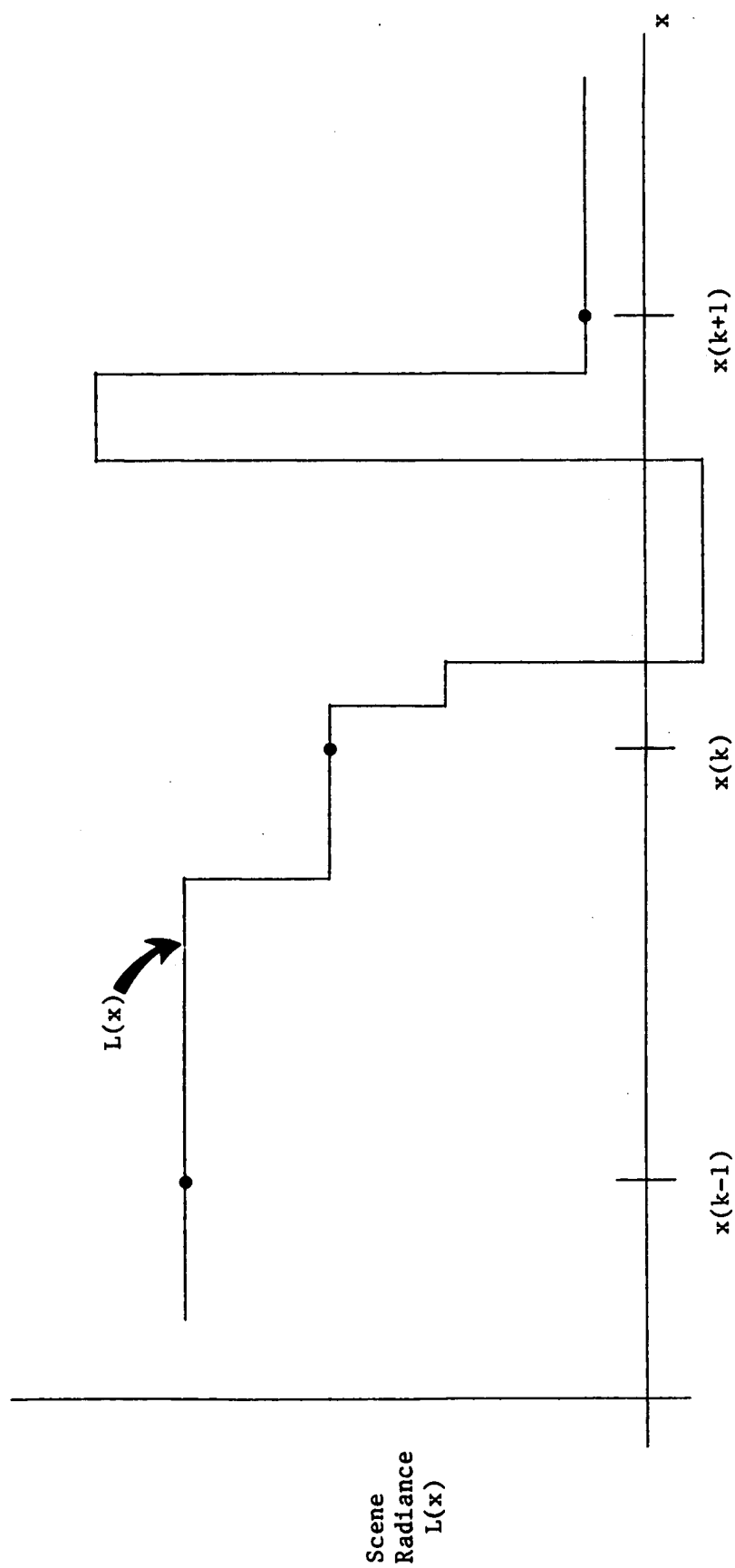


FIGURE 5. Example of undersampling.

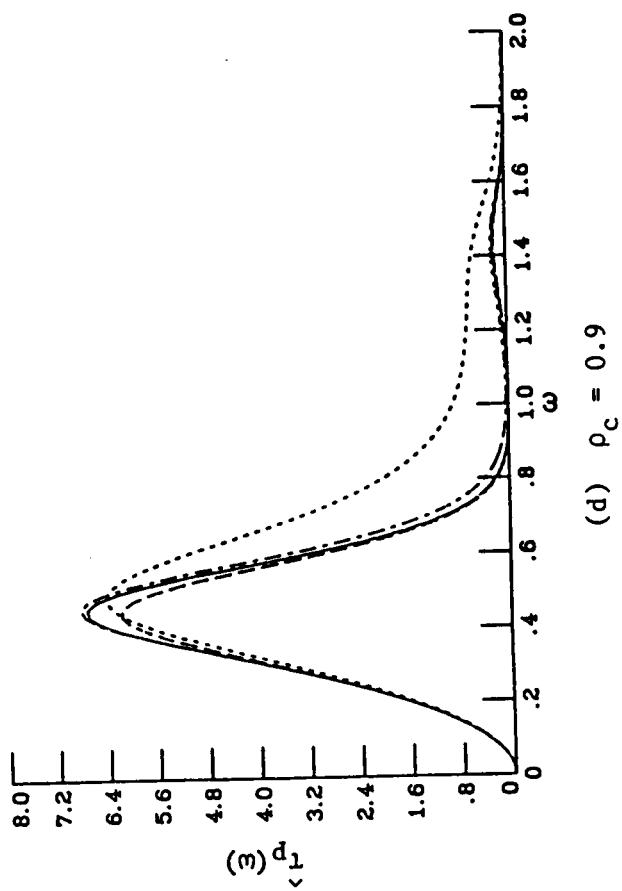
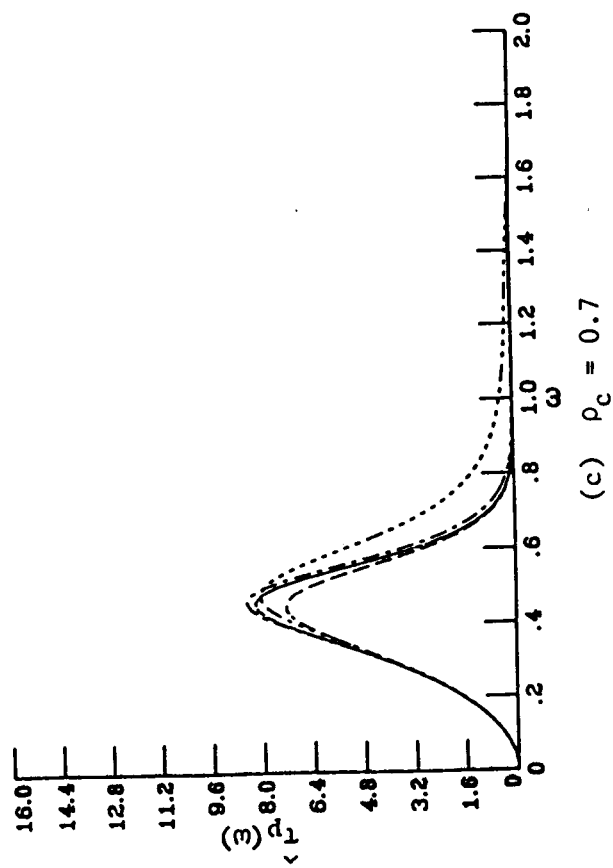
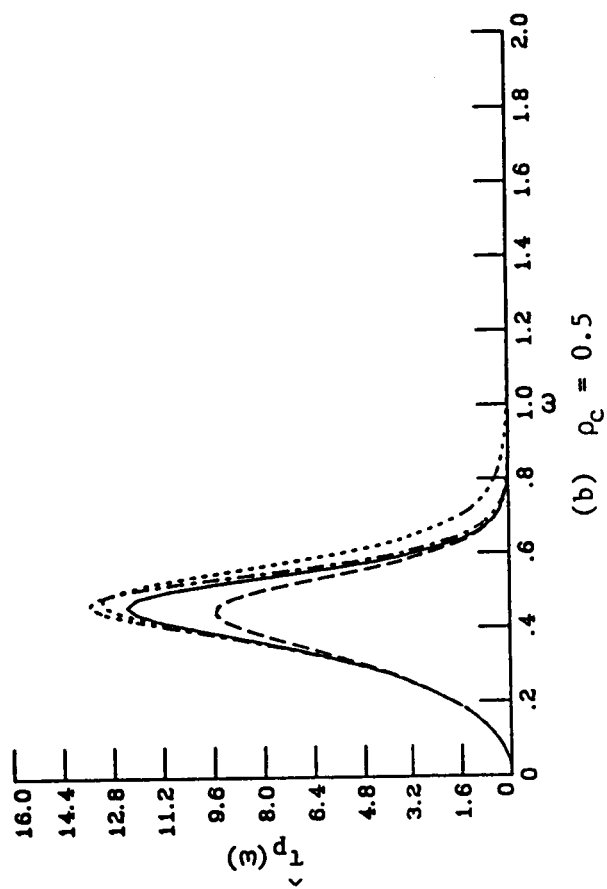
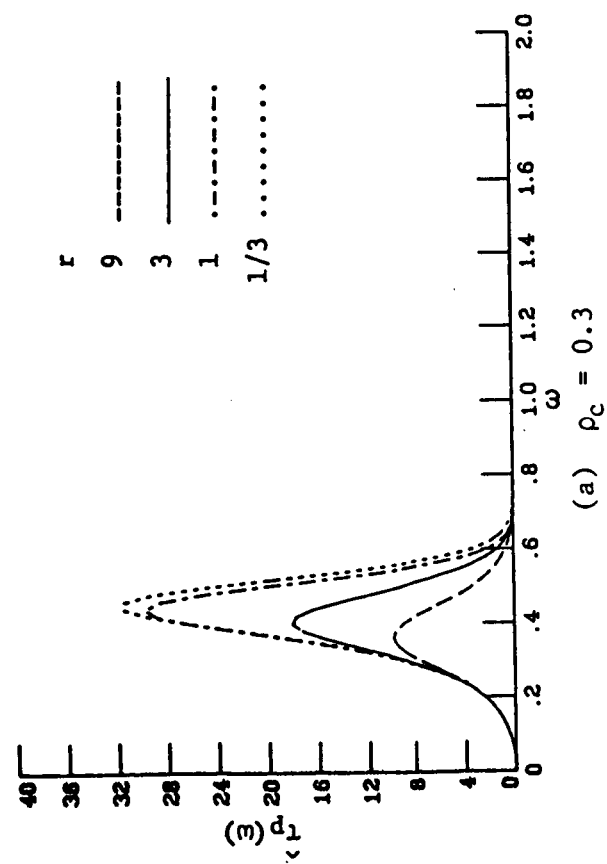


FIGURE 6. Optimal edge detector using ∇^2

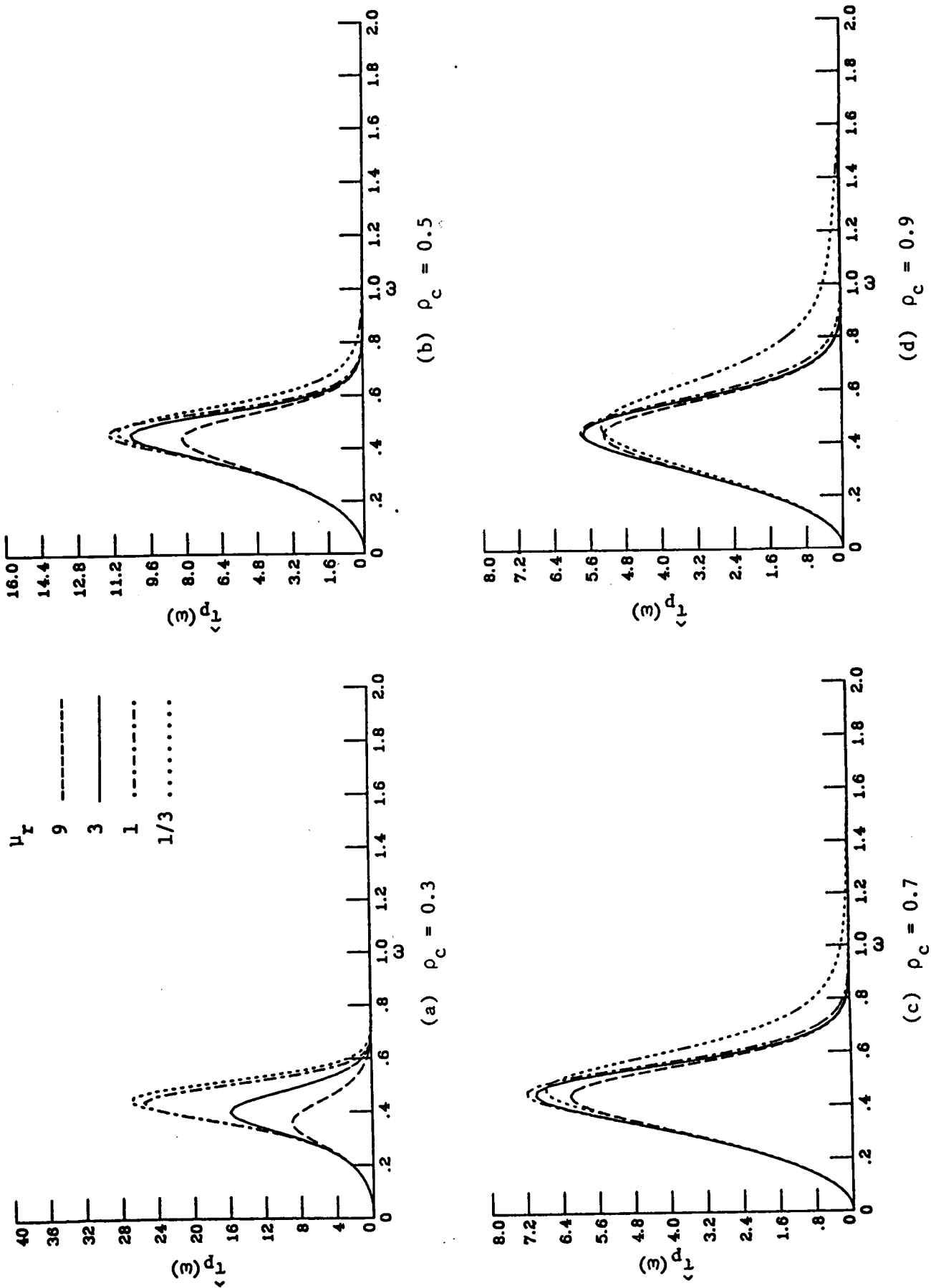
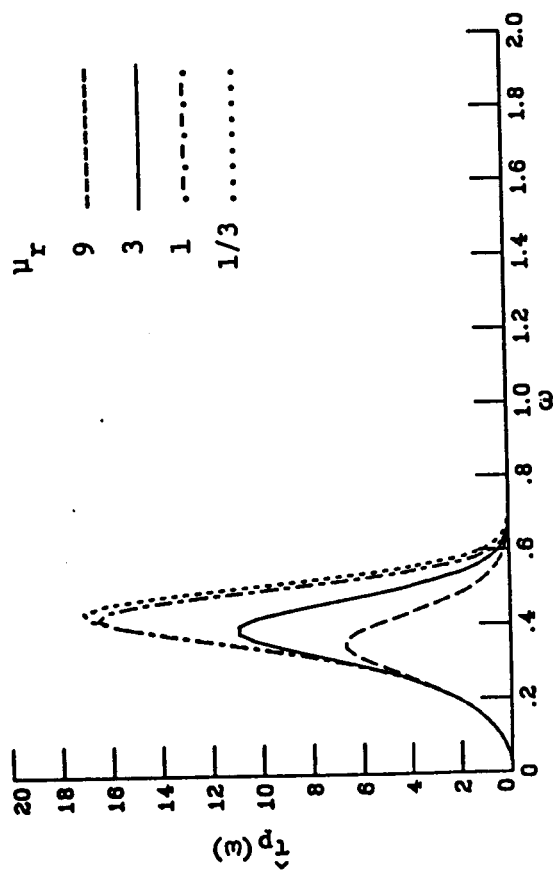
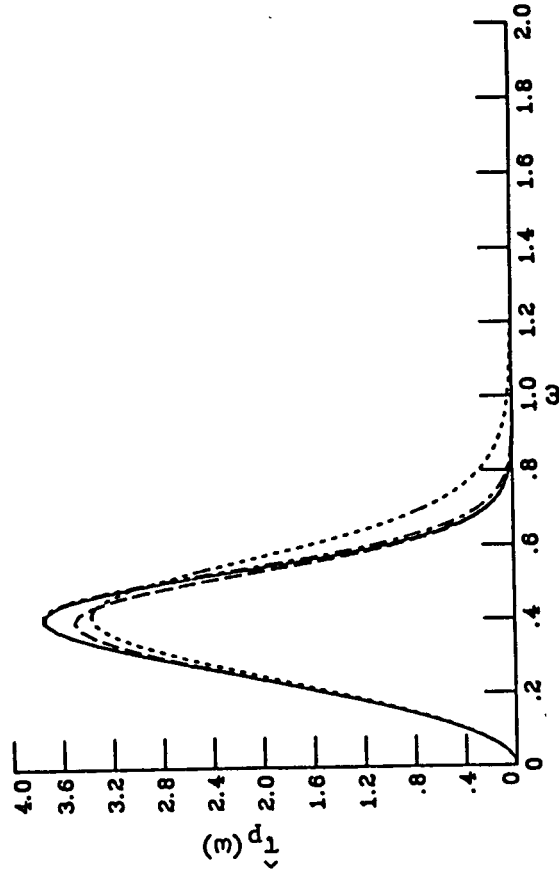


FIGURE 7. Optimal edge detector using $V^2 G_\beta$, $\beta = .2$



(b) Processor vs. scene for $\rho_e = 0.5$



(d) Processor vs. scene for $\rho_e = 0.9$

FIGURE 8. Optimal edge detector using $\nabla^2 G_\beta$, $\beta = .4$

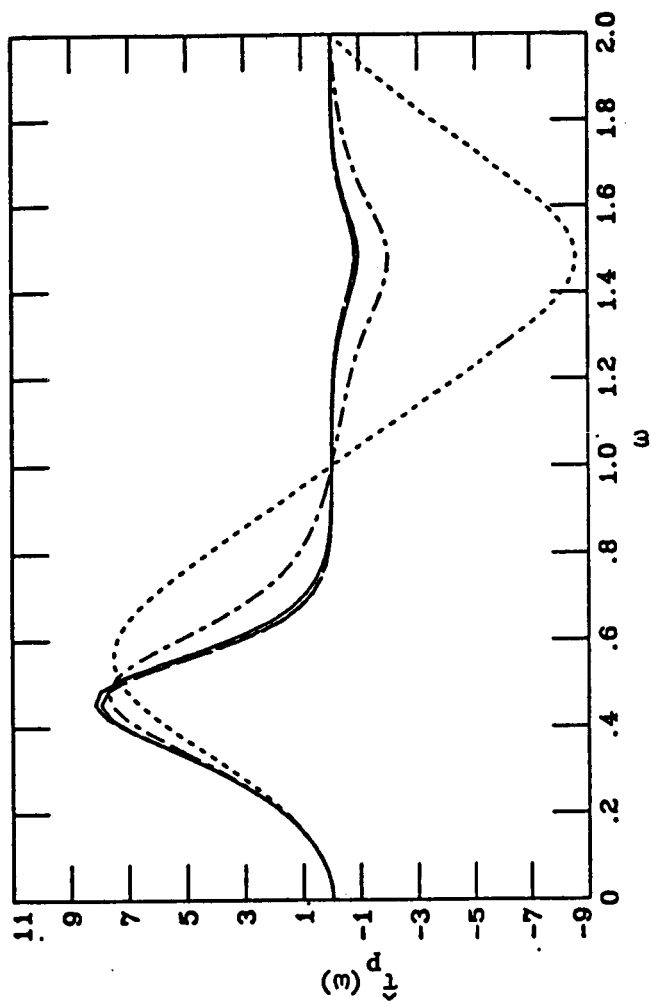


FIGURE 9. Optimal edge detector using V^2 and square aperture.

SQUARE SAMPLING

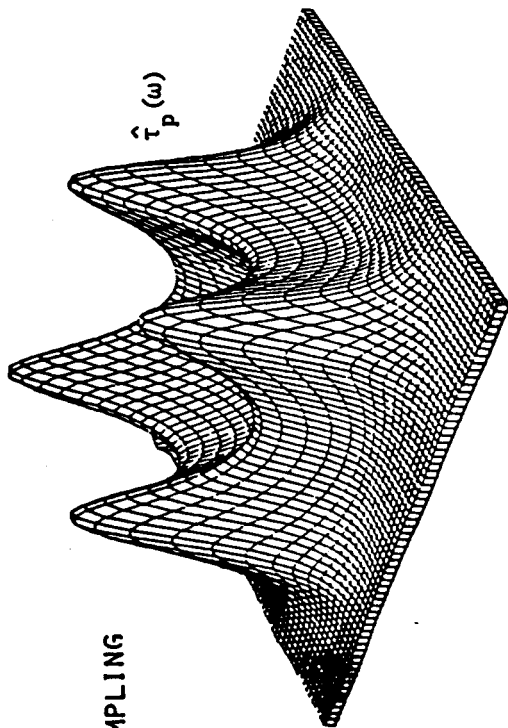


FIGURE 10. Optimal edge detector transfer function perspective plot for $\sqrt{2} S/N = 32$, $\mu_r = 1$, $\rho_c = .38$

HEXAGONAL SAMPLING

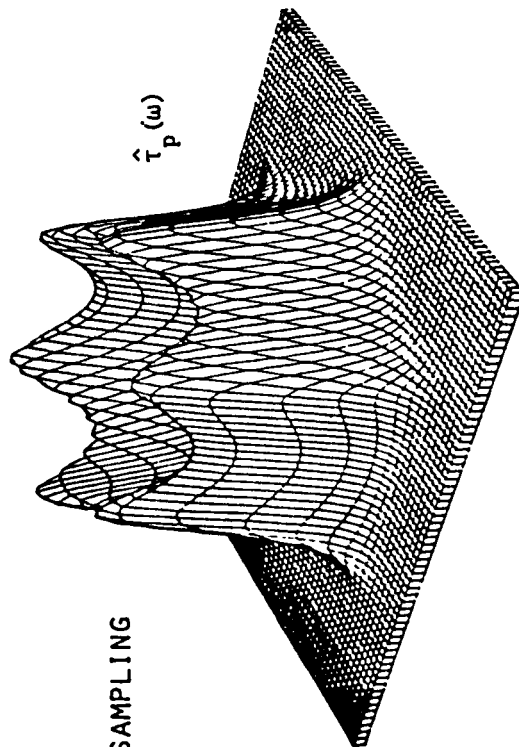


FIGURE 11. Optimal edge detector transfer function perspective plot for $\sqrt{2} S/N = 32$, $\mu_r = 1$, $\rho_c = .38$

SQUARE SAMPLING
SQUARE APERTURE

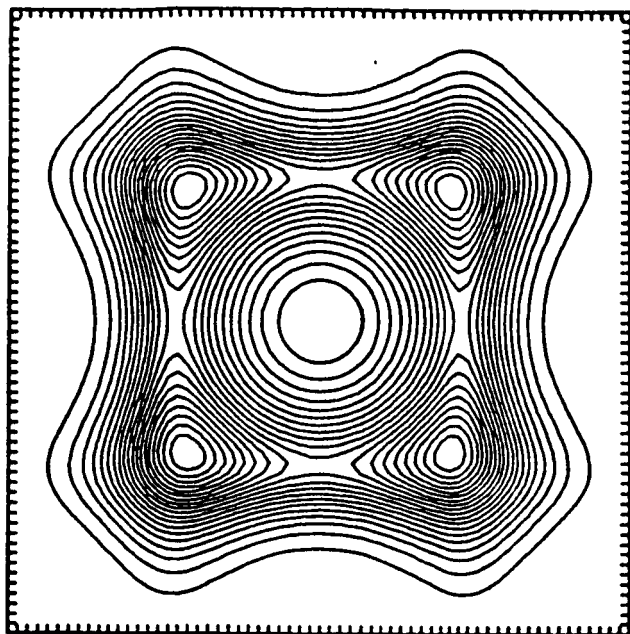
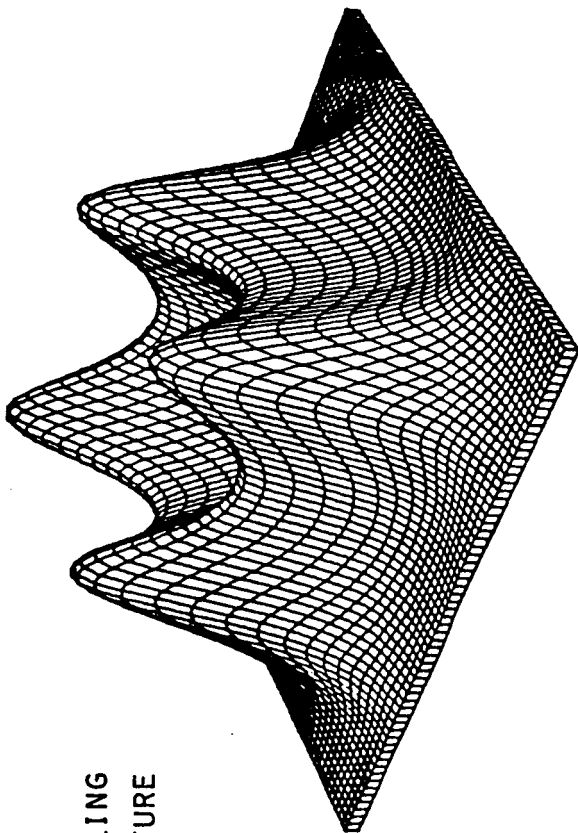
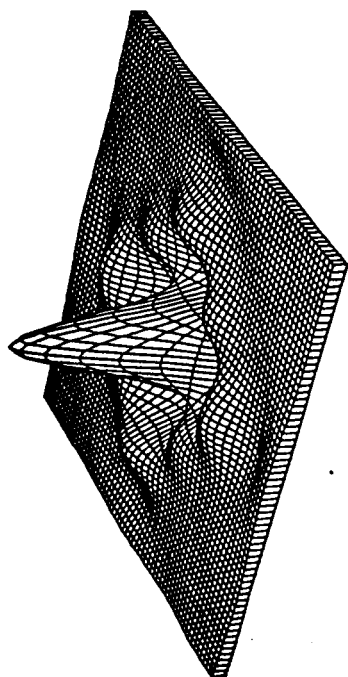
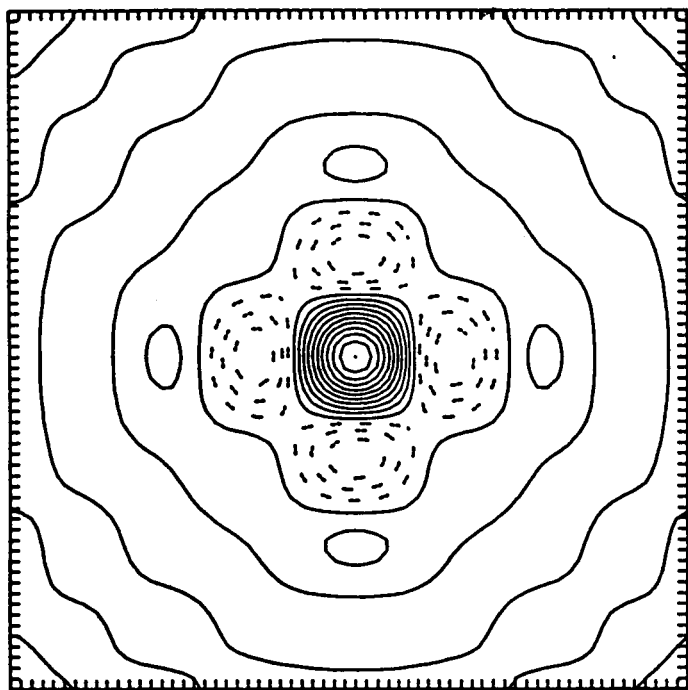


FIGURE 12. Optimal edge detector transfer function perspective plot for $\sqrt{2} S/N = 32$, $\mu_T = 1$



(a) perspective plot



(b) contour plot

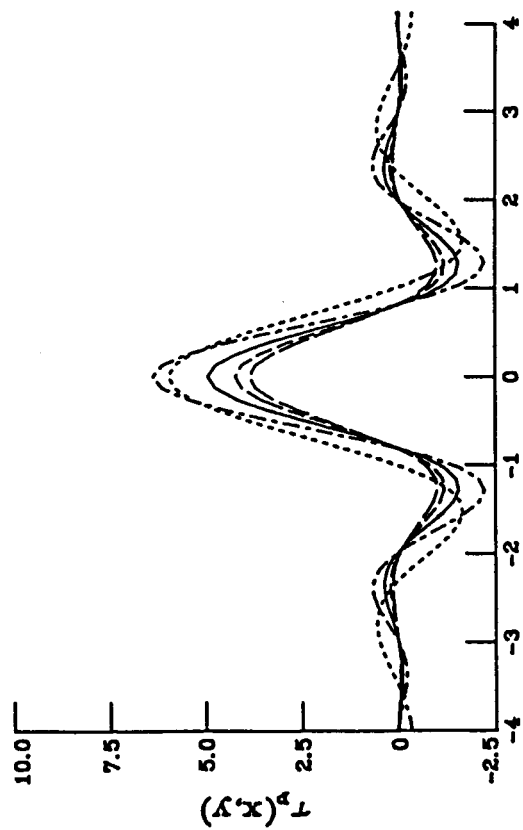
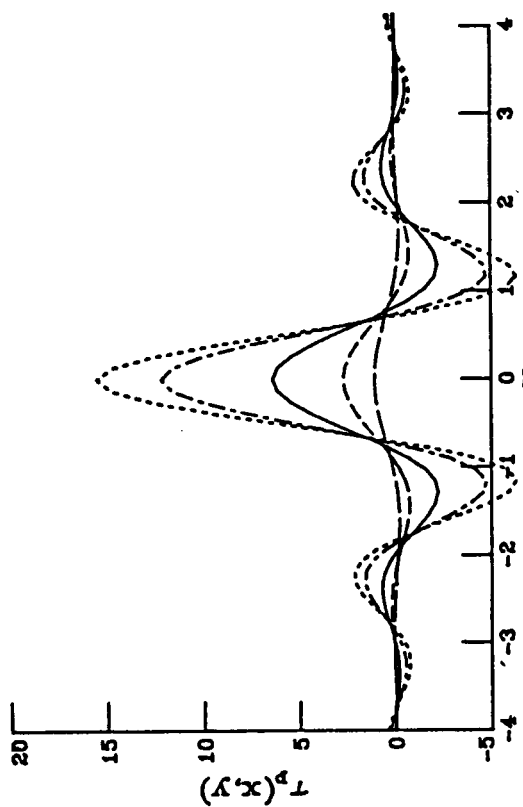
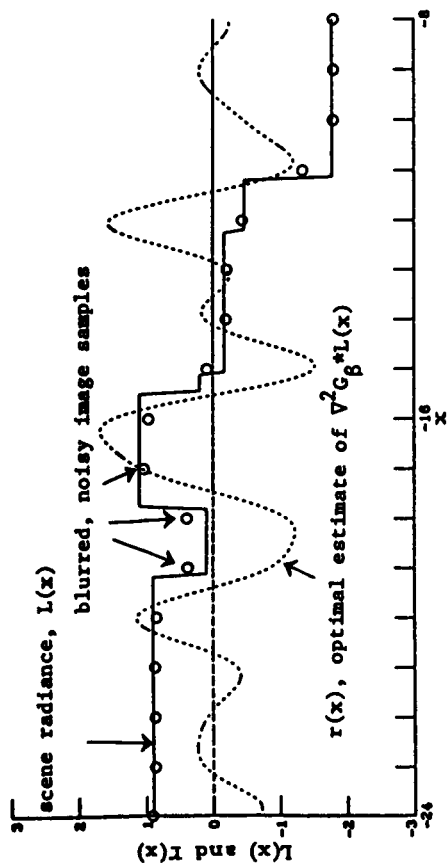
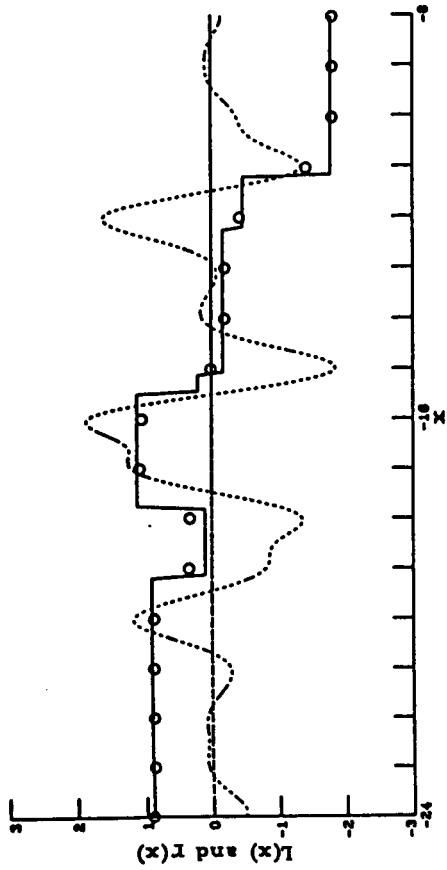
(c) cross-sections for various sensor OTF's $\rho_c = .3, .5, .7, .9, .11, \beta = .4$ (d) cross-sections for various levels of detail, $\nabla^2 G_\beta, \beta = 0, .2, .4, .6, .8$

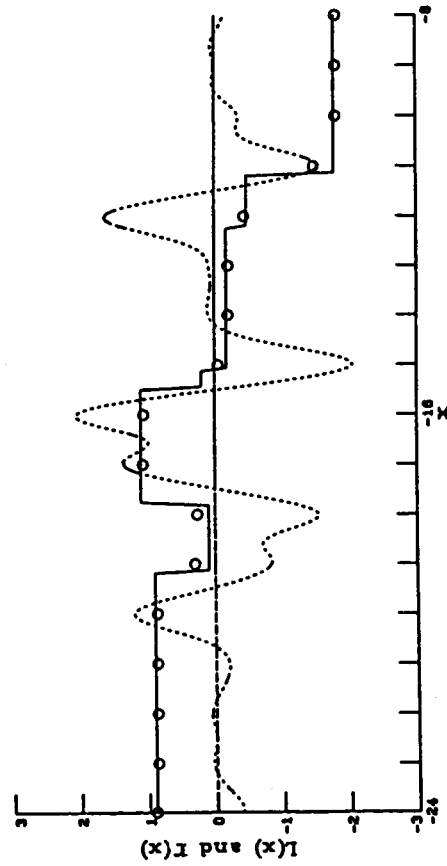
FIGURE 13. Optimal edge detector point spread function.



(a) Samples from gathering system with $\rho_c = 0.5$



(b) Samples from gathering system with $\rho_c = 0.7$



(c) Samples from gathering system with $\rho_c = 0.9$

FIGURE 14. 1-D Simulations of optimal edge detectors for $\frac{d^2}{dx^2} G_\beta$, $\beta = .2$

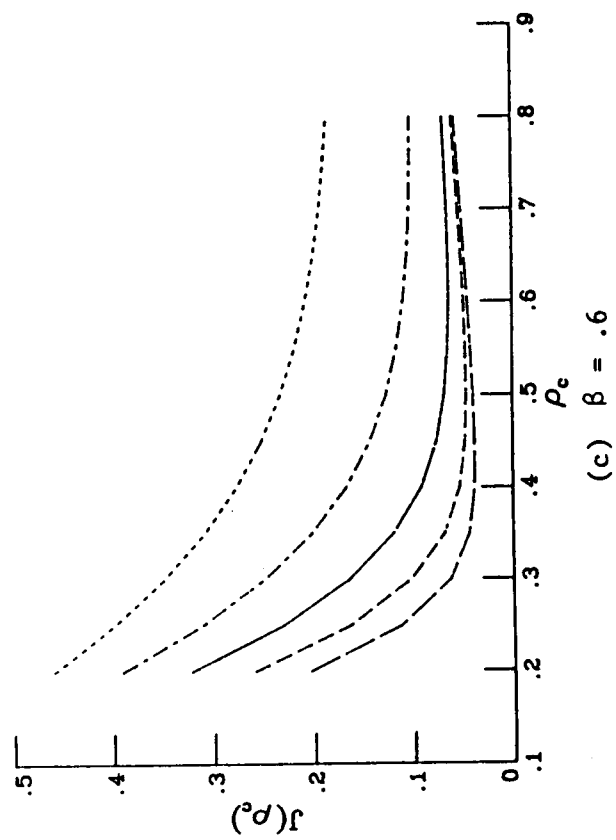
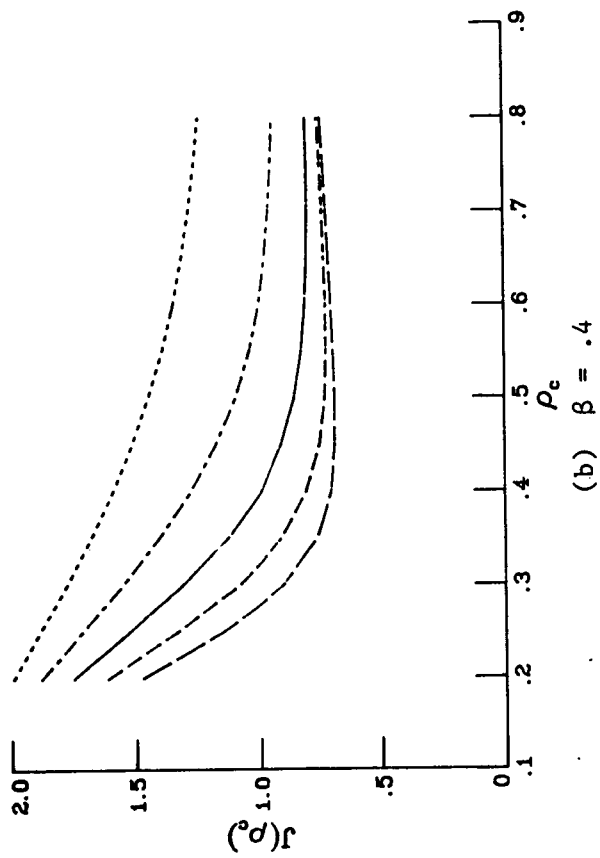
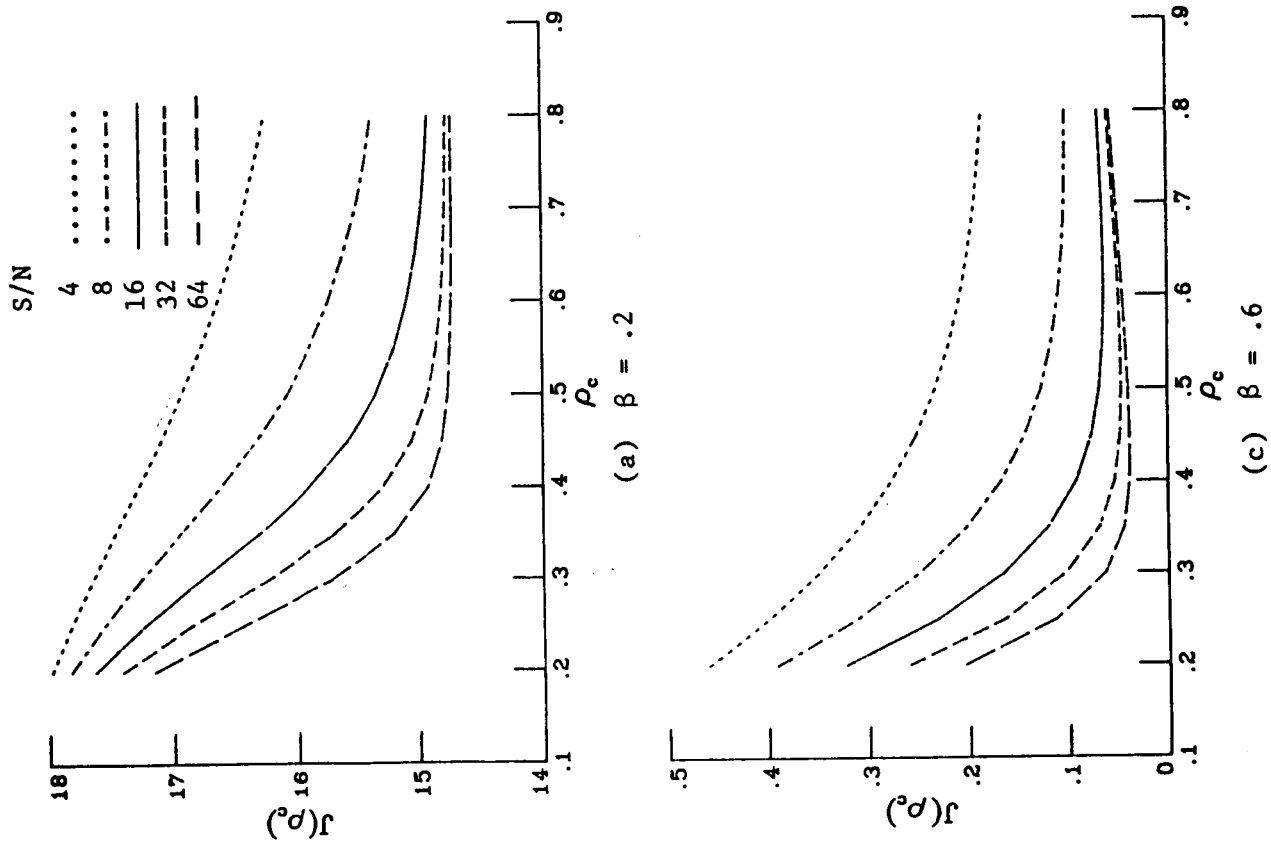


FIGURE 15. Mean-squared error versus OTF cut-off frequency for $\nabla^2 G_\beta$ and $\mu_r = 3$.

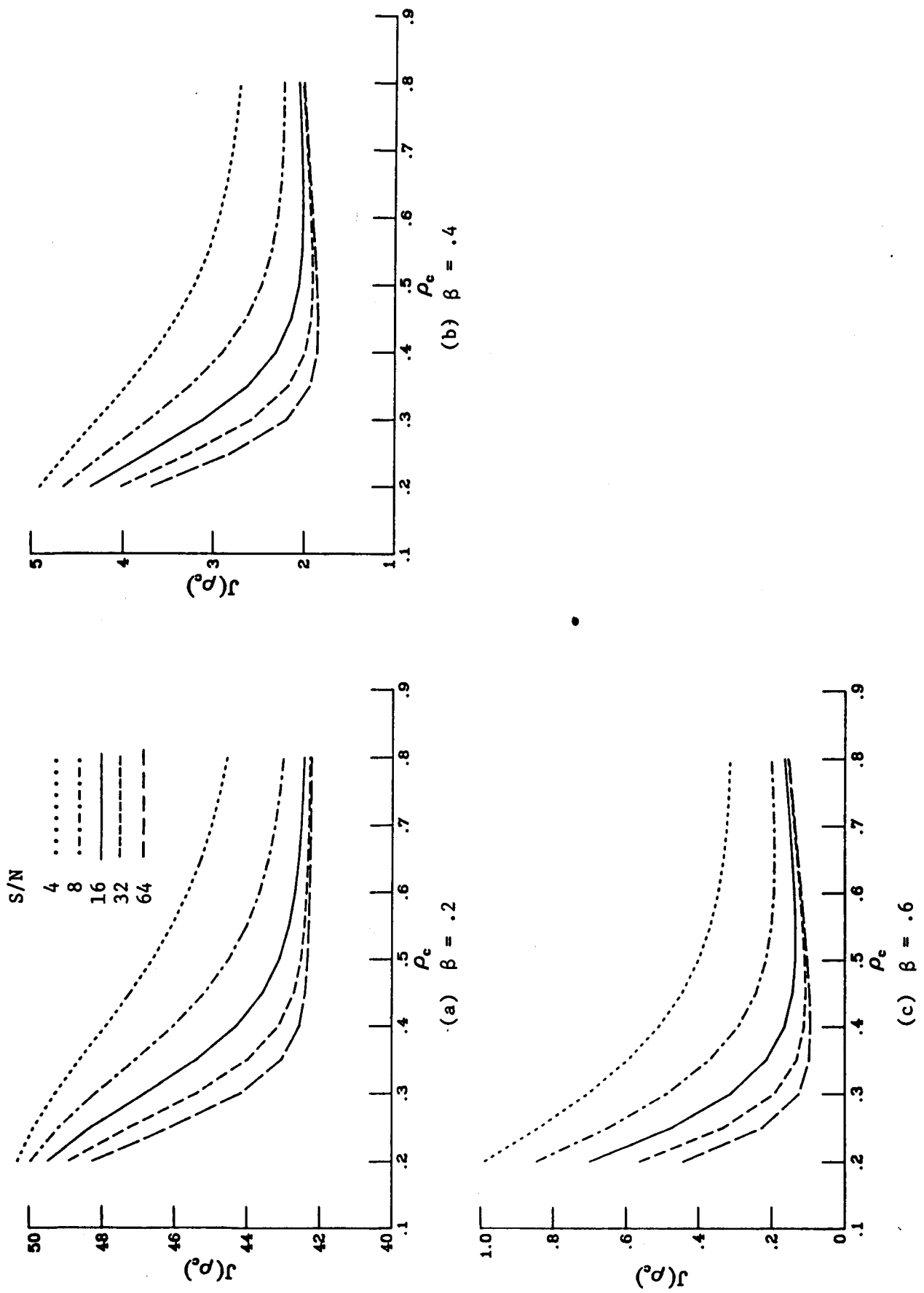


FIGURE 16. Mean-squared error versus OTF cut-off frequency for V_G^2 and $\mu_r = 1$.

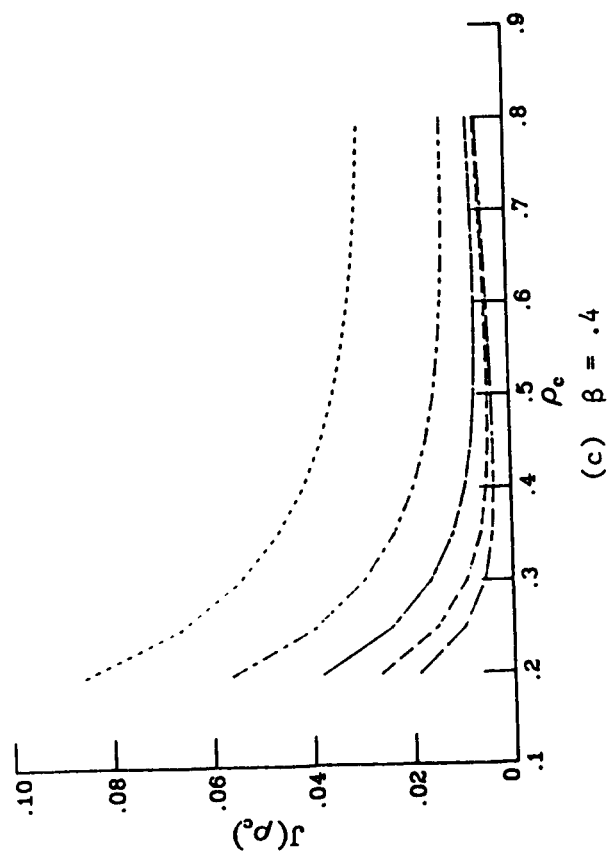
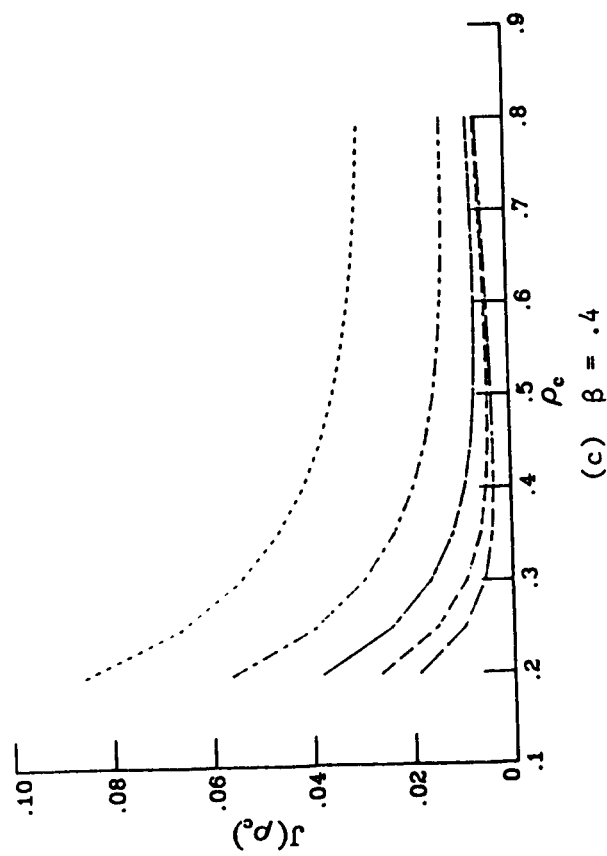
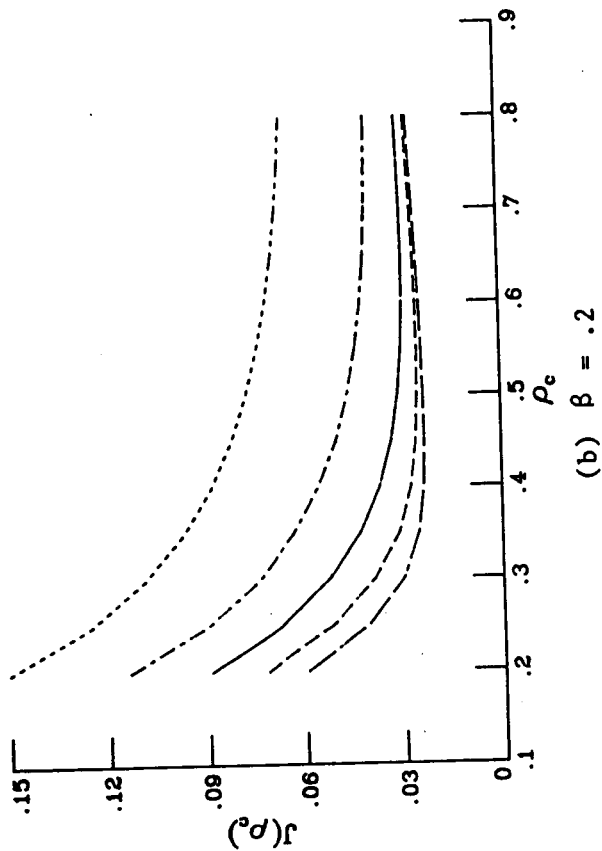
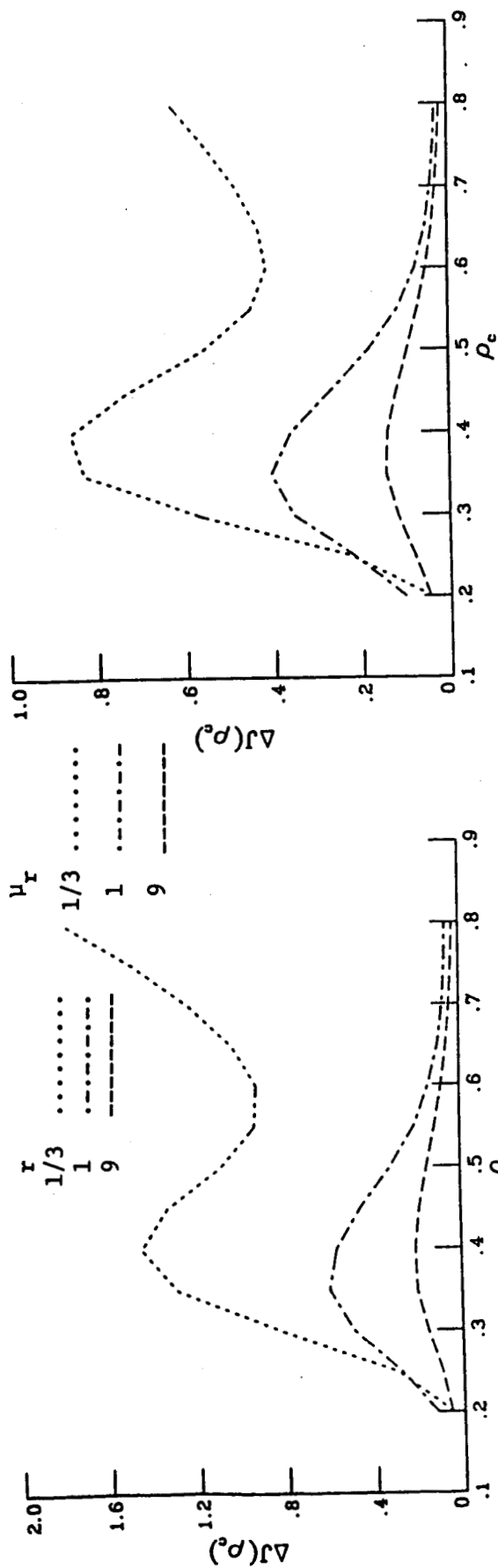
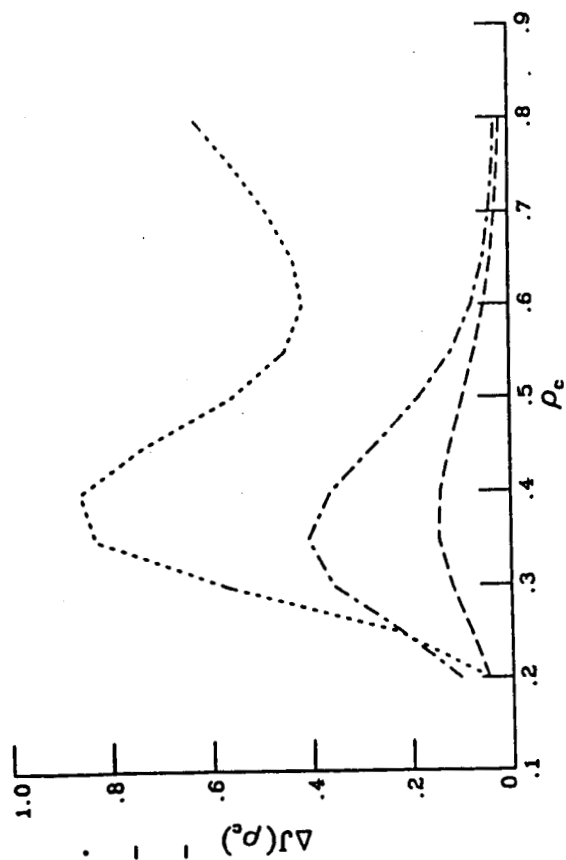


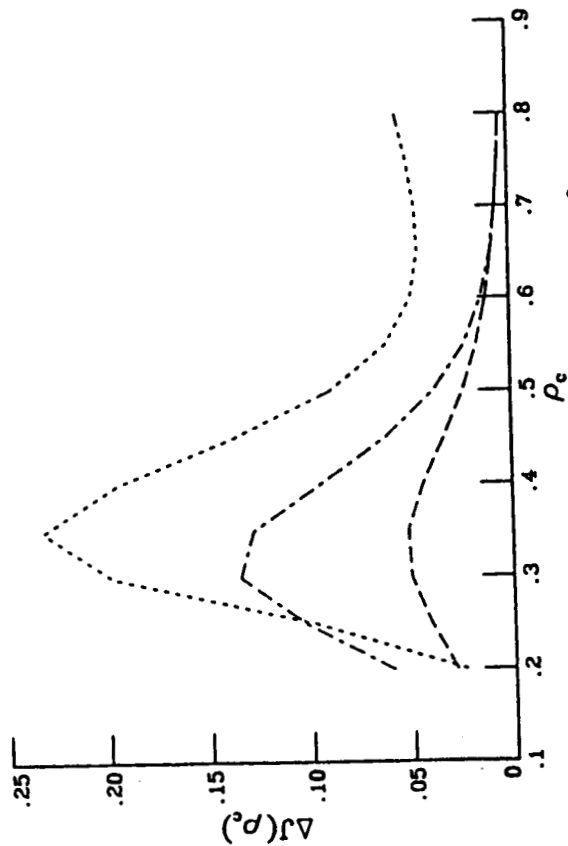
FIGURE 17. Mean-squared error versus OTF cut-off frequency for scene reconstruction $G_{\beta}^* L$ and $\mu_r = 3$.



(a) Cost vs. scene change for $V^2_{G\beta}$, $\beta = 0$.



(b) Cost vs. scene change for $V^2_{G\beta}$, $\beta = .2$



(c) Cost vs. scene change for $V^2_{G\beta}$, $\beta = .4$

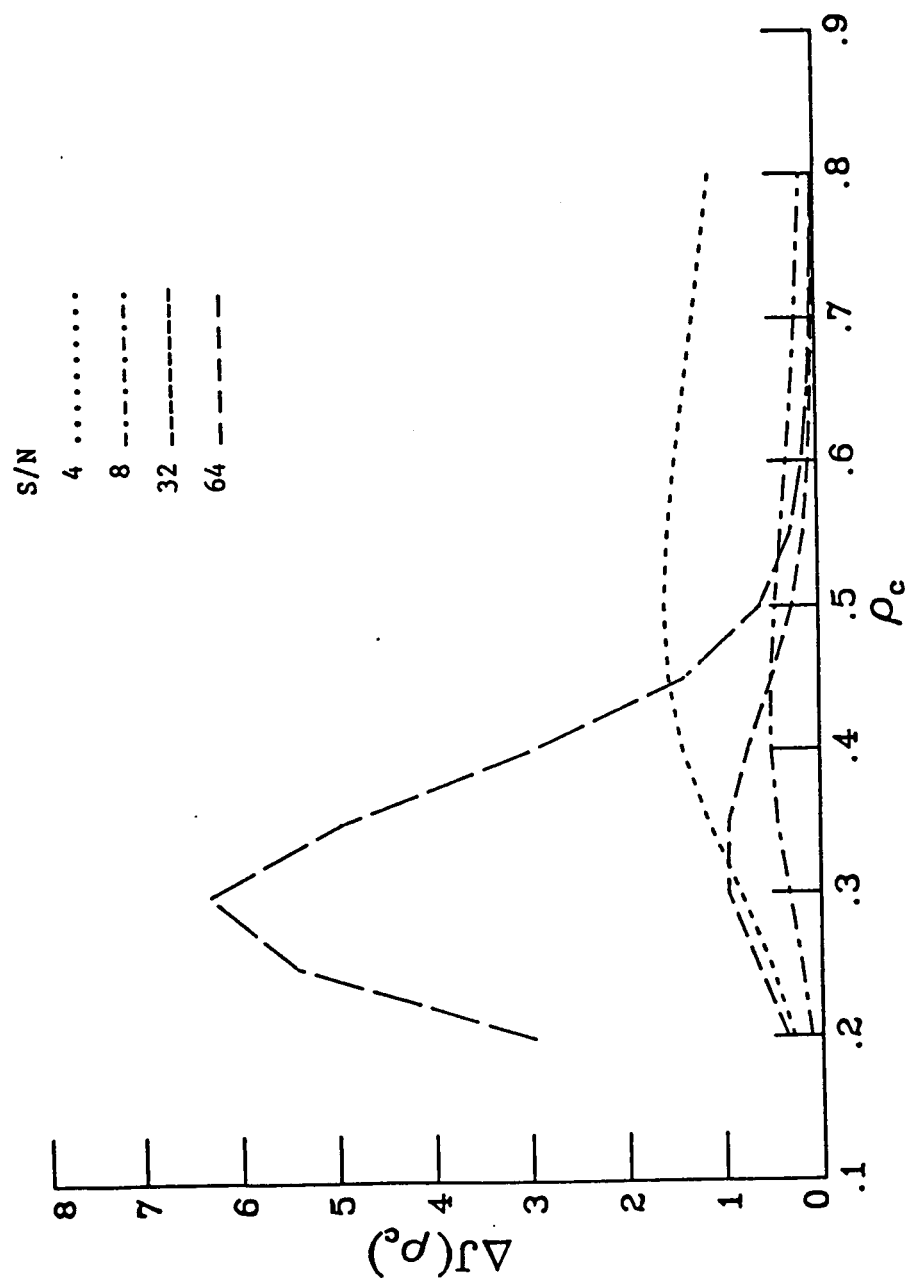


FIGURE 19. Sensitivity to uncertainties in the actual signal-to-noise ratio S/N ; design based on S/N of 16.

CHAPTER II.

EFFECTS OF ELECTRICAL FILTERING ON IMAGE-GATHERING AND IMAGE-PROCESSING SYSTEM OPTIMIZATION FOR EDGE DETECTION

ABSTRACT

This paper investigates the effects of phase distortion due to on-line electrical filtering in the image-gathering system, and extends the results of Chapter I on the combined optimization of image-gathering and image-processing in estimating a scene characteristic or feature. An effective image-gathering point-spread function (PSF) including the effects of both electrical and optical systems is developed. It is shown that the phase distortion appears in the effective image-gathering PSF as a shift in the location of the PSF maximum, an asymmetry about the maximum and a decaying "tail" which effectively widens the sensor's footprint. The edges of the acquired image are not only blurred, but also shifted in position along the scan direction. This effect further stresses the importance of the combined image gathering and processing approach. It is shown that the optimal image processor compensates for both phase and magnitude distortion in the image to the extent compatible with noise attenuation, and continues to display a lack of circular symmetry while being highly influenced by the sampling lattice used in image acquisition. Finally, it is shown that the spatially averaged mean-squared error and its sensitivity to variations in the scene detail and noise statistics are both independent of the image-gathering system phase characteristics, when the optimal image processor is used to correct magnitude and phase distortion.

1. INTRODUCTION

The performance of line-scan imaging systems has received considerable attention in the electro-optical system design literature [1] - [12]. Line-scan imaging systems, such as TV cameras and optical-mechanical scanners generally use on-line electrical filtering to shape the image-gathering system characteristics along the scan direction. The usual considerations in selecting the electrical filtering to be performed involve the trade-off between the reduction of noise and aliasing effects by filtering out high frequencies and the blurring introduced by the attenuation of high frequency detail.

Whereas the effects of blurring due to the attenuation of certain frequency bands, or transfer function magnitude effects, have been investigated (e.g., [12], [13]), the effects of blurring due to the phase distortion introduced by the electrical transfer function have received little attention in the literature.

Due to the symmetry in the aperture of most designs, optical system transfer functions are real functions and have zero phase, except for optical aberrations. On the other hand, on-line electrical filter transfer functions are complex functions and have non-zero phase. The transfer function of the overall image-gathering system thus becomes complex with non-zero phase characteristics, and results in a phase distortion of the image.

In this paper, the effects of electrical filter phase distortion on the image-gathering system transfer function, the image and the optimal image processor are investigated. The methodology of combined optimization of image-gathering and image-processing used in this paper follows the same lines as the one introduced in [14]. The results of [14] are extended to image-gathering systems which have non-zero phase.

As shown in Figure 1, the image-gathering system consists of the optical transfer function, $\hat{t}_o(\nu, \omega)$, which usually has zero phase, the electrical filter transfer function, $\hat{h}_e(\omega')$, where ω' is the temporal frequency variable while ν and ω represent the spatial

frequency variables, the sampling process and additive noise or, more generally, sensor errors. The image-gathering system is followed by the image processor, $\hat{r}_p(\nu, \omega)$, which produces the overall system output, $r(x, y)$.

The objective is to determine a spatial characteristic or feature of the scene rather than a characteristic of the image data which contains the effects of blurring due to both magnitude and phase distortion and has been contaminated by noise. The class of spatial characteristics considered here consists of characteristics which can be obtained from the observed radiance field by a linear operator. The image processor uses the sampled image data to estimate the desired scene characteristic. The optimal image processor must compensate for the magnitude and phase distortion introduced by the image-gathering system, the aliasing effects introduced by the sampling lattice and the sensor noise.

In Section 2, the effects of the electrical filter or, more generally, the effects of temporal processing, are modeled in terms of spatial processing characteristics. Combined with the optical transfer function, this results in an overall image-gathering transfer function which is complex, therefore producing both magnitude and phase distortion in the image acquired. This effective point-spread-function (PSF) of the image gathering system is shown to be shifted away from the origin and to have a "tail" along the same axis. The effective PSF shows that the edges in the image will be shifted relative to the location of the edges in the scene, due to the phase distortion. It is also seen that the tail of the effective PSF will produce a further blurring effect.

In Section 3, the optimal image processor for image-gathering systems with non-zero phase is investigated. It is seen that, in order to eliminate (minimize) phase distortion, the optimal image processor must have exactly the opposite phase as the image-gathering PSF. The magnitude characteristics of the optimal image processor are seen to be the same as for image-gathering systems with no phase distortion. In particular, it is seen that as in [14], the optimal edge detector is not circularly symmetric due to the effect of the sampling lattice used in image acquisition.

In Section 4, the spatially averaged mean-squared difference between the scene characteristic desired and the system output is considered. It is shown that the spatially averaged mean-squared error is independent of the phase characteristics of the image-gathering scene when the optimal image processor is used, irrespective of the scene characteristic or feature being estimated. It is also shown that the sensitivity of the optimal image-gathering system to variation (or uncertainties) in the scene and noise statistics is also independent of the phase characteristics of the image gathering system, as long as the optimal image processor is used. Therefore, the magnitude characteristics of the optimal image-gathering system obtained in [14] remain valid for non-zero phase image acquisition, as long as the optimal image processor is used.

2. EFFECTIVE IMAGE-GATHERING SPATIAL RESPONSE

To model the effects of electrical filtering (or processing) on the overall electro-optical system, we will consider a scanner where the scanning axis, say y , is perpendicular to the x -axis in which the relative motion of the scanner center of mass and the scene occurs. Other types of scanning strategies can be analyzed and modeled in a similar fashion, but will not be treated here. As shown in Figure 1, the electrical filtering is actually performed on the analog signal which is obtained by the optical system. Thus, the scanning axis, y , runs along the time axis. We will assume that the scanner's relative motion along the x -axis is much slower in comparison to the scanning motion of the optical axis. In other words, the scanning speed is assumed to be much faster than the relative motion of the device.

Let $h_e(t)$ be the impulse response of the electrical filter processing the signal obtained by the Optical Transfer Function (OTF), $\hat{\tau}_o(\nu, \omega)$. Thus, the Electrical Transfer Function (ETF), $\hat{h}_e(\omega')$, is given by the usual one-dimensional Fourier transform

$$\hat{h}_e(\omega') = \int_{-\infty}^{\infty} h_e(t) e^{-2\pi i \omega' t} dt \quad , \quad (1)$$

where ω' is the temporal frequency variable in units of cycles per sec. In most continuous scan systems, the electrical processing used is low-pass filtering with the ETF corresponding to standard low-pass filters such as the Butterworth, Tchebycheff, Bessell filters.

The input-output relationship of the electrical filter is given by the one-dimensional convolution

$$o(t) = \int_{-\infty}^{\infty} h_e(t') i(t - t') dt' \quad , \quad (2)$$

where $i(t)$ and $o(t)$ are the input and output signals, respectively. It is assumed here that transient effects due to initial conditions have died down to negligible levels.

On the other hand, when the optical axis points along (x, y) , the optical system input-output relationship is given by the two-dimensional convolution

$$g(x, y) = \int_{-\infty}^{\infty} \int_{-\infty}^{\infty} \tau_o(x', y') L(x - x', y - y') dx' dy' \quad (3)$$

where $L(x, y)$ is the scene radiance input to the sensor and $g(x, y)$ is the output, and $\tau_o(x, y)$ is the optical Point Spread Function (PSF) corresponding to the OTF, $\hat{\tau}_o(\nu, \omega)$.

Now suppose that, at time t , the optical axis points along $(x(t), y(t))$ producing the signal $g(x(t), y(t))$. Then, the analog output of the electrical filter is given by

$$s(x(t), y(t)) = \int_{-\infty}^{\infty} h_e(t') g(x(t - t'), y(t - t')) dt' \quad , \quad (4)$$

where the output of the electronics, $s(x(t), y(t))$, has been associated with the optical axis direction $(x(t), y(t))$ rather than simply time, t .

As mentioned earlier, the scanning motion along y is much faster than the motion along x . Thus, we assume that $y(t - t')$ varies along the scan direction, while $x(t - t')$ remains essentially unchanged over the period of a scan; i.e.,

$$x(t - t') \approx x(t) \quad , \quad (5)$$

$$y(t - t') = \dot{y}(t - t') = \dot{y}t - \dot{y}t' \quad , \quad (6)$$

when $t - t'$ is of the order of a scan period, but is much larger than the electrical filter time constants, and where \dot{y} is the linear scan rate. Substituting (5) and (6) into (4) and manipulating,

$$\begin{aligned}
s(x(t), y(t)) &= \int_{-\infty}^{\infty} h_e(t') g(x(t), \dot{y}t - \dot{y}t') dt' \\
&= \frac{1}{\dot{y}} \int_{-\infty}^{\infty} h_e\left(\frac{y'}{\dot{y}}\right) g(x(t), y(t) - y') dy'
\end{aligned} \tag{7}$$

$$= \int_{-\infty}^{\infty} \int_{-\infty}^{\infty} \tau_e(x', y') g(x(t) - x', y(t) - y') dx' dy' \tag{8}$$

where

$$y' = \dot{y}t' \quad , \tag{9}$$

$$\tau_e(x', y') = \frac{1}{\dot{y}} h_e\left(\frac{y'}{\dot{y}}\right) \delta(x') \quad , \tag{10}$$

and $\delta(x')$ is the Dirac delta function.

It is seen that the effect of the electrical filter in the spatial domain can be expressed by the PSF $\tau_e(x', y')$ and a two dimensional convolution, as shown in (8).

Taking the 2-D Fourier transform of (8), and using (3),

$$\hat{s}(\nu, \omega) = \hat{\tau}_e(\nu, \omega) \hat{g}(\nu, \omega) = \hat{\tau}_e(\nu, \omega) \hat{\tau}_o(\nu, \omega) \hat{L}(\nu, \omega) . \tag{11}$$

Taking the Fourier transform of (10), and manipulating,

$$\hat{\tau}_e(\nu, \omega) = \hat{h}_e(\dot{y}\omega) = \hat{\tau}_e(\omega) \quad , \tag{12}$$

where ω is the spatial frequency variable corresponding to the scan direction; i.e., the y-axis. It should be noted that since $\hat{\tau}_e$ varies only with ω and is independent of ν , we will treat it as a function of ω alone to emphasize this fact.

From (11) and (12), it is seen that the effective OTF for the combined electro-optical system is given by

$$\hat{\tau}(\nu, \omega) = \hat{\tau}_e(\omega) \hat{\tau}_o(\nu, \omega) = \hat{h}_e(\dot{y}\omega) \hat{\tau}_o(\nu, \omega) \quad , \quad (13)$$

where \hat{h}_e is the temporal transfer function of the electrical filter, and \dot{y} is the scan rate. Thus, given $\hat{h}_e(\omega')$ and the scan rate, it is a simple matter to obtain the effective spatial OTF.

Similarly, it can be shown that the effective system PSF, $\tau(x, y)$, can be obtained as a one-dimensional convolution.

$$\tau(x, y) = \int_{-\infty}^{\infty} \frac{1}{\dot{y}} h_e\left(\frac{y'}{\dot{y}}\right) \tau_o(x, y - y') dy' \quad , \quad (14)$$

which is the inverse Fourier transform of the effective system OTF, $\hat{\tau}(\nu, \omega)$.

It is important to note that any temporal effects which can be expressed in terms of a convolution can be analyzed in this manner. For example, thermal dynamics which may be present in the sensors can be included in the term $\hat{h}_e(\omega')$ and analyzed in the same way as electrical processing.

The most significant aspect of (13) is the fact that the effective OTF, $\hat{\tau}(\nu, \omega)$, is now a complex-valued function. Whereas the optical transfer function, $\hat{\tau}_o(\nu, \omega)$, is usually a real-valued function, the electrical transfer function, $\hat{h}_e(\omega')$, is rarely, if at all, real-valued. Thus, in general, $\hat{\tau}_e(\omega)$ and $\hat{\tau}(\nu, \omega)$ now have magnitude as well as phase characteristics due to a non-zero imaginary part.

The existence of non-zero and non-linear phase characteristics in the image-gathering system essentially produces a "blurring" effect which adds to the blurring due to the magnitude characteristics. Any known optical phase aberrations can also be included in $\hat{\tau}_o(\nu, \omega)$.

The transfer functions involved can be expressed in terms of their magnitude and phase in the form:

$$\hat{h}_e(\omega') = |\hat{h}_e(\omega')| e^{i\varphi_e(\omega')} \quad , \quad \hat{\tau}_o(\nu, \omega) = |\hat{\tau}_o(\nu, \omega)| e^{i\varphi_o(\nu, \omega)} \quad . \quad (15)$$

The effective system OTF can now be written as

$$\hat{\tau}(\nu, \omega) = |\hat{h}_e(j\omega')| |\hat{\tau}_o(\nu, \omega)| e^{i[\varphi_o(j\omega) + \varphi_o(\nu, \omega)]} \quad (16)$$

From (15), it is seen that, when the optical system has no phase aberrations, the effective system OTF phase is precisely the electronic phase, while the magnitude effects are multiplicative and depend on both optical and electrical system characteristics.

It should be noted that for causal, or non-anticipating, electrical filters, the impulse response is constrained by

$$h_e(t) = 0 \quad , \quad t < 0 \quad (17a)$$

so that the filter can be implemented in real time. This causality condition simply requires that the output at time t depend only on the input till time t so that the current output of the filter does not depend on the future input. From (10), this causality condition requires that the effective PSF of the electrical filter satisfy the condition

$$\tau_e(x, y) = 0 \quad , \quad y < 0 \quad . \quad (17b)$$

Figure 2 shows the effective image-gathering PSF, $\tau(x, y)$, while Figure 3 shows the corresponding OTF; i.e., the effective image-gathering system OTF including both optical and electrical filtering effects. The optical system PSF and OTF used in the analysis are shown in Figure 4. These correspond to a square with sides of 1° convolved with a Gaussian kernel to model the edge effects for the obstructed portion of the field-of-view. Figure 5 shows the magnitude and phase characteristics of a 2^{nd} order Butterworth filter which is the class of electrical filters used in this study to illustrate the phase distortion effects.

The main effects of electrical filtering on the image-gathering process are most clearly seen in the effective PSF of the image-gathering system shown in Figure 2. Comparison of

the optical system PSF (Figure 4) before the electrical filter and the effective PSF which includes the effects of both the optics and electronics, indicates that the effective PSF is shifted along the scan axis, y , is no longer symmetrical and displays a "tail". The basic square shape of the field of view is seen to have become more rectangular since the electrical filtering occurs along the scan axis which corresponds to the time axis. The response in the cross-scan x -axis is essentially unchanged. This results in a widening of the effective field of view along the scan direction.

The shift of the effective image-gathering PSF implies that the sensor output has a lag, or a distorted delay; i.e., the sensor output is obtained not only from the incoming radiation at the present time, but by appropriate weighting of past values of the incoming radiation. In spatial terms, this means that the sensor output, hence the image, is shifted relative to the scene in a distorted manner. This shift and the asymmetry of the PSF are due solely to the presence of phase effects; the blurring due to the magnitude characteristics is an additional effect. It should be noted that the shift associated with different frequencies is not uniform or constant; so that high frequency features and low frequency features are shifted by different amounts, producing the "distorted shift". Linear phase versus frequency characteristics would produce a constant shift for all frequencies which could easily be accounted for in post-processing. However, on-line or causal filters cannot produce linear phase characteristics, but may approximate linearity over a given frequency band.

The effect of different cutoff frequencies, ω_c , corresponding to the half-power, or 3 db, point can be seen by comparing Figures 2a, 2b and 2c. It is seen that the lower the cutoff frequency, the larger the shift and the more pronounced the tail. It is generally known that the highest cutoff frequency consistent with the goal of reducing aliasing and noise would usually produce the best results. The phase distortion effects shown in Figure 2 further suggest that the sensor aperture be designed with consideration to the electrical filter in order to achieve the desired effective image-gathering point-spread function.

The shift in the effective image-gathering PSF shows that the edges of the image data

will be shifted relative to scene edges along the scan direction. This is a further indication of the necessity for the combined image-gathering and image-processing approach presented in [14]. An edge detector which does not make use of the effective image-gathering PSF will at best locate the scene edge with an error equal to the shift introduced during image-gathering. Whereas an edge detector which makes use of the effective image-gathering PSF can reduce the errors in edge location by appropriate processing as will be discussed in the following sections.

3. OPTIMAL IMAGE PROCESSOR

From the previous section, it is clear that depending on the accuracy required (desired) and the frequency content of the signal, the effects of electrical processing are not necessarily negligible. The sensor design must trade off noise and aliasing versus phase distortion. Also, the processing performed on the image data obtained by the sensor should try to reduce these effects according to the frequency content of the feature to be extracted from the image data.

A useful criterion for evaluating the level of accuracy in estimating a feature is the spatially averaged mean-squared error. This criterion can be expressed in the form

$$J = \lim_{|A| \rightarrow \infty} \frac{1}{|A|} \iint_A E |c(x, y) - r(x, y)|^2 dx dy \quad (19)$$

where E denotes the statistical expectation operator, $|A|$ the area of the surface A , $c(x, y)$ the characteristic or feature of the scene to be estimated and $r(x, y)$ the estimate of the desired feature.

The system shown in Figure 1 can be described by the equations

$$s(x, y) = \int_{-\infty}^{\infty} \int_{-\infty}^{\infty} \tau(x', y') L(x - x', y - y') dx' dy' \quad , \quad (20)$$

$$m_{jk} = s(x_j, y_k) + n_{jk} \quad , \quad -\infty < j, k < \infty \quad , \quad (21)$$

where the effective system PSF, $\tau(x, y)$, satisfies (14) - (16).

We restrict the system output, $r(x, y)$, to be of the form

$$r(x, y) = \sum_{j, k=-\infty}^{\infty} \tau_p(x - x_j, y - y_k) m_{jk} \quad , \quad x, y \in R \quad (22)$$

The system output, $r(x, y)$, which must estimate the desired characteristic of the scene is a weighted infinite sum of the sampled, noisy measurement, m_{jk} . The particular image processor is determined by the choice of the weighting function, $\tau_p(x, y)$.

The class of scene characteristics or features that will be considered here is the class that can be obtained from the scene radiance, $L(x, y)$, using a linear, spatially invariant operator. Thus,

$$c(x, y) = \int_{-\infty}^{\infty} \int_{-\infty}^{\infty} \tau_c(x', y') L(x - x', y - y') dx' dy' \quad , \quad (23)$$

where $\tau_c(x, y)$ is the PSF corresponding to the linear operator. Note that the Wiener spectrum, $\hat{\phi}_c(\nu, \omega)$, of the desired scene characteristic is given by

$$\hat{\phi}_c(\nu, \omega) = |\hat{\tau}_c(\nu, \omega)|^2 \hat{\phi}_L(\nu, \omega) \quad , \quad (24)$$

where $\hat{\phi}_L(\nu, \omega)$ is the Wiener spectrum or power spectral density (PSD) of the scene radiance, considered to be a second-order stationary random process. The noise n_{jk} will be assumed to be a second-order stationary random sequence, statistically independent of the scene, $L(x, y)$.

In [14], it is shown that the image processor, $\hat{\tau}_p(\nu, \omega)$, which minimizes the spatially averaged mean-squared error, J in (19), under the constraints (20) - (23) is unique and given by

$$\hat{\tau}_p(\nu, \omega) = \frac{\hat{\tau}_c(\nu, \omega) \hat{\tau}^*(\nu, \omega) \hat{\phi}_L(\nu, \omega)}{\hat{\phi}_m(\nu, \omega)} \quad , \quad \nu, \omega \in R \quad (25)$$

where the superscript "*" denotes the complex conjugate and $\hat{\phi}_m(\nu, \omega)$ is given by [12]

$$\hat{\phi}_m(\nu, \omega) = \hat{\phi}_s(\omega) + \hat{\phi}_a(\nu, \omega) + \hat{\phi}_n(\nu, \omega) \quad , \quad (26)$$

$$\hat{\phi}_s(\nu, \omega) = |\hat{\tau}(\nu, \omega)|^2 \hat{\phi}_L(\nu, \omega) \quad , \quad (27a)$$

$$\hat{\phi}_a(\nu, \omega) = \sum_{(j,k) \neq (0,0)}^{\infty} \hat{\phi}_s(\nu - j\nu_o, \omega - k\omega_o) \quad , \quad (27b)$$

ν_o and ω_o are the Nyquist frequencies along the ν and ω axes, respectively, $\hat{\phi}_a(\nu, \omega)$ is the PSD of the aliasing error, $\hat{\phi}_n(\nu, \omega)$ is the discrete PSD of the noise sequence $\{n_{jk}, -\infty < j, k < \infty\}$.

The effects of non-zero phase in the effective image-gathering OTF are due to the complex conjugate term in (25). The magnitude characteristics of the optimal image processor remain essentially unchanged. In particular, note that

$$|\hat{r}_p(\nu, \omega)| = \frac{|\hat{r}_c(\nu, \omega)| |\hat{r}^*(\nu, \omega)| \hat{\phi}_L(\nu, \omega)}{\hat{\phi}_m(\nu, \omega)} \quad , \quad \nu, \omega \in R \quad (28a)$$

$$\begin{aligned} \varphi_p(\nu, \omega) &= \varphi_c(\nu, \omega) - \varphi(\nu, \omega) \\ &= \varphi_c(\nu, \omega) - \varphi_c(j\omega) - \varphi_o(\nu, \omega), \quad \nu, \omega \in R \end{aligned} \quad (28b)$$

where $\varphi_p(\nu, \omega)$, $\varphi_c(\nu, \omega)$ and $\varphi(\nu, \omega)$ represent the phase functions of $\hat{r}_p(\nu, \omega)$, $\hat{r}_c(\nu, \omega)$ and $\hat{r}(\nu, \omega)$, respectively.

Figure 6 shows the magnitude of the OTF of the optimal image processor for edge detection. The image-gathering system used is the smoothed square aperture followed by 2nd order low-pass Butterworth filters at various cutoff frequencies, ω_c , discussed in the preceding section. The sampling strategy used is a square lattice with sampling interval normalized to unity in both the x- and y-axes. The feature or characteristic estimated is $-\nabla^2 * L$; i.e., the negative Laplacian of the incoming radiance, which is assumed to be a sample function from a second-order stationary random process with PSD

$$\hat{\phi}_L(\nu, \omega) = \frac{2\pi\mu_r^2\sigma_L^2}{[1 + 2\pi\mu_r(\nu^2 + \omega^2)]^{3/2}} \quad . \quad (29)$$

It is seen that this class of radiance inputs has circular symmetry. The parameter μ_r corresponds to the average distance between two edges, and represents a measure of the level of detail present in the scene.

As can be seen from Figure 6, the optimal edge detector transfer function, $\hat{r}_p(\nu, \omega)$, vanishes at zero frequency, peaks near but before the Nyquist frequency at 0.5, and attenuates high frequencies. The major characteristics of the optimal edge detector magnitude are essentially the same as shown in [14] where the image gathering OTF, $\hat{r}(\nu, \omega)$, is assumed to have zero phase. The only essential difference in the case considered in this paper, is that the optimal edge detector has non-zero phase. Thus, in this case, the optimal characteristic image processor tries to eliminate the phase shift introduced by the image gathering optics and electronics, as well as trying to reduce the magnitude induced blurring.

From the perspective plots in Figure 6, it is clear that the optimal edge detector for this case is not circularly symmetric, but is mainly influenced by the sampling lattice. Thus, the optimal edge detector attempts to reduce all three of the major effects introduced during image acquisition: blurring, noise and sampling. In this case, blurring has two components: magnitude induced and phase induced. The optimal edge detector attempts to minimize both types of blurring.

The similarity of the magnitude characteristics for the non-zero phase case seen here and the zero phase case discussed in [14] is quite striking. Nevertheless, the effect of the Butterworth filter magnitude characteristics can be seen by comparing the different cutoff frequency plots. The effect is seen most clearly at the low cutoff frequency of 0.3, where the peaks along the scan axis (ω) are lower than those along the cross-scan (ν) axis. This demonstrates that while the sampling lattice effects are the most pronounced ones, the optimal image processor is also influenced by non-symmetric effects in the effective image-gathering system. Figure 7 shows the optimal PSF for estimating $-\nabla^2 L(x, y)$ from the sampled image. The effect of the non-zero phase of the optimal edge detector is clearly

seen in these plots. Note that the optimal PSF is shifted in the negative scan- or y-axis; i.e., the shift in the optimal PSF is in the opposite direction from the shift in the effective image-gathering PSF (see Figure 2). It is clear that the optimal image processor is correcting the distorted shift present in the image. Further note that the optimal image processor PSF displays a rectangular character more clearly noticeable at low cutoff frequencies, where the effective image-gathering PSF has a rectangular character.

The main strategy of the optimal image processor is seen to be one of subtracting surrounding samples from the center sample with appropriate weighting, which is an approximation to the Laplacian operator. The rectangular character and the distorted shift combine to account for the rectangular character of the image-gathering PSF. However, the main characteristics of the optimal image processor are quite similar to the one shown in [14] (Figure 14) where the image-gathering system has zero phase distortion.

4. OPTIMIZATION OF THE IMAGE-GATHERING SYSTEM

In the preceding section, it has been shown that the optimal image processor for estimating a scene characteristic accounts for any known phase shifts introduced by the image gathering system. Thus, when an electrical filter having non-zero phase is used, the image processor itself has non-zero phase, as evidenced by (28), in an attempt to eliminate this phase distortion. Therefore, the optimal image processor depends on the phase characteristics of the effective image-gathering OTF.

The spatially averaged mean-squared error, J , defined by (19) is known to be [14]

$$J = \int_{-\infty}^{\infty} \int_{-\infty}^{\infty} \frac{|\hat{r}_c(\nu, \omega)|^2 \hat{\phi}_L(\nu, \omega)}{1 + \frac{|\hat{r}(\nu, \omega)|^2 \hat{\phi}_L(\nu, \omega)}{\hat{\phi}_a(\nu, \omega) + \hat{\phi}_n(\nu, \omega)}} d\nu d\omega \quad (30)$$

when the optimal characteristic image processor in (25), or equivalently the expression in (28), is used.

From this expression and the expression for the aliasing error spectrum, $\hat{\phi}_a(\nu, \omega)$, in (27), it is clear that the spatially averaged mean-squared error, J , depends only on the magnitude characteristics of the image-gathering OTF, $\hat{r}(\nu, \omega)$. Alternately, the error is independent of the phase characteristics of the image-gathering system when the optimal image processor for the desired feature is used. It is important to note that when the optimal image processor is not used, the phase characteristics of the image-gathering system may influence the error according to the particular suboptimal image processor used.

The optimal characteristic image processor $\hat{r}_p(\nu, \omega)$ depends on the scene's statistical characteristics as described by $\hat{\phi}_L(\nu, \omega)$ and the effective discrete noise PSD, $\hat{\phi}_n(\nu, \omega)$. In most cases, the true statistics of the scene and noise are not accurately known, so that the optimal image processor is based on uncertain parameters in $\hat{\phi}_L(\nu, \omega)$ and $\hat{\phi}_n(\nu, \omega)$. Therefore, the robustness, or lack of sensitivity, of the optimal image processor to errors in

parameters such as level of scene detail, μ_r , and signal-to-noise ratio, S/N, is an integral part of the design process.

It is of interest to see whether the robustness of the optimal characteristic image processor is affected by the phase characteristics of the image gathering system. To analyze the sensitivity, let $\hat{\tau}'_p(\nu, \omega)$ be an arbitrary image processor; then the mean-squared error can be shown to be [14]

$$J' = \int_{-\infty}^{\infty} \int_{-\infty}^{\infty} \left[|\hat{\tau}_c(\nu, \omega)|^2 \hat{\phi}_L(\nu, \omega) - 2R_e(\hat{\tau}_c^*(\nu, \omega) \hat{\tau}(\nu, \omega) \hat{\tau}'_p(\nu, \omega)) \hat{\phi}_L(\nu, \omega) + |\hat{\tau}'_p(\nu, \omega)|^2 \hat{\phi}_m(\nu, \omega) \right] d\nu d\omega \quad (31)$$

Let $\hat{\phi}'_L(\nu, \omega)$ and $\hat{\phi}'_n(\nu, \omega)$ be the PSD's used in designing $\hat{\tau}'_p(\nu, \omega)$, and let

$$\hat{\tau}'_p(\nu, \omega) = \hat{\tau}_c(\nu, \omega) \hat{\tau}^*(\nu, \omega) \frac{\hat{\phi}'_L(\nu, \omega)}{\hat{\phi}'_m(\nu, \omega)}, \quad \nu, \omega \in R, \quad (32)$$

where $\hat{\phi}'_m(\nu, \omega)$ is given by

$$\hat{\phi}'_m(\nu, \omega) = \sum_{j,k=-\infty}^{\infty} |\hat{\tau}(\nu - j\nu_o, \omega - k\omega_o)|^2 \hat{\phi}'_L(\nu - j\nu_o, \omega - k\omega_o) + \hat{\phi}'_n(\nu, \omega) \quad (33)$$

Substituting (32) into (31), and manipulating,

$$J' = \int_{-\infty}^{\infty} \int_{-\infty}^{\infty} \left[|\hat{\tau}_c(\nu, \omega)|^2 \hat{\phi}_L(\nu, \omega) - |\hat{\tau}_c(\nu, \omega)|^2 |\hat{\tau}(\nu, \omega)|^2 \frac{\hat{\phi}'_L(\nu, \omega)}{\hat{\phi}'_m(\nu, \omega)} \left(\frac{\hat{\phi}_m(\nu, \omega)}{\hat{\phi}'_m(\nu, \omega)} \hat{\phi}'_L(\nu, \omega) - 2\hat{\phi}_L(\nu, \omega) \right) \right] d\nu d\omega \quad (34)$$

Observation of (34), (33), (26) and (27) reveals that J' depends only on the magnitude of the image gathering system, and is independent of its phase characteristics. Further note that since J uses the optimal image processor while J' does not, it follows that

$$\Delta J = J' - J \geq 0 \quad (35)$$

Thus, the change in the mean-squared error due to using $\hat{\phi}'_L(\nu, \omega)$ and $\hat{\phi}'_m(\nu, \omega)$ in designing the image processor, when the true quantities are $\hat{\phi}_L(\nu, \omega)$ and $\hat{\phi}_m(\nu, \omega)$, is given by ΔJ in (35) which, of necessity, is non-negative. From the previous argument, it is clear that J , J' , hence ΔJ are independent of the phase characteristics of the image gathering system. This result might have been expected since the suboptimal image processor considered uses the correct phase characteristics for the image-gathering system PSF and uses the optimal processor expression in (25), albeit with incorrect statistics for the radiance signal and noise. In fact, observation of the general error expression in (31) indicates that if the phase of the suboptimal image processor is exactly the negative of the effective image-gathering OTF, then ΔJ will be independent of the phase function.

It is seen that both the spatially averaged mean-squared error, and the robustness properties of the optimal image-gathering system depend only on the magnitude of the image gathering system.

5. CONCLUSIONS

This paper extends the results of [14] on the combined optimization of the image-gathering and image-processing systems to the case where the image-gathering system produces phase distortion in the acquired image due to electrical filtering.

The effects of electrical filtering or, more generally, temporal processing such as thermal dynamics, is transformed into an equivalent spatial filter operating on spatial inputs. When combined with the optical transfer function, the overall effect of image-gathering optics and electronics can be described by a complex transfer function containing both magnitude and (non-zero) phase characteristics. Thus, the acquired image contains both magnitude and phase distortion before being sampled according to the sampling lattice and being contaminated by noise.

The effective point spread function of the electro-optical image-gathering system is characterized by a shift in the PSF maximum away from the origin in the scan direction and by a "tail" asymptotically decaying to zero in the scan direction, as shown in Figure 2. As evidenced by this effective PSF, the effect of electrical filtering significantly modifies the image-gathering characteristics. Sharp edges in the observed scene are not only blurred, but also shifted in position along the scan direction. The amount of magnitude and phase distortion in the acquired image depends on the (spatial) frequency content of the incoming radiance.

The optimal image processor which minimizes the spatially averaged mean-squared error for any linear scene feature is shown to eliminate the phase shift introduced during image acquisition. The optimal image processor itself has non-zero phase for this purpose, its phase equaling the negative of the image-gathering system phase. The optimal image processor for edge detection is not circularly symmetric, but is highly dependent

on the sampling lattice, and attempts to minimize the blurring, aliasing and noise errors introduced during image acquisition.

It is also shown that, when the optimal image processor for the desired characteristic is used, the spatially averaged mean-squared error is independent of the phase characteristics of the image-gathering system and depends solely on the magnitude of the image-gathering transfer function. Similarly, the robustness characteristics are also shown to be independent of the phase characteristics of the image-gathering system; i.e., the change in the spatially averaged mean-squared error due to errors in the scene level of detail or noise statistics is solely dependent on the magnitude of the image-gathering transfer function, when the optimal image processor is used.

These results imply that when the optimal image processor is to be used, the basic trends obtained in [14] are valid for non-zero phase image acquisition. Thus, in the design of the image-gathering system, the results indicate that if the image-gathering system is designed for 1) lower signal-to-noise ratio as well as 2) higher scene detail than generally expected, and 3) with a 3 dB cutoff near, but lower than, the Nyquist frequency, it is possible to achieve nearly optimal mean-squared error. This is possible even if the actual signal-to-noise ratio turns out to be higher or the scene actually observed has a lower level of detail than used in the design, as long as the optimal image processor is used to eliminate the phase distortion introduced in image acquisition.

If the optimal image processor cannot be used due to computational restrictions or other constraints, the image processor output may have errors depending on both magnitude and phase characteristics. In such cases, the errors can be analyzed using the effective image-gathering PSF developed in Section 2 and the general expression for the spatially averaged mean-squared error given in (31).

REFERENCES

1. Mertz, P. and F. Grey, Bell Syst. Tech. J., Vol. 13, pp. 464, 1934.
2. Baldwin, M. W., Jr., Bell Syst. Tech. J., Vol. 19, pp. 563, 1940.
3. Kell, R. D., et al., RCS Ref., Vol. 5, pp. 8, 1940.
4. Schade, O. H., Sr., J. Soc. Motion Pict. Telev. Eng., Vol. 56, pp. 131, 1951; Vol. 58, pp. 181, 1952; Vol. 61, pp. 97, 1953; Vol. 64, pp. 593, 1955; Vol. 73, pp. 81, 1964.
5. Robinson, A. H., Appl. Opt., Vol. 12, pp. 1054, 1973.
6. Pearson, D. E., Transmission and Display of Pictorial Information, Wiley and Sons, New York, New York, 1975.
7. Gonsalves, R. A. and P. S. Considine, Opt. Eng., Vol. 15, pp. 64, 1976.
8. Pratt, W. K., Digital Image Processing, Wiley and Sons, New York, New York, 1978.
9. Huck, F. O., N. Halyo and S. K. Park, Appl. Opt., Vol. 19, pp. 2174, 1980.
10. Huck, F. O., N. Halyo and S. K. Park, "Information Efficiency of Line-Scan Imaging Mechanisms," Appl. Opt., Vol. 20, pp. 1990-2007, 1981.
11. Huck, F. O., S. K. Park, N. Halyo and S. T. Stallman, "Aliased Noise in Radiometric Measurements," NASA Tech. Paper 1639, U. S. Government Printing Office, Washington, DC, 1980.
12. Halyo, N. and S. T. Stallman, "A Parametric Study of Aliasing Error for a Narrow Field of View Scanning Radiometer," NASA Contract Rep. 3294, U. S. Government Printing Office, Washington, DC, 1980.
13. Huck, F. O., C. L. Fales, N. Halyo, R. W. Samms, and K. Stacey, "Image Gathering and Processing: Information and Fidelity," J. Opt. Soc. Am. A, Vol. 2, pp. 1644-1666, 1985.

14. Halyo, N. and R. W. Samms, "Combined Optimization of Image-Gathering Optics and Image-Processing Algorithm for Edge Detection," J. Opt. Soc. Am. A, Vol. 3, No. 9, pp. 1522-1536, 1986.

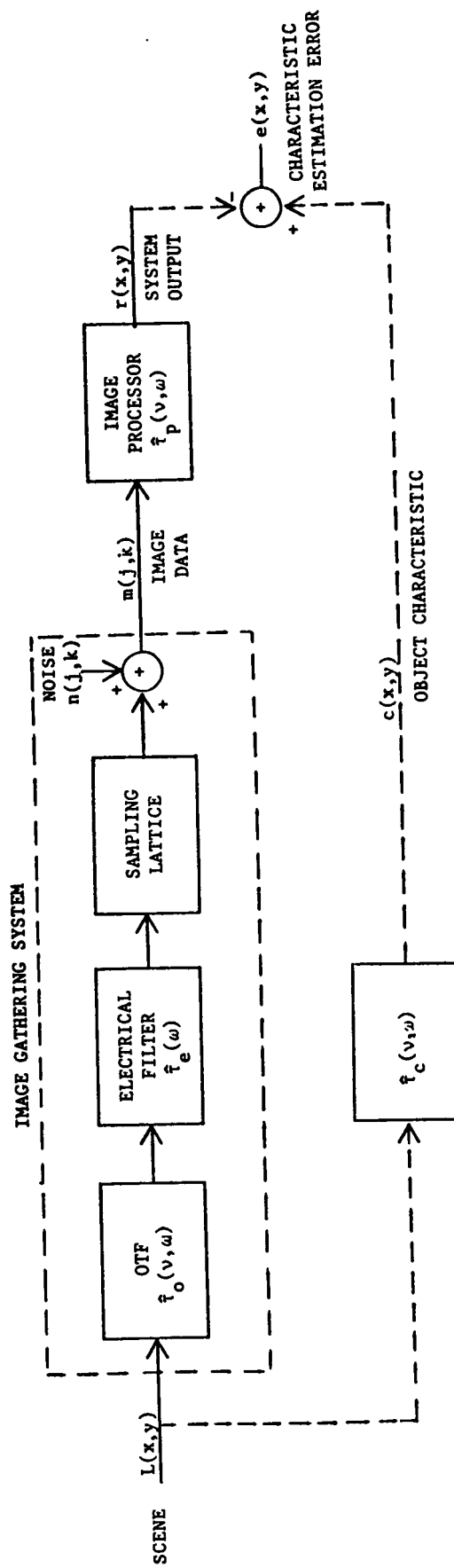
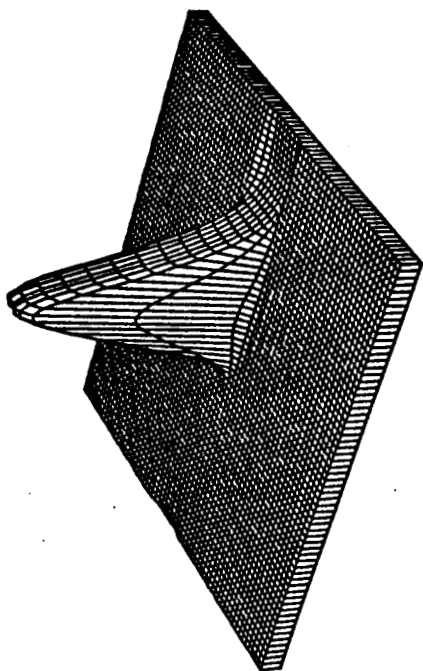
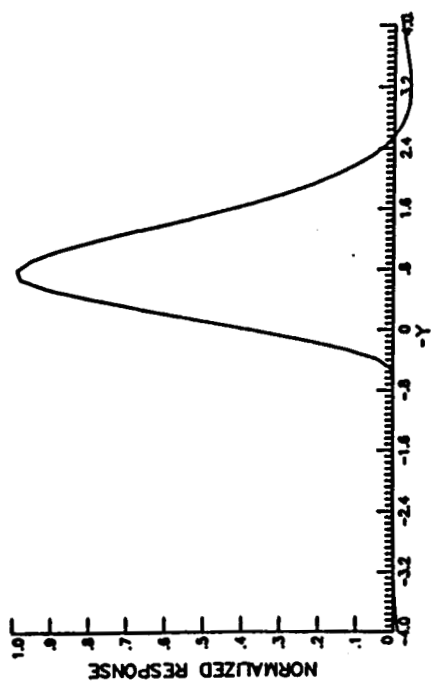


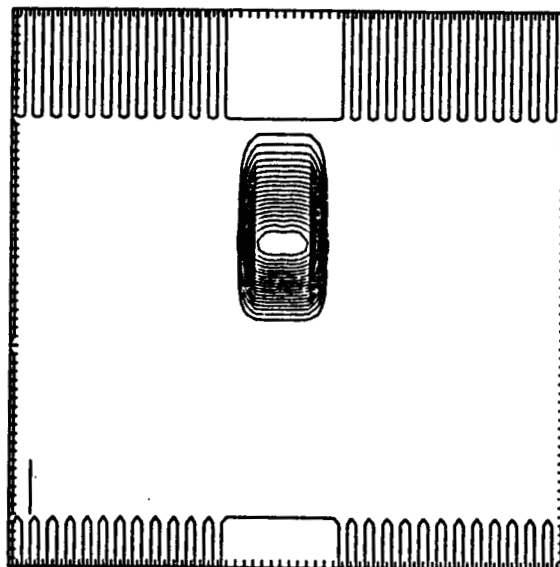
FIGURE 1. BASIC SCANNER BLOCK DIAGRAM



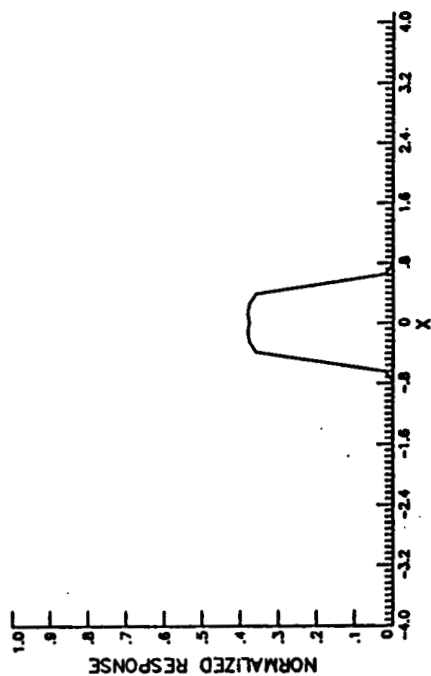
Perspective Plot



Cross-section at $x = 0$



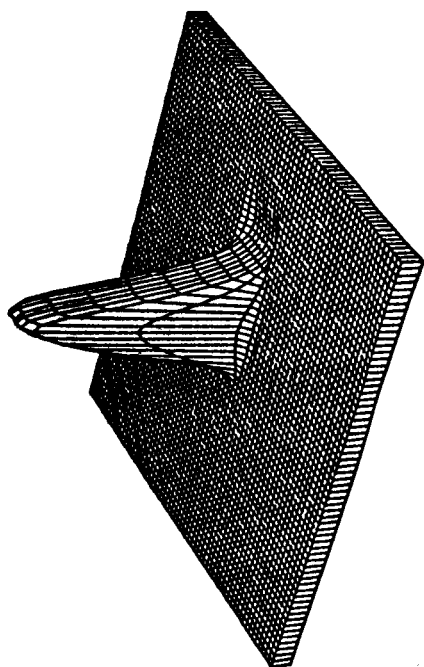
Contour Plot



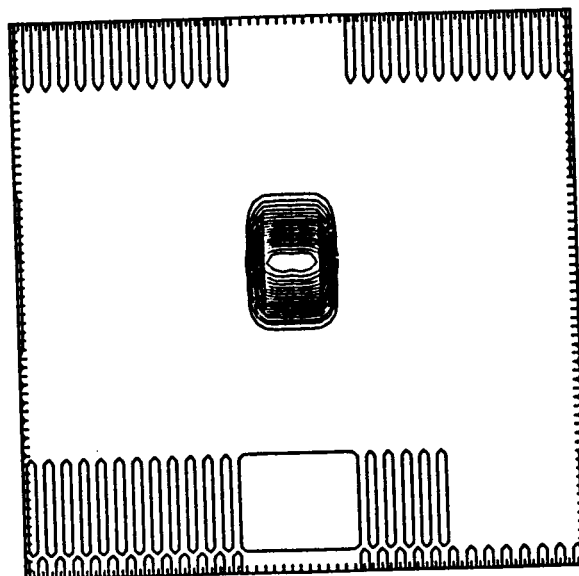
Cross-section at $y = 0$

a) $\omega_c = .3$

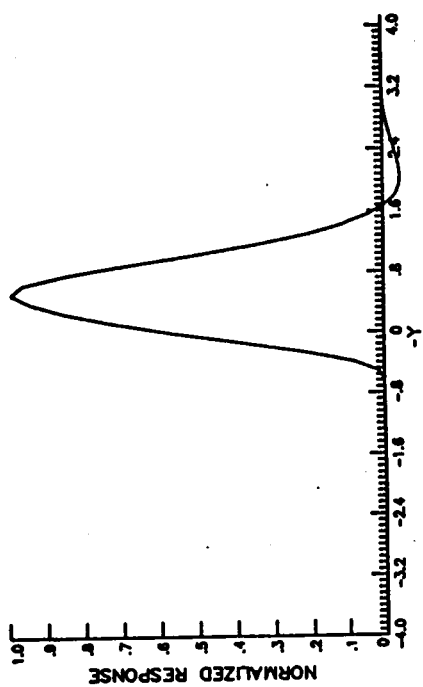
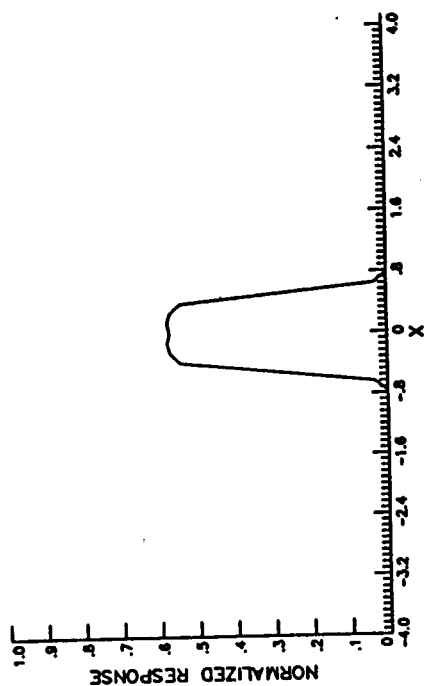
FIGURE 2. EFFECTIVE IMAGE-GATHERING PSF, $\tau(x,y)$



Perspective Plot

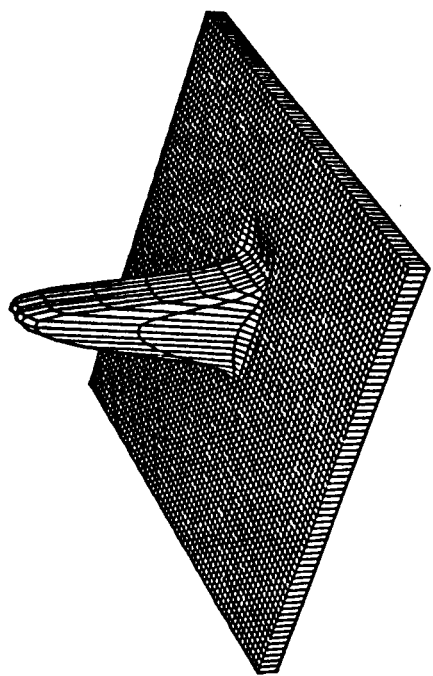


Contour Plot

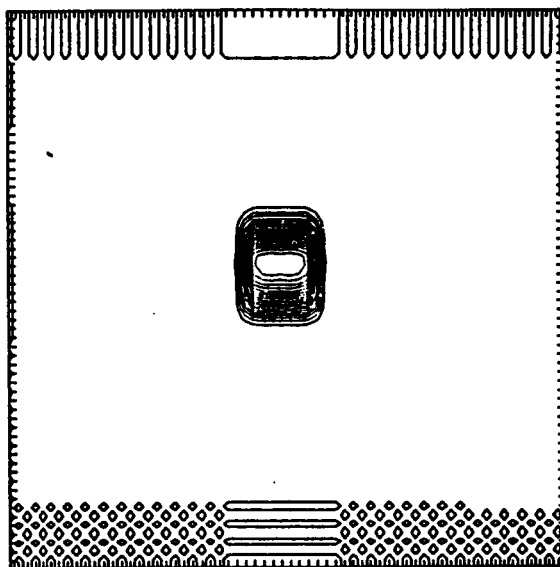
Cross-section at $x = 0$ Cross-section at $y = 0$

b) $\omega_c = .5$

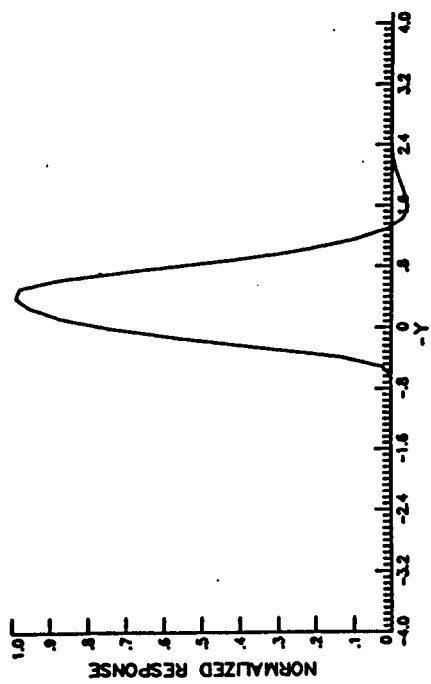
FIGURE 2. EFFECTIVE IMAGE-GATHERING PSF, $\tau(x,y)$



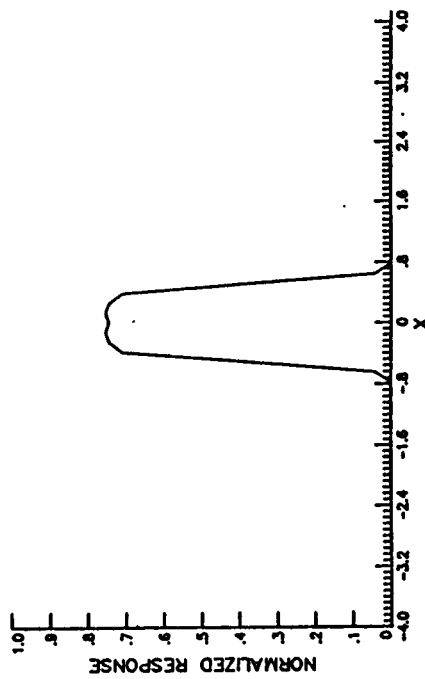
Perspective Plot



Contour Plot



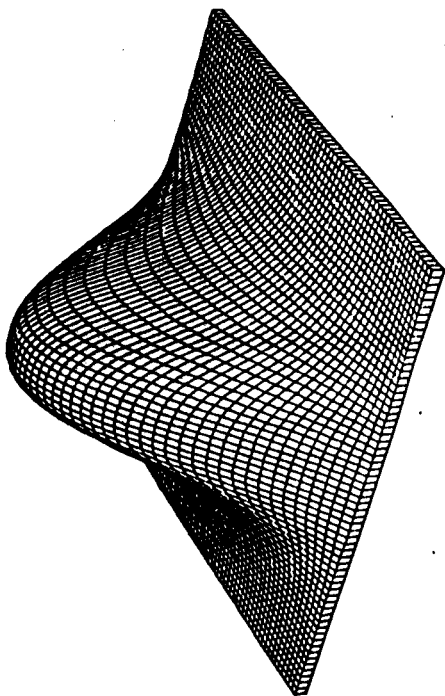
Cross-section at $x = 0$



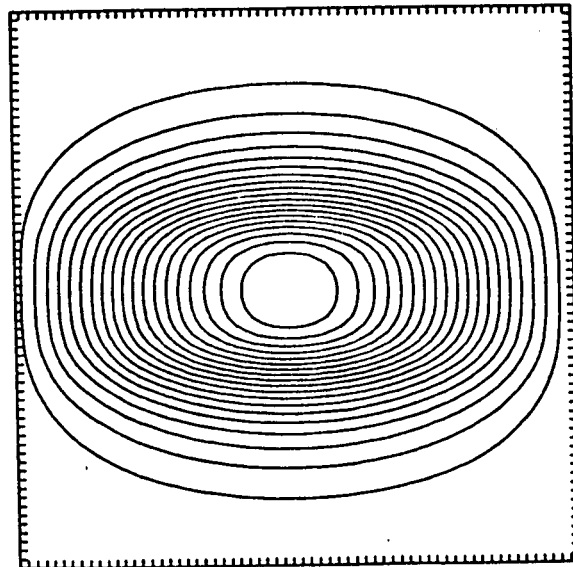
Cross-section at $y = 0$

$$c) \omega_c = .7$$

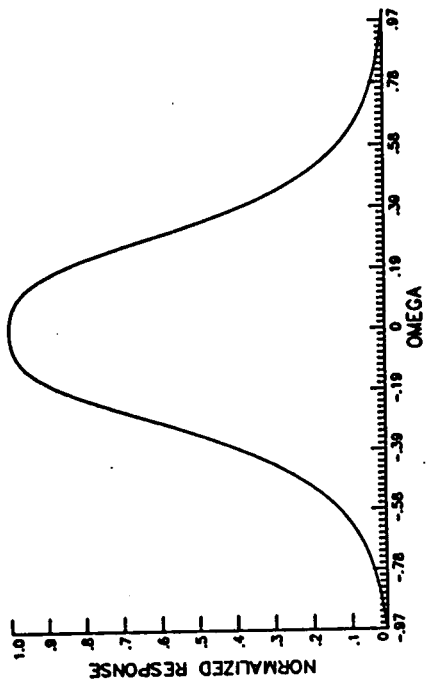
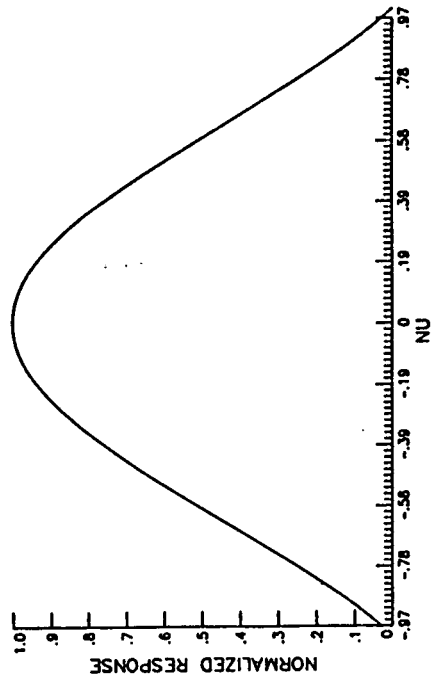
FIGURE 2. EFFECTIVE IMAGE-GATHERING PSF, $\tau(x,y)$



Perspective Plot

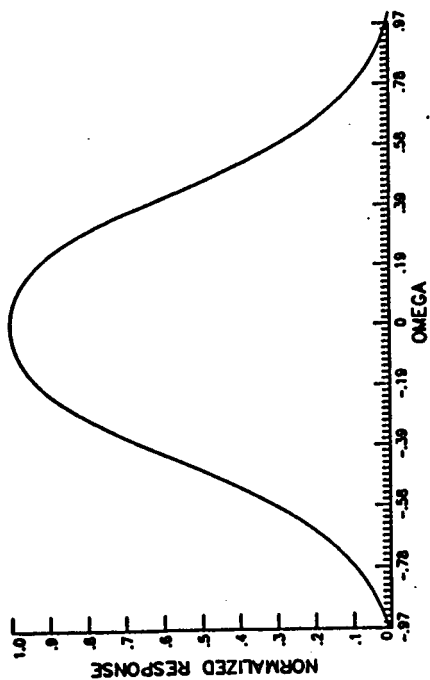


Contour Plot

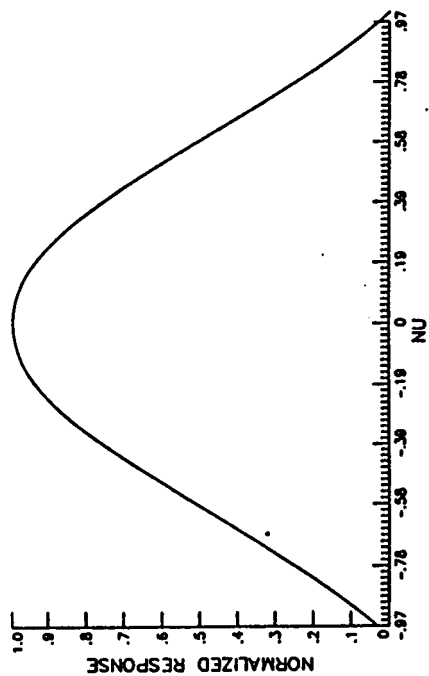
Cross-section at $\nu = 0$ Cross-section at $\omega = 0$

a) $\omega_c = .3$

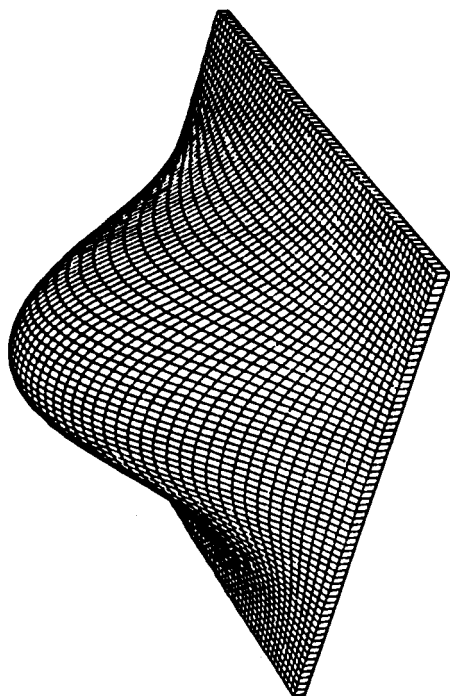
FIGURE 3. EFFECTIVE IMAGE-GATHERING OTF, $\hat{\tau}(\nu, \omega)$



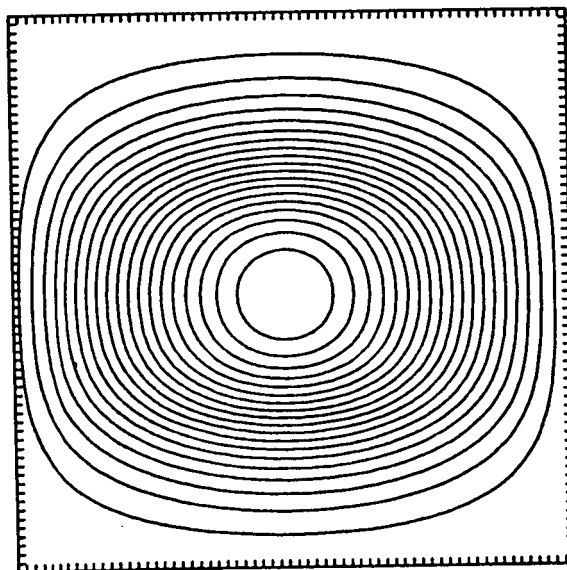
Cross-section at $\nu = 0$



Cross-section at $\omega = 0$



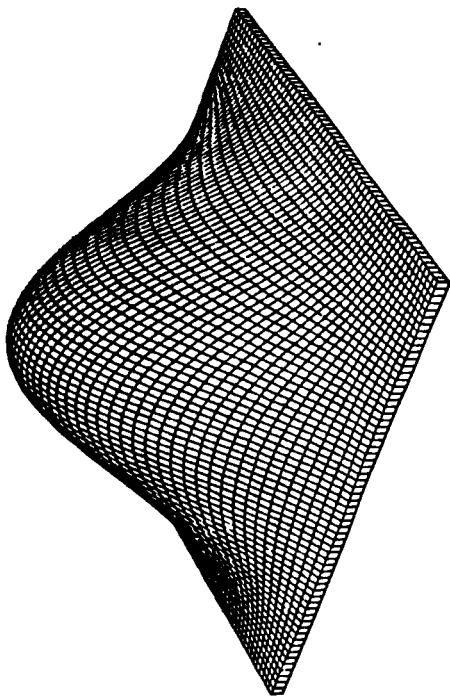
Perspective Plot



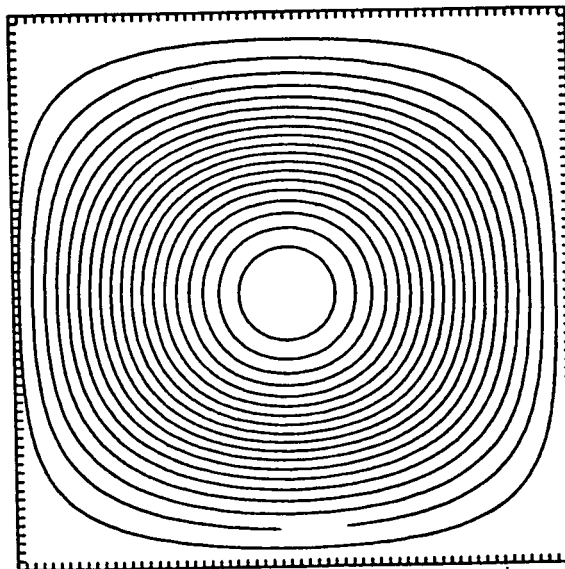
Contour Plot

b) $\omega_c = .5$

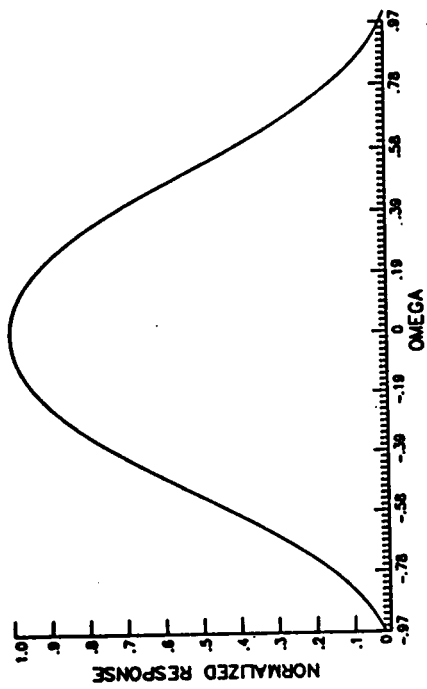
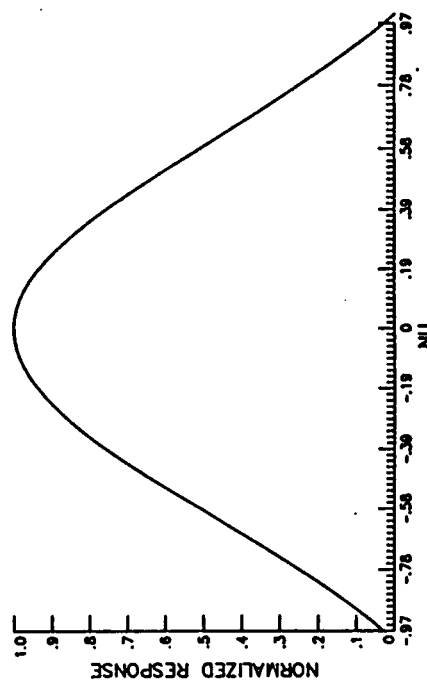
FIGURE 3. EFFECTIVE IMAGE-GATHERING OTF, $\hat{\tau}(\nu, \omega)$

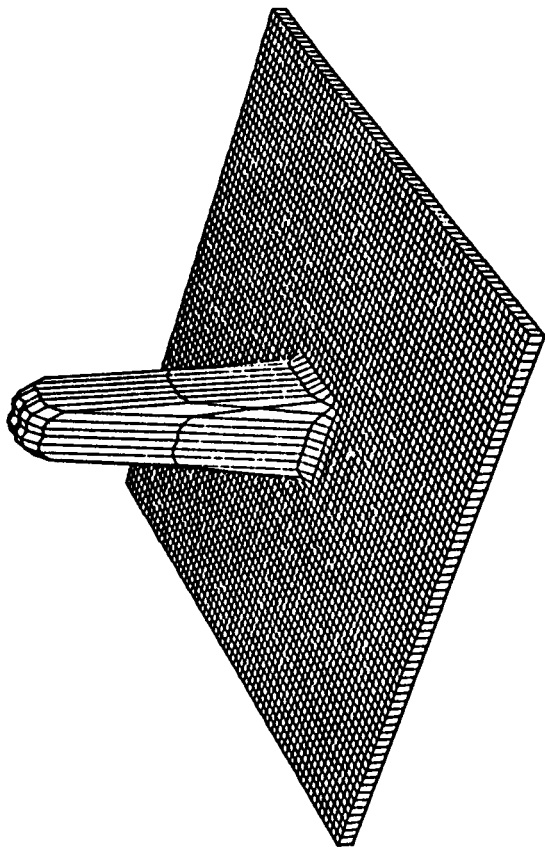


Perspective Plot

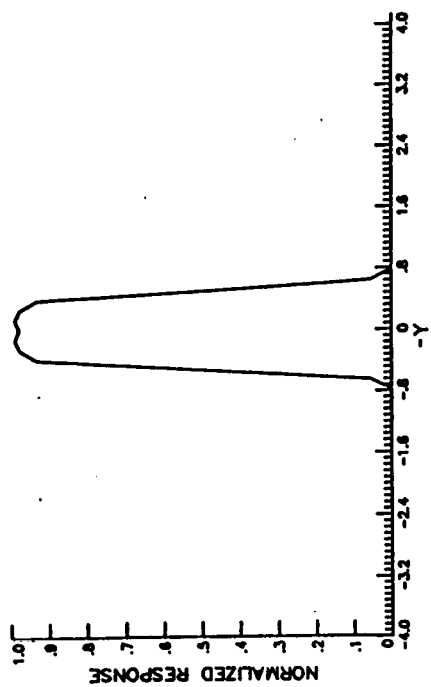


Contour Plot

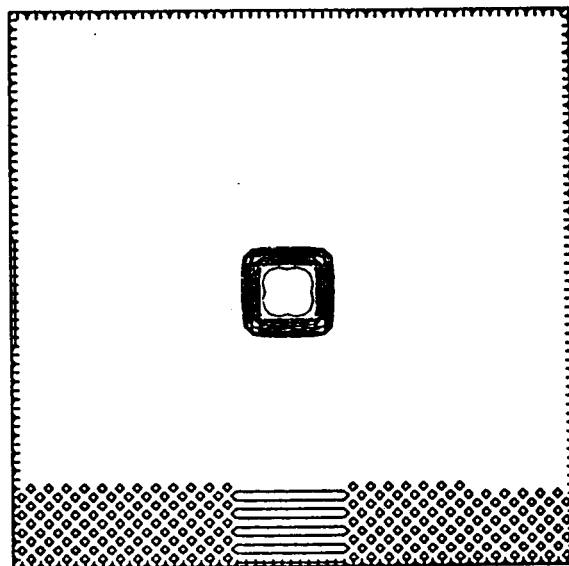
Cross-section at $\nu = 0$ Cross-section at $\omega = 0$ c) $\omega_c = .7$ FIGURE 3. EFFECTIVE IMAGE-GATHERING OTF, $\hat{\tau}(\nu, \omega)$



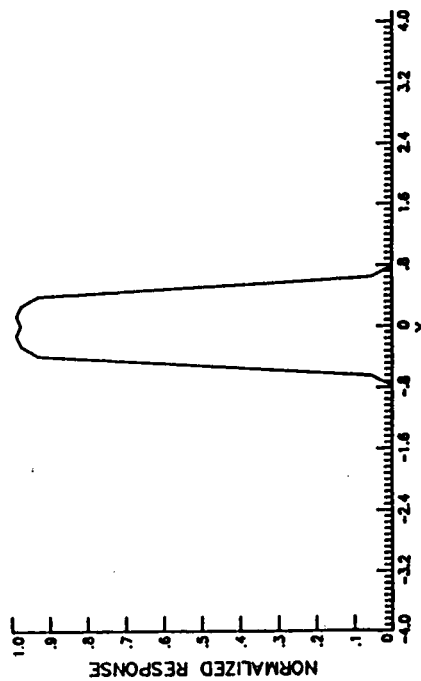
Perspective Plot



Cross-section at $x = 0$



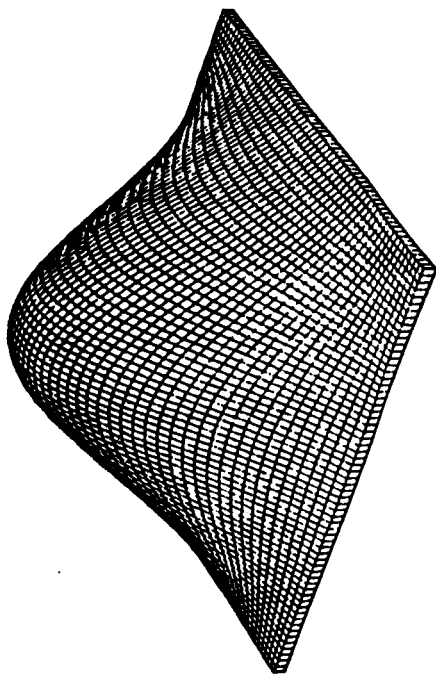
Contour Plot



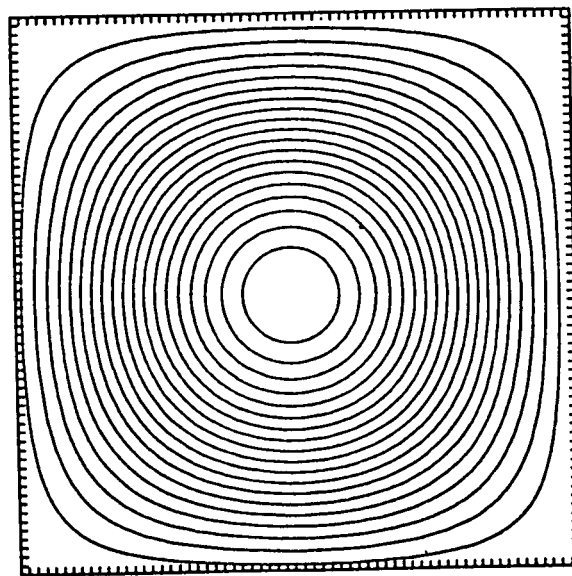
Cross-section at $y = 0$

a) Point-spread function

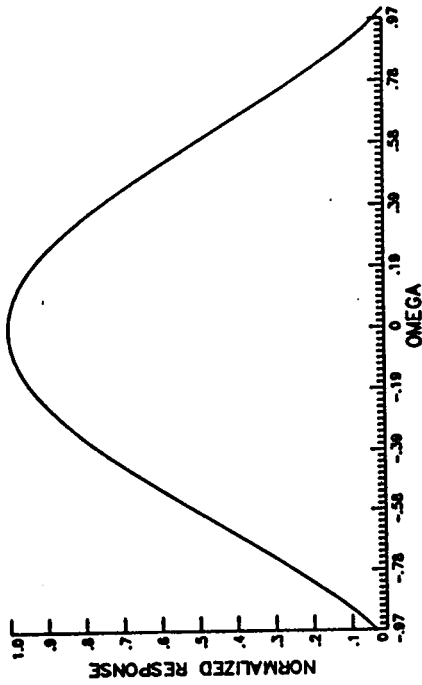
FIGURE 4. IMAGE-GATHERING OPTICS



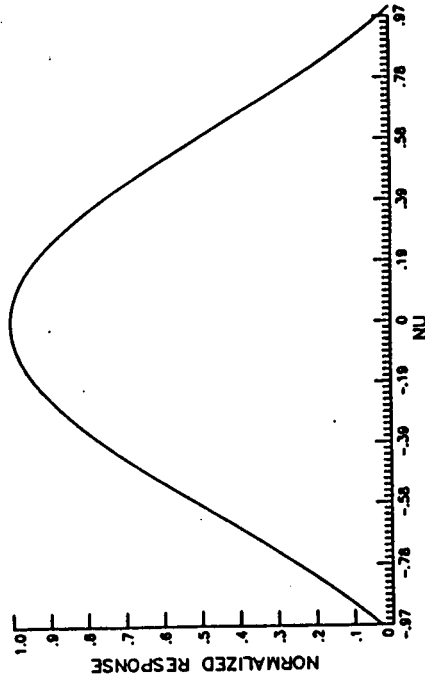
Perspective Plot



Contour Plot



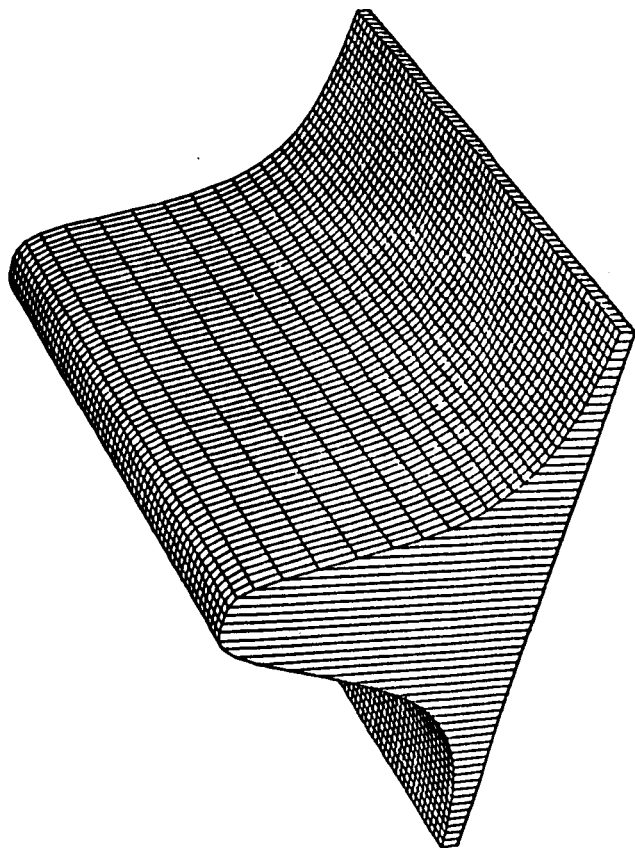
Cross-section at $\nu = 0$



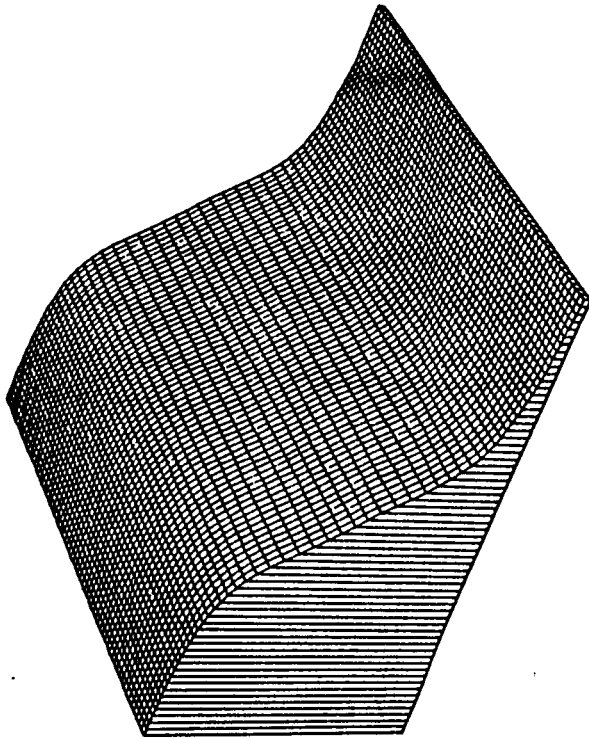
Cross-section at $\omega = 0$

b) Optical transfer function

FIGURE 4. IMAGE-GATHERING OPTICS

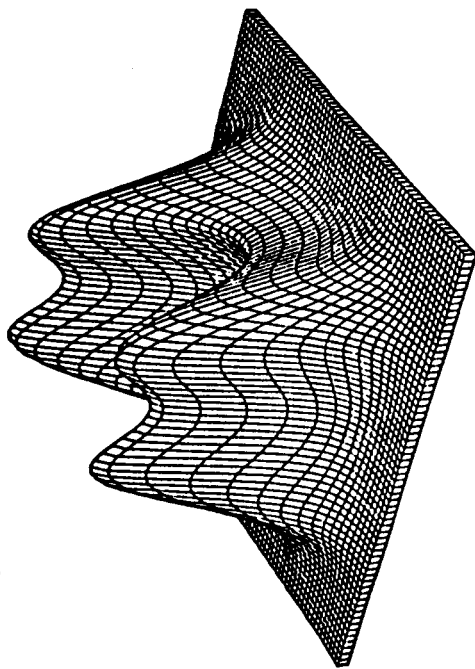


a) Magnitude

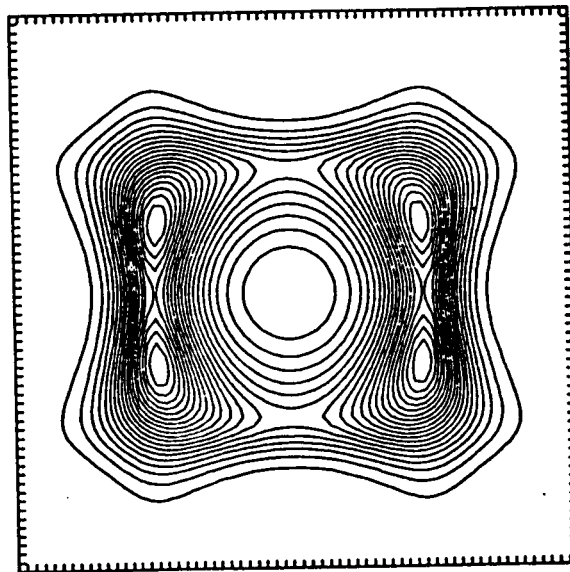


b) Phase

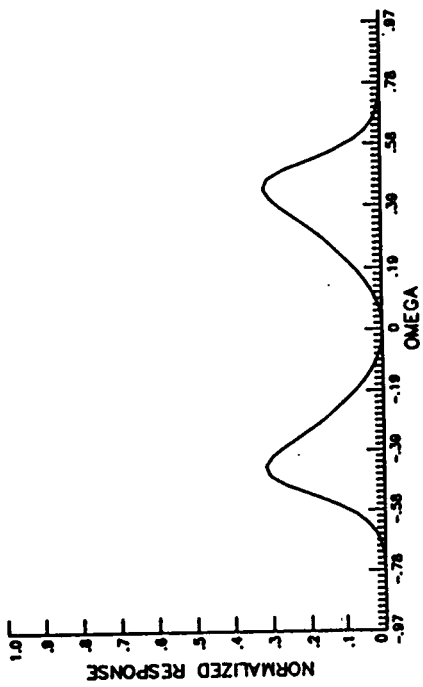
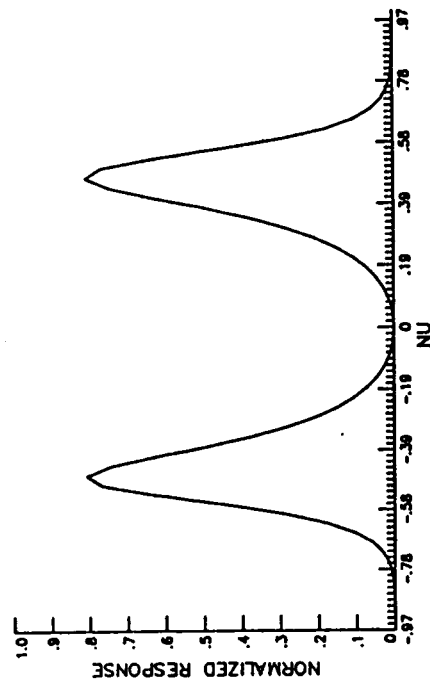
FIGURE 5. LOW-PASS ELECTRICAL FILTER (2nd ORDER BUTTERWORTH)

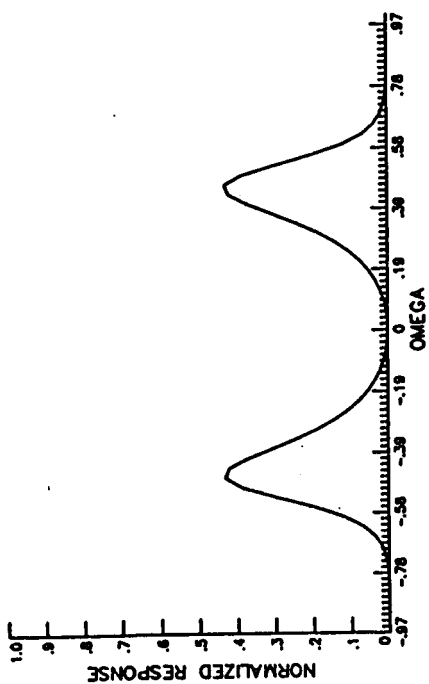


Perspective Plot

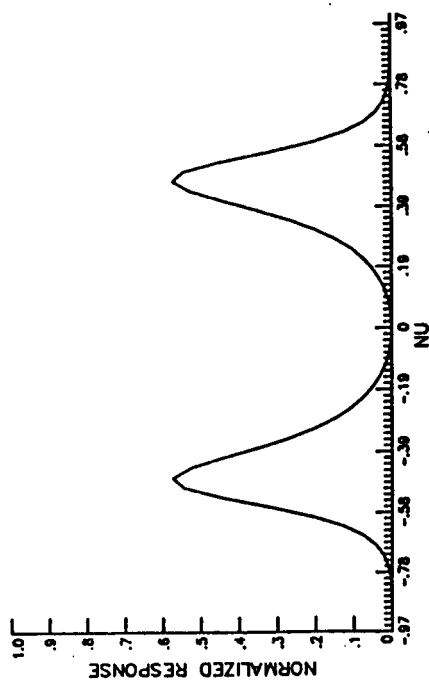


Contour Plot

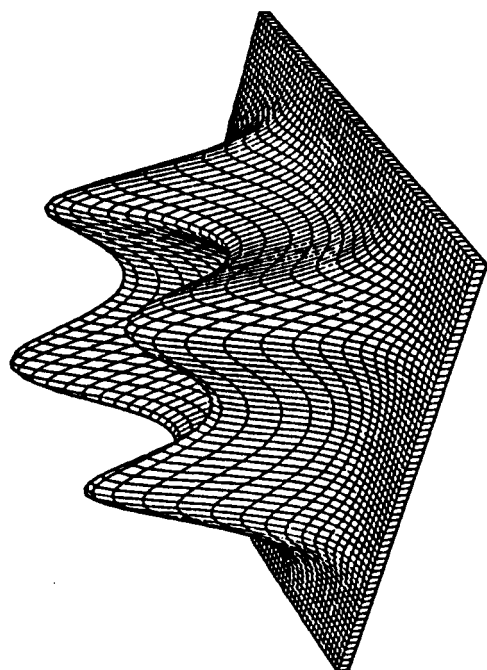
Cross-section at $\nu = 0$ Cross-section at $\omega = 0$ a) $\omega_c = .3$ FIGURE 6. OPTIMAL EDGE DETECTOR OTF ($c(x,y) = -\nabla^2 L(x,y)$, $\nu_r = 3$)



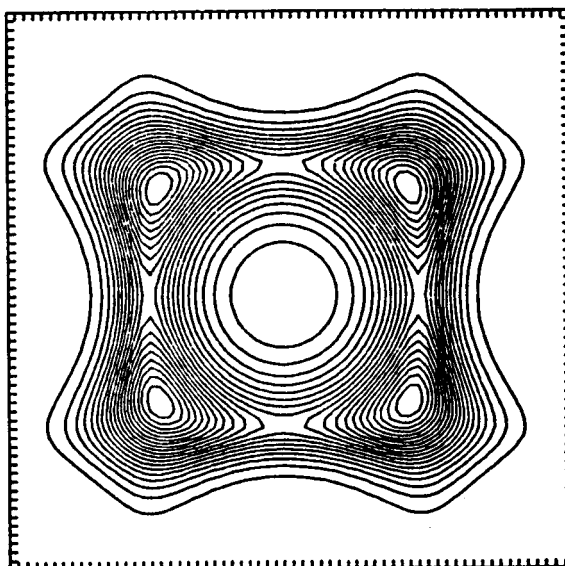
Cross-section at $\nu = 0$



Cross-section at $\omega = 0$



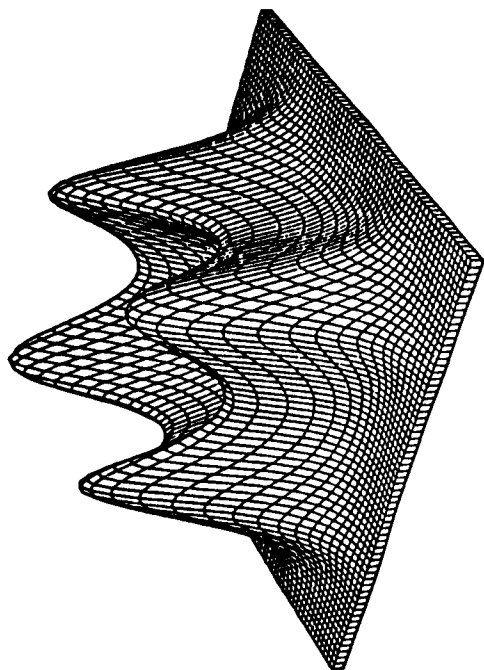
Perspective Plot



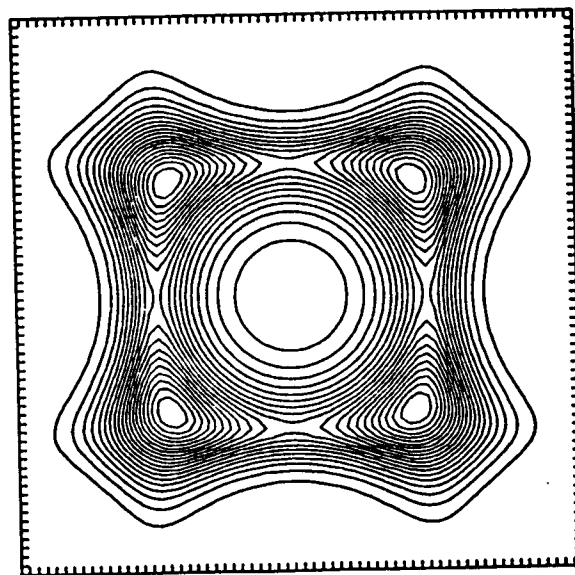
Contour Plot

b) $\omega_c = .5$

FIGURE 6. OPTIMAL EDGE DETECTOR OTF ($c(x,y) = -\nabla^2 L(x,y)$, $\mu_r = 3$)



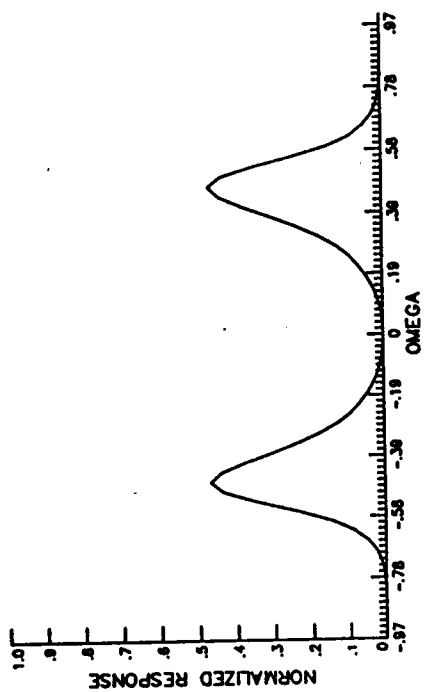
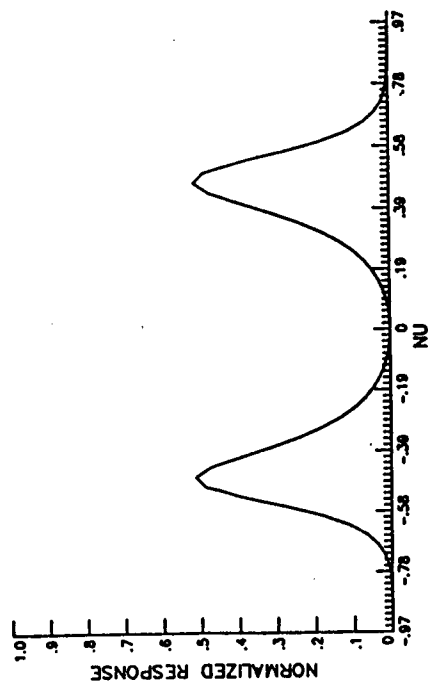
Perspective Plot

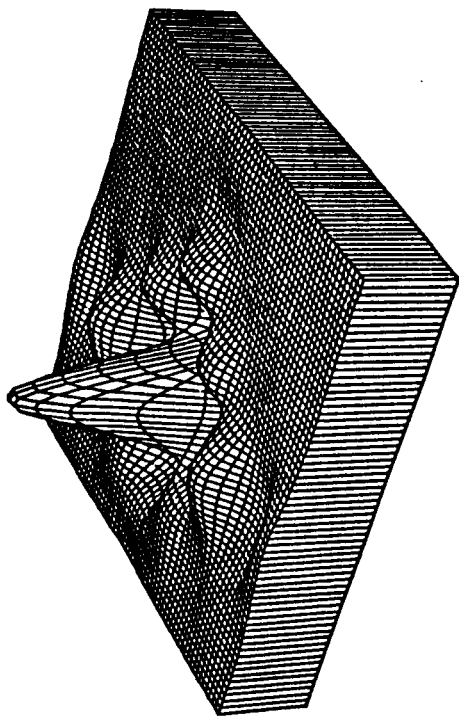


Contour Plot

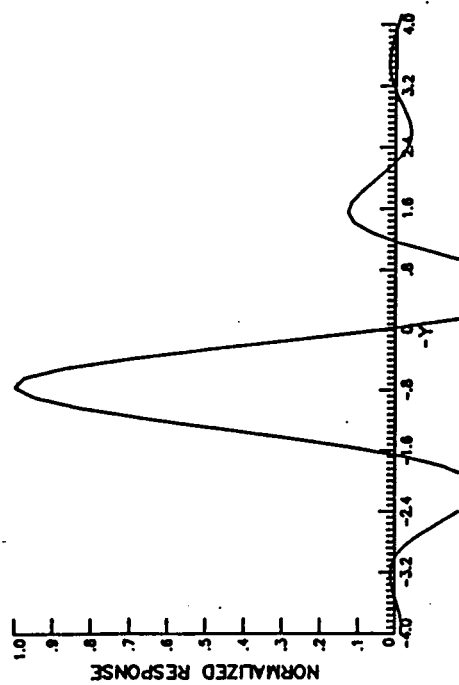
$$c) \omega_c = .7$$

FIGURE 6. OPTIMAL EDGE DETECTOR OTF ($c(x,y) = -\nabla^2 L(x,y)$, $\mu_r = 3$)

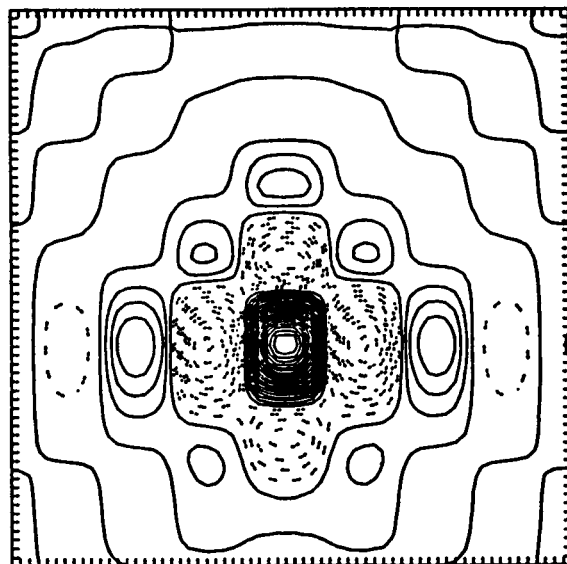
Cross-section at $\nu = 0$ Cross-section at $\omega = 0$



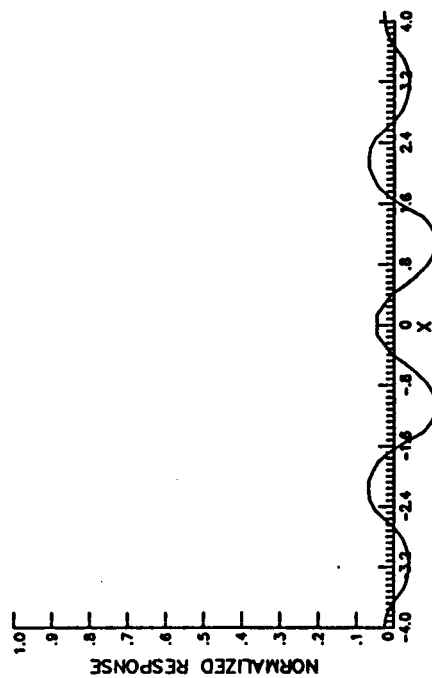
Perspective Plot



Cross-section at $x = 0$



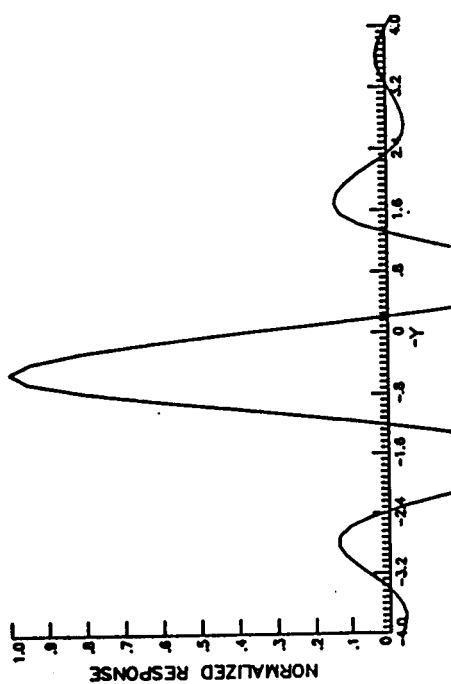
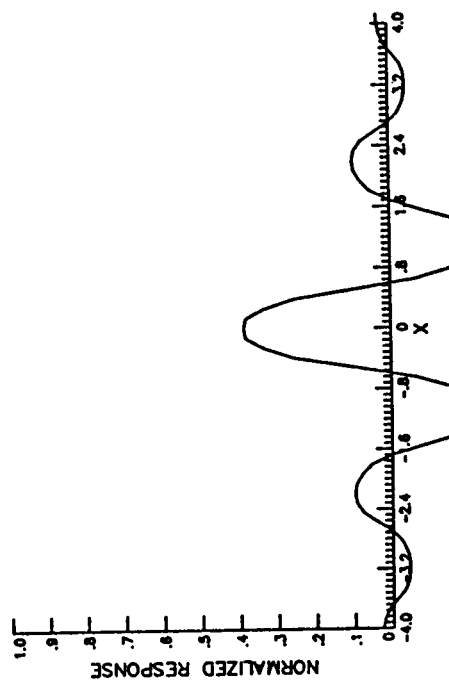
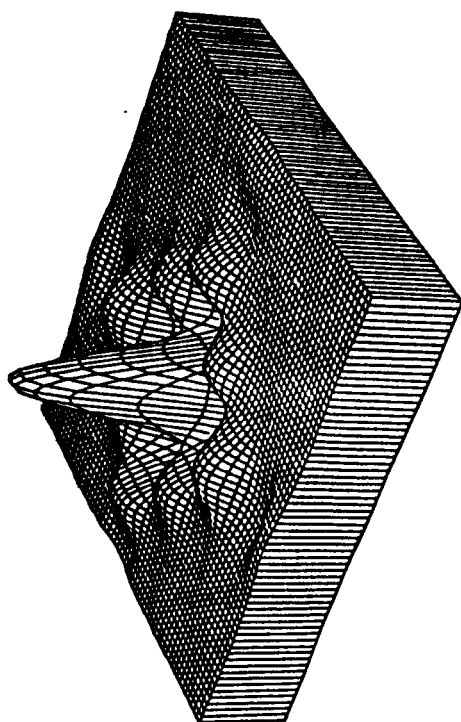
Contour Plot



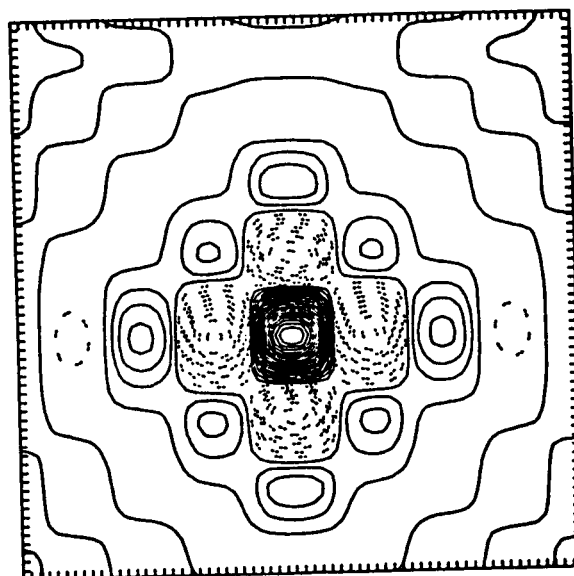
Cross-section at $y = 0$

a) $\omega_c = .3$

FIGURE 7. OPTIMAL EDGE DETECTOR PSF ($c(x,y) = -\nabla^2 L(x,y)$, $\mu_r = 3$)

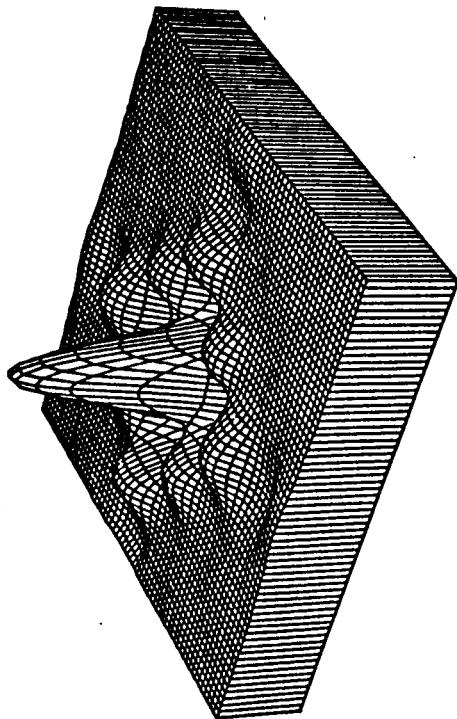
Cross-section at $x = 0$ Cross-section at $y = 0$ b) $\omega_c = .5$ 

Perspective Plot

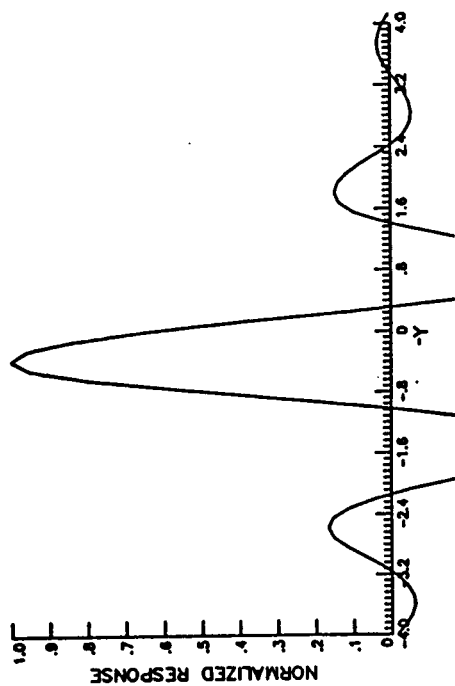


Contour Plot

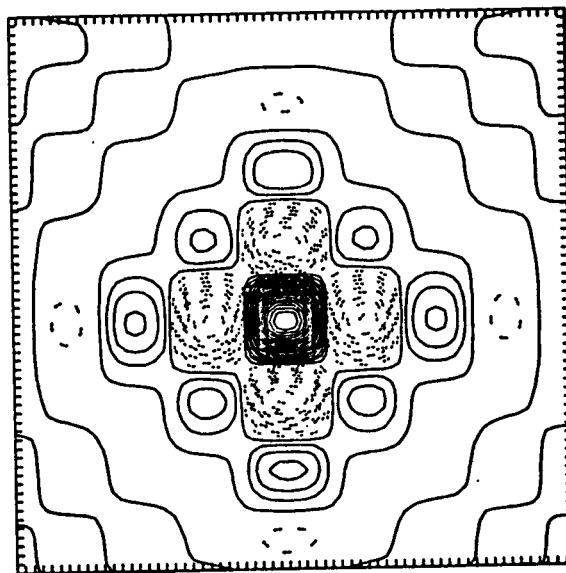
FIGURE 7. OPTIMAL EDGE DETECTOR PSF ($c(x,y) = -\nabla^2 L(x,y)$, $\mu_r = 3$)



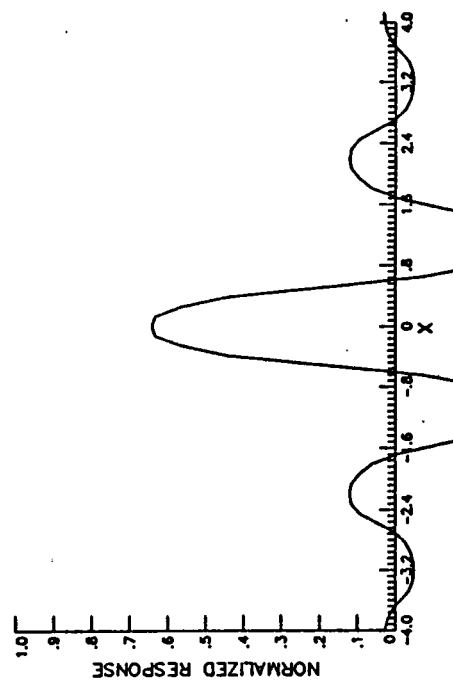
Perspective Plot



Cross-section at $x = 0$



Contour Plot



Cross-section at $y = 0$

c) $\omega_c = .7$

FIGURE 7. OPTIMAL EDGE DETECTOR PSF ($c(x,y) = -\nabla^2 L(x,y)$, $\mu_r = 3$)

1. Report No. NASA CR-178353		2. Government Accession No.		3. Recipient's Catalog No.	
4. Title and Subtitle Combined Optimization of Image-Gathering and Image-Processing Systems for Scene Feature Detection				5. Report Date August 1987	
				6. Performing Organization Code	
7. Author(s) Nesim Halyo, Robert F. Arduini, Richard W. Samms				8. Performing Organization Report No. FR 687101	
9. Performing Organization Name and Address Information & Control Systems, Incorporated 28 Research Drive Hampton, VA 23666				10. Work Unit No. 549-01-31-01	
				11. Contract or Grant No. NAS1-17133	
12. Sponsoring Agency Name and Address National Aeronautics and Space Administration Langley Research Center Hampton, VA 23665				13. Type of Report and Period Covered Contractor Report	
				14. Sponsoring Agency Code	
15. Supplementary Notes NASA Langley Technical Monitor: Friedrich O. Huck Final Report					
16. Abstract <p>In this study, the relationships between the image-gathering and image-processing systems for minimum mean-squared error estimation of scene characteristics are investigated. A stochastic optimization problem is formulated where the objective is to determine a spatial characteristic of the scene rather than a feature of the already blurred, sampled and noisy image data. An analytical solution for the optimal characteristic image processor is developed. The Wiener filter for the sampled image case is obtained as a special case, where the desired characteristic is scene restoration. Optimal edge detection is investigated using $\nabla^2 G$ as the desired characteristic, where G is a two-dimensional Gaussian distribution function. It is shown that the optimal edge detector compensates for the blurring introduced by the image gathering optics, and notably, that it is not circularly symmetric. The lack of circular symmetry is largely due to the geometric effects of the sampling lattice used in image acquisition. The optimal image gathering OTF is also investigated and the results of a sensitivity analysis are shown. The effects of phase distortion due to on-line electrical filtering in the image-gathering system are examined. An effective image-gathering point-spread function (PSF) including the effects of both electrical and optical systems is developed. It is shown that the phase distortion appears in the effective image-gathering PSF as a shift in the location of the PSF maximum, an asymmetry about the maximum and a decaying "tail" which effectively widens the sensor's footprint. The edges of the acquired image are not only blurred, but also shifted in position along the scan direction. This effect further stresses the importance of the combined image gathering and processing approach. It is shown that the optimal image processor compensates for both phase and magnitude distortion in the image to the extent compatible with noise attenuation, and continues to display a lack of circular symmetry while being highly influenced by the sampling lattice used in image acquisition. Finally, it is shown that the spatially averaged mean-squared error and its sensitivity to variations in the scene detail and noise statistics are both independent of the image-gathering system phase characteristics, when the optimal image processor is used to correct magnitude and phase distortion.</p>					
17. Key Words (Suggested by Author(s)) image-processing system, optimization, image-gathering system, edge detection, feature detection, optimal edge detection, phase distortion, effective PSF			18. Distribution Statement Unclassified - Unlimited Subject Category 35		
19. Security Classif. (of this report) Unclassified	20. Security Classif. (of this page) Unclassified	21. No. of Pages 89	22. Price* A05		